

**REDUCED ORDER MODELLING OF MISTUNED INTEGRALLY
BLADED ROTORS**

by

Jhansi Reddy Dodda

A Thesis

Submitted to the Faculty of Purdue University

In Partial Fulfillment of the Requirements for the degree of

Master of Science in Mechanical Engineering



School of Mechanical Engineering

West Lafayette, Indiana

August 2023

**THE PURDUE UNIVERSITY GRADUATE SCHOOL
STATEMENT OF COMMITTEE APPROVAL**

Dr. Nicole Key, Chair

School of Mechanical Engineering

Dr. Yujun Leng

School of Mechanical Engineering

Dr. Andres Arrieta

School of Mechanical Engineering

Approved by:

Dr. Nicole Key

Dedicated to my family and friends.

ACKNOWLEDGMENTS

I want to extend my deepest gratitude to my advisor, Professor Nicole Key, for giving me this opportunity to learn from extraordinary people at Purdue University. I am incredibly grateful for her motivation and mentorship, which helped me improve and grow as a researcher. I also want to thank Dr. Yujun Leng and Dr. Andres Arrieta for serving on my committee and for their valuable feedback on my work.

I would like to thank Guide 6 Consortium, Purdue University, and Rolls-Royce for their financial support. I am also very thankful to Laith Zori for his valuable advice. Additionally, this endeavor would not have been possible without the P3S team, Doug, Joey, Yujun, and Amanda, the best teammates and friends I could have asked for. I would like to extend my sincere thanks to Doug Matthews and Yujun Leng, without whom this thesis would not be possible. I would like to thank Yu Ning, Will, Adam, and Dean for their wonderful friendship and support. I will always cherish these memories. I am grateful to everyone at the lab who make it a fun workplace.

I would like to thank my parents, who supported me despite my absences when they needed me. Words cannot express my gratitude to my dad, who stayed positive and encouraged me, especially when it should have been I who did so during his recovery. My accomplishments will never have been achievable without your unwavering support. Lastly, I want to thank Trishika and my friends who loved and supported me back home. I love you all very much. Thank you for everything.

TABLE OF CONTENTS

LIST OF TABLES	7
LIST OF FIGURES	8
NOMENCLATURE	12
ABSTRACT.....	14
1. INTRODUCTION	16
1.1 Motivation.....	16
1.2 GUIde Consortium.....	18
1.3 Structural dynamics	19
1.3.1 Modal Analysis.....	22
1.4 Forced Response	27
1.4.1 Frequency splitting	31
1.4.2 Mode Localization.....	32
1.4.3 Intentional mistuning and Damage assessment	34
1.5 Harmonic Analysis.....	35
1.6 Reduced order modeling.....	36
1.6.1 Lumped parameter model and beam frame assembly model	36
1.6.2 FE-based reduced order models.....	37
1.7 Mistuning.....	41
1.8 Research Objectives.....	46
2. COMPUTATIONAL METHODOLOGY.....	48
2.1 Purdue 3-stage Axial Compressor Facility	48
2.2 FEM models.....	50
2.3 Mistuning cases.....	55
3. SIMULATION AND RESULTS	58
3.1 Grid Convergence Study.....	58
3.2 Comparative Studies	64
3.2.1 CMM Method - Effect of Tuned system modes (TSM) and Cantilever blade modes (CBM)	65
3.2.2 Small Mistuning Cases	70

3.2.3 Frequency Mistuning	95
4. LARGE MISTUNING CASES	98
5. SUMMARY AND CONCLUSIONS	110
5.1 Overview	110
5.2 Recommendations for future work	111
APPENDIX: HARMONIC ANALYSIS METHODS	113
REFERENCES	115

LIST OF TABLES

Table 2.1 PAX100 compressor Configurations	49
Table 2.2 Excitation Orders on Rotor 2 in different configurations	50
Table 3.1 Mesh elements and number of equations for grid convergence study	58
Table 3.2 Spacing and Grid refinement factor of the FE models.	60

LIST OF FIGURES

Figure 1.1 Collars Triangle reproduced – reproduced from Collar [2].....	17
Figure 1.2 Cyclic symmetric structure.....	19
Figure 1.3 Single DoF system.....	20
Figure 1.4 Response Magnification factor varying with speed from Xuanen et al. [6].....	22
Figure 1.5 Disk mode shapes	23
Figure 1.6 Blade mode shapes	24
Figure 1.7 Mass-spring model of an airfoil section - reproduced from Leng [8]	24
Figure 1.8 (a) Forward traveling wave and (b) Backward traveling wave.	25
Figure 1.9 Flow-induced vibration -reproduced from Razvan [12].....	27
Figure 1.10 Primary forcing functions from Li [13].....	28
Figure 1.11 Nodal diameter vs. Frequency (Hz).....	29
Figure 1.12 Campbell Diagram.....	30
Figure 1.13 Zig-Zag Diagram	31
Figure 1.14 Frequency splitting from Ewins [14].....	32
Figure 1.15 Magnification Factor corresponding to EO1 of intentionally mistuned designs from Judge et al. [19].....	34
Figure 1.16 Harmonic analysis system from Ansys Structural Analysis Guide [23].	35
Figure 1.17 (a) Lumped mass parameter model (b) Beam frame assembly model from Yuan et al. [24].....	37
Figure 1.18 Substructuring of a mistuned bladed disk from Bladh et al. [29].....	42
Figure 2.1 Purdue 3-stage axial compressor flow path.....	49
Figure 2.2 Single Sector FEM model	51
Figure 2.3 GridPro mesh in the hub and fillet region.	52
Figure 2.4 Effects of inherent mistuning on forced response due to the mesh.	53
Figure 2.5 Full Blisk FEM model	54
Figure 2.6 Forcing and response probe location of the FE models	54
Figure 2.7 Mistuning pattern for a case study with small proportional mistuning	56
Figure 2.8 Mistuning pattern for a case study with proportional mistuning.....	56

Figure 3.1(a) Natural frequency of first four tuned system modes as a function of mesh size (b) Percent error between Medium and Fine meshes of the first 200 modes	59
Figure 3.2 GCI for the first 50 modes.....	61
Figure 3.3 Frequency error percent relative to the extrapolated frequency for different levels of grid refinement.....	61
Figure 3.4 MAC Matrices ((a) Coarse and Medium mesh, (b) Medium and fine mesh)	63
Figure 3.5 Relative Frequency Error for different grids.	64
Figure 3.6 Tuned system modes.	65
Figure 3.7 Effect of the number of tuned system modes retained (10 CBM).....	66
Figure 3.8 (a) Relative frequency error (b) Relative frequency error percent (ND 11) Note: Modal frequency is mapped to the left ordinate and the errors are mapped to the right ordinate.....	67
Figure 3.9 (a) Blade amplification factor for the first bending mode (b) Blade amplification factor for the first torsion mode (Retaining Bending Mode)(ND 11)	68
Figure 3.10 (a) Relative frequency error (b) Relative frequency error percent (ND 5).....	69
Figure 3.11 Effect of CBM on the forced response for the first torsion mode (ND 5).....	70
Figure 3.12 (a) Forced Response and (b) Amplification factor of Rotor 2 with 0.1% standard deviation mistuning (Full blisk - First Torsion Mode).	71
Figure 3.13 (a) Blade Amplification Factor and (b) Maximum response envelope (First Torsion Mode).....	73
Figure 3.14 Modal participation factors (First Torsion Mode).....	74
Figure 3.15 (a) Forced Response and (b) Amplification factor of 0.1% SD (Full blisk - First Bending Mode).	75
Figure 3.16(a) Blade Amplification Factor and (b) Maximum response envelope (First Bending Mode).....	75
Figure 3.17 Modal participation factors (First Bending Mode (ND 11))	76
Figure 3.18 Mistuned frequency (0.1% SD).....	77
Figure 3.19 (a) Forced Response and (b) Amplification factor of Rotor 2 with 0.5% standard deviation mistuning (Full blisk - First Bending Mode).	78
Figure 3.20 (a) Blade Amplification Factor and (b) Maximum response envelope (First Bending Mode).....	79
Figure 3.21 Modal participation factors (First Bending Mode (ND 11) – 0.5% standard deviation)	80
Figure 3.22 (a) Forced Response and (b) Amplification factor with 0.5% SD mistuning (Full blisk - First Torsion Mode).....	81

Figure 3.23 Modal participation factors (ND 11 – 0.5% standard deviation)	82
Figure 3.24 Tuned system mode selection approaches for Torsion Mode	83
Figure 3.25 Mistuned frequency (0.5% SD).....	84
Figure 3.26 (a) Blade Amplification Factor and (b) Maximum response envelope (ND 11 - First approach).....	85
Figure 3.27 (a) Blade Amplification Factor and (b) Maximum response envelope (ND 11 - Second approach).....	85
Figure 3.28 Blade Amplification Factor (First Approach)	86
Figure 3.29 Blade Amplification Factor (Second Approach).....	87
Figure 3.30 Comparison of Fullblisk amplification factor at ND 3, ND 5, and ND 11 crossings (0.5% Deviation).....	88
Figure 3.31 Amplification factors for ND 3, ND 5, and ND 11 crossings of 1 st Bending mode (0.5% Deviation)	89
Figure 3.32 (a) Forced Response and (b) Amplification factor 0.5% SD mistuning (Full blisk – ND 3).	91
Figure 3.33 (a) Blade Amplification Factor and (b) Maximum response envelope (ND 3).....	91
Figure 3.34 (a) Forced Response and (b) Amplification factor 0.5% SD mistuning (Full blisk – ND 5).	92
Figure 3.35 Modal participation factors (ND 5 – 0.5% standard deviation)	93
Figure 3.36 (a) Blade Amplification Factor and (b) Maximum response envelope (Sweep: 2500-2650 Hz: ND 5).....	94
Figure 3.37 (a) Blade Amplification Factor and (b) Maximum response envelope (Sweep: 2600-3000 Hz: ND 5).....	94
Figure 3.38 Amplification factors for ND 3, ND 5, and ND 11 crossings of 1st Bending mode (Ping test Frequencies (0.45% SD)).....	96
Figure 3.39 Amplification factors for ND 3, ND 5, and ND 11 crossings between 2000 to 3000 Hz (Ping test Frequencies (0.45% SD)).....	97
Figure 4.1 (a) Forced Response at ND 5 (Fullblisk - 300 Modes) (b) Forced Response at ND 5 (Fullblisk - 400 Modes)	99
Figure 4.2 (a) Maximum response envelope (ND 3) (b) Maximum response envelope (ND 5) (c) Maximum response envelope (ND 11) [Frequency Sweep 2000-3000 Hz].....	100
Figure 4.3 Amplification factors for ND 3, ND 5, and ND 11 crossings between 2000 to 3000 Hz (5% SD).	101
Figure 4.4 Amplification factors of first bending mode for ND 3, ND 5, and ND 11 (5% SD).	102

Figure 4.5 (a) Localized mode shape (Mode 31) (b) Tuned System Mode (Mode 31).....	103
Figure 4.6 (a) Localized mode shape (Mode 72) (b) Tuned System Mode (Mode 72).....	103
Figure 4.7 (a) Mistuned mode shape (Mode 39) (b) Tuned System Mode (Mode 39).....	104
Figure 4.8 Mistuned frequencies comparison for various SD.	105
Figure 4.9 Blade amplification factor (5% SD)	105
Figure 4.10 Maximum amplification factor of the mistuned system.....	106
Figure 4.11 Maximum blade amplification factor error for FMM and CMM models at ND 11	107
Figure 4.12 Maximum amplification factor error of the sweep for FMM and CMM models at ND 11.....	107
Figure 4.13 Normalized response band	108
Figure 4.14 Amplification factors for ND 3, ND 5, and ND 11 crossings between 2000 to 3000 Hz (Random Mistuning).....	109

NOMENCLATURE

<u>Symbol</u>	<u>Definition</u>
A	Amplification factors
[A], [B]	representative matrices in Block Lanczos method
APDL	Ansys Parametric Design Language
Bcirc	Block Circulant matrix
Bdiag	Block Diagonal matrix
CMM	Component Mode Mistuning
C, Ct, Cb	Damping matrix
DOF	Degrees of Freedom
EO	Engine order
EOM	Equation of motion
F	Excitation force matrix
FE	Finite Element
FMM	Fundamental Mode Mistuning
I	Inertia
IBR	Integrated bladed rotor
K	Stiffness Matrix
M	Mass matrix
N	Number of disk-blade sectors
ND	Nodal Diameter
ROM	Reduced order model
SD	Standard Deviation
[S]	Static condensation matrix
[G]	Shape functions matrix
[s]	Stress stiffening matrix
x	Displacement
Greek Symbols	
ω, Ω	Frequency

τ	Stresses
α	Angular Deflection
Φ	Normal Modes
Ψ	Attachement Modes
Λ, λ	Eigenvalues (Frequencies)

ABSTRACT

This work aims to study the mode localization behavior of the mistuned rotor, which is the root cause of the unexpected premature fatigue failure. The unsteady loading, flow separations, tip leakage flows, vortex shedding, and acoustic instabilities induce nonlinear blade vibrations and responses. An accurate finite element model can help predict the maximum dynamic response and shed light on the dynamics of the mistuned system, which can lay out guidelines for design and manufacturing processes. Cyclic symmetry structures are generally simplified as Finite Element (FE) models of single sectors for analysis purposes to reduce computational costs. However, inherent blade mistuning breaks the cyclic symmetry, and often the full blisk must be modeled, which has millions of degrees of freedom (DOF), making it computationally too expensive. These simulations are often coupled with Monte Carlo simulations (MCS) and Latin hypercube for the probabilistic analysis of random mistuning, which requires a large sample set, further increasing the computational costs.

Previous research and aeromechanical analysis used lumped mass and beam frame assembly models, which were very robust but had a low order of accuracy. This paved the way for developing FE-based Reduced Order Models (ROM). These high-fidelity complex models can capture the simplified nonlinearities in reduced-order models. The CMM (Component Mode Mistuning) and FMM (Fundamental Mode Mistuning) models were studied on the embedded stage of the Purdue 3-Stage axial compressor to understand the accuracy and usability of these methods for regions of interest.

A brief comparison between the ROM models is made in this study. Although the FMM model is a simple, accurate model for determining the impact of mistuning on forced response when we have an isolated family of blade modes, the accuracy decreases considerably in cases with strong modal participation from other families. The more complex CMM model is required to study mistuned responses in veering regions, regions with high modal density, and instances of disk-dominated modes. The FMM model estimates the amplification well for mistuning cases with low deviations and high nodal diameters. The CMM model captures the intricate details of the response well and converges rapidly with the increasing number of tuned system modes. The modal participation in the veering regions was also captured reasonably well by CMM. The forced response for cases with small standard deviation was predicted well by both the reduced order

models. The effect of the arrangement of the deviations was also explored, which showed significant amplification reduction.

This study will guide the future to predict forced response incorporating frequency mistuning and aerodynamic coupling, which would be validated with the experimental data.

1. INTRODUCTION

1.1 Motivation

An important design factor in turbomachinery is optimizing the rotor mass for higher aerodynamic performance. The Integrally Bladed Rotors (IBRs) extensively used in aviation applications have evident performance, cost, and mass reduction benefits. However, the significant challenges in their mechanical design are the impacts of mistuning, which are amplified by the structure's low dampening level, higher disk flexibility, and blade/disk interaction. High Cycle Fatigue (HCF) is responsible for up to 55% of Class A jet accidents that cost over \$1 million or result in the loss of the aircraft, as well as 30% of the expenditures related to jet engine maintenance. Most failures are caused by pre-existing flaws or end-of-life fatigue. According to Beuseroy and Lengellé [1], the failure modes are often caused by crack propagation driven mainly by vibrations. This makes it essential to understand the dynamic behavior of a blisk since the reliability of turbomachinery depends on the capacity to recognize and anticipate these risky resonance circumstances in the design phase.

In turbomachinery, the interactions of the inertial, aerodynamic, and elastic forces cause aeromechanical phenomena such as flutter and forced response, as shown in the Collars triangle in Figure 1.1. In an IBR, the inertial force is a function of mass, the stiffness of the blisk introduces the elastic force, and the external unsteady blade interactions such as wakes, potential fields, and blade motion constitute the aerodynamic forces.

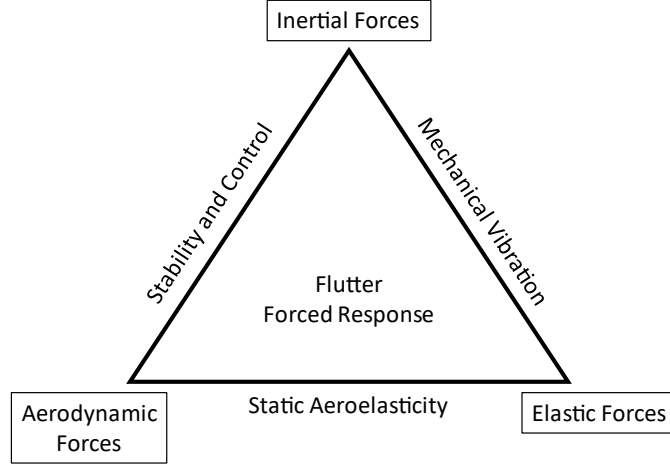


Figure 1.1 Collars Triangle reproduced – reproduced from Collar [2]

These forces are mathematically represented by a second order non-homogeneous differential equation known as the Equation of Motion (EOM) that satisfies Newton’s Second law.

$$[M_{struc}]\ddot{X} + [C_{struc}]\dot{X} + [K_{struc}]X = [F_{exc}] + [F_{coupled}(x(t),\dot{x}(t))] \quad (1.1)$$

$$[M_{struc}]\ddot{X} + ([C_{struc}] + [C_{aero}])\dot{X} + ([K_{struc}] + [K_{aero}])X = [F_{exc}] \quad (1.2)$$

M_{struc} , C_{struc} , and K_{struc} are the structure’s mass, damping coefficient, and stiffness, respectively. The aerodynamic coupled force can be represented in terms of aerodynamic damping (C_{aero}) and aerodynamic stiffness (K_{aero}) using Equation (1.2), rearranged from Equation (4.2). The externally applied forcing function (F_{exc}) is generally expressed as a periodic time function.

The unavoidable non-uniformities known as mistuning introduced into the system due to variations in geometric and material properties, manufacturing tolerances, and non-uniform wear can cause premature failure. Mistuning can significantly change the vibratory response of a tuned system. This makes it a primary factor of failures due to the normal mode localization phenomenon, in which vibration energy is restricted to a few blades leading to higher stresses. The mistuned system behaves like a simple “tuned absorber” in which a part of the system (absorber) may be under resonance while the other parts remain stationary. The mechanical or aerodynamic coupling between different blades can further complicate the vibratory behavior of the system. In the worst situation, a higher-frequency vibration with a modest amplitude could result in failure

owing to HCF. These factors have made modeling and understanding the influence of mistuning on turbomachinery forced response essential. Forced response and flutter, the major types of aeromechanics problems in axial compressors, are caused by external excitation and self-excited oscillation. Synchronous vibration, the major portion of this study, is the forced response of the blades subjected to periodic excitation due to the unsteady aerodynamic loading at the fundamental frequency and its integer multiples. Analysis of resonant frequencies and the forced response prediction of mistuned blades can be used to explore the dynamic behavior, fatigue life, and damage detection with response-based identification methods. Simplified FE models of single sectors are not appropriate for analysis because mistuning destroys the cyclic symmetry of bladed-disk systems; instead, a full-bladed disk model is typically required. Millions of degrees of freedom (DOFs) are often used in a full FE model of a bladed disk, making parametric analysis unaffordable even with high-performance computing.

$$x = \{[M_{struc}]\omega^2 + ([C_{struc}] + [C_{aero}])\omega + ([K_{struc}] + [K_{aero}])\}^{-1}[F_{exc}] \quad (1.3)$$

The vibration amplitude can be computed in the frequency domain by solving the inverse in Equation (1.13), rearranged from Equation (1.2). The inverse must be solved for all the degrees of freedom of the system, which makes ROMs a feasible choice to reduce the size of the matrices and thus reduce the computational cost. The GUIde consortium was established to research these reduced order models, understand the dynamic behavior and solve these issues of excessive vibration and high cycle fatigue.

1.2 GUIde Consortium

“GUIde” is an acronym for Government Agencies, Universities, and Industry working toward decreased time and cost inculcated in engine development in turbomachinery blade response. This consortium aims to expedite the research and enhance the technology transfer to industry.

Researchers at Purdue University study the forced response and blade row interactions in the Purdue 3-stage compressor, which models the scaled-up rear stages of a high-speed compressor by matching the Mach number and Reynolds number at a design speed of 5000 rpm. The scaled-

up geometry allows precise instrumentation throughout the compressor, and the various stator configurations enable extensive research with different engine order excitation. PAX100 configuration studied in this facility is an open geometry, making it an excellent machine for analyzing multi-stage compressor mistuned forced response and validating the predictive tools as a part of GUIde Consortium.

1.3 Structural dynamics

Cyclic Symmetry

A structure consisting of a series of substructures identical in form and connectivity is considered periodic or tuned. The rotationally periodic structural properties and geometry leads to circulant matrices, as shown in Figure 1.2. In a circulant matrix, each row is a circular shift of the previous row such that the last element of the previous row becomes the first element. The mathematical representation of a circulant matrix for a structure with N sectors equivalent to the number of blades is shown in Equation (1.4).

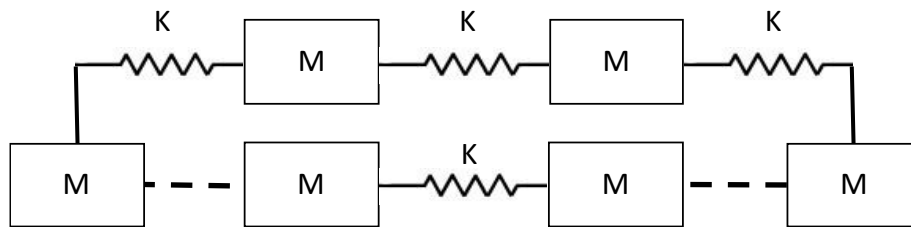


Figure 1.2 Cyclic symmetric structure

$$C = circ[c_1, c_2, \dots, c_N] = \begin{bmatrix} c_1 & c_2 & c_3 & \dots & c_{N-2} & c_{N-1} & c_N \\ c_N & c_1 & c_2 & \dots & c_{N-3} & c_{N-2} & c_{N-1} \\ c_{N-1} & c_N & c_1 & \dots & c_{N-4} & c_{N-3} & c_{N-2} \\ \vdots & \vdots & \vdots & \ddots & \vdots & \vdots & \vdots \\ c_3 & c_4 & c_5 & \dots & c_N & c_1 & c_2 \\ c_2 & c_3 & c_4 & \dots & c_{N-1} & c_N & c_1 \end{bmatrix} \quad (1.4)$$

If the matrix is symmetric and circulant, the matrix reduces further depending on N, as shown in Equation (1.5).

$$C = \begin{cases} \text{circ} \left[c_1, c_2 \dots \frac{c_{N+2}}{2}, \dots c_3, c_2 \right] & \text{if } N \text{ is even} \\ \text{circ} \left[c_1, c_2 \dots \frac{c_{N+1}}{2}, \dots c_3, c_2 \right] & \text{if } N \text{ is odd} \end{cases} \quad (1.5)$$

This property of cyclic structures can be utilized to reduce the computational cost by considering one sector instead of the full model.

Single Degree of Freedom (SDOF) system

The behavior of a physical system described by the EOM in Equation (1.6) is solved in the frequency domain for a single DOF model, as shown in Figure 1.3, to express motion as a function of time. Vibrational characteristics of a structure are generally computed by assuming the displacement (X) to be harmonic without the damping and excitation term using Equation (1.9), which solves the undamped system in a vacuum. This assumption transforms the problem into a straightforward eigenvalue problem to compute the vibrational characteristics of a structure.

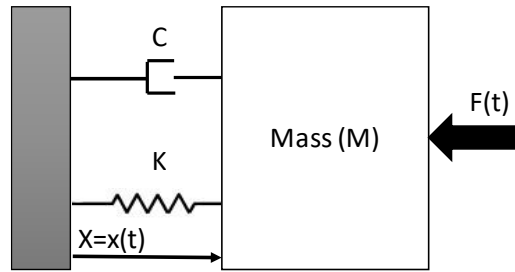


Figure 1.3 Single DoF system

$$M\ddot{X} + C\dot{X} + KX = F(t) \quad (1.6)$$

$$X = xe^{j\omega t} \quad (1.7)$$

$$(-\omega^2 M + j\omega C + K)x = F(t) \quad (1.8)$$

$$(-\omega^2 M + K)x = 0 \quad (1.9)$$

M is the structure's mass, C is the damping coefficient, K is the structure's stiffness, x is the displacement, ω is the frequency, and $F(t)$ is the excitation force. An undamped system's EOM does not contain the imaginary part associated with system loss and yields only real frequencies

and mode shapes. Structures with damping result in a complex eigen solution that can be interpreted into mode shape magnitudes and phase angles using physical quantities [3]. To model a multi-DOF system of equations for a complex structure like a blisk, the equations of the network of masses coupled by stiffness and damping coefficients are assembled and solved using a matrix formulation.

The changing geometry often introduces geometric nonlinearities in the system as it deflects under static or dynamic loads. The analysis of complex structures with geometric nonlinearities like IBR's solving linear systems is insufficient to compute the vibrational characteristics as they change the stiffness matrix significantly. These systems must consider nonlinearities induced due to large deflection, pressure load, stress stiffening, and spin softening. The centrifugal effects induced in the rotating machinery can change the direction of the centrifugal load and weaken the structure. A preceding static structural analysis is used to include the pre-stress effects in the modal analysis.

Stress stiffening and spin softening effects

A structure experiences stiffening or weakening in a stressed state which is an essential parameter for thin structures or where bending is high compared to in-plane displacements. This pre-stress is computed in a preceding static structural analysis which uses an additional stiffness matrix to account for this stiffening effect using equations (1.10) and (1.11)(4.2). The stress stiffness matrix is computed in at least two interactions depending on the effect of additional stiffness on the stresses using shape functions $[G]$ and true stresses $[\tau]$ integrated into the volume domain. The final stiffness matrix, including the stress stiffening effects, may have negative terms in cases with high compressive stresses. Insufficient rigid body constraints also lead to such matrices.

$$[s] = \int [G]^T [\tau] [G] d(vol) \quad (1.10)$$

$$[K] = [K_{static}] + [s] \quad (1.11)$$

Hui-Ying et al. [4] studied these effects for a rotating blade geometry and concluded that the increased radial centrifugal force and spin softening increased the blade vibration frequency on the order of 33 % for a 1200 rad/s rotational speed difference while the mode shape was not

significantly affected. The spin stiffening effect was prominent at high speeds, which reduced the frequencies. Houxin et al. [5] found a receptive interval of the vibration referred to as a “sensitive rotation speed region” where the stiffening effects were significant and can substantially change the frequencies and modal damping ratios for the shrouded interface. By default, a stress-free system is assumed in Ansys Mechanical, which can be overwritten by turning on the pre-stress effects. This study has considered these stiffening effects. Some of the previous research has included the Coriolis effect, which can deflect the moving mass in a rotating system. These forces can change the frequencies and behavior depending on the structure and rotational speed. Xuanen et al. [6] studied the effect of Coriolis force on the mistuned system. They observed that it increased the force response’s magnification factor by around 0.65% at a rotational speed of 3000 rpm. In comparison, it decreased the factor by 6.28 % for the mistuned system at 12000 rpm. The Coriolis forces effects are generally insignificant in the low-speed range of 3000 to 6000 rpm, as shown in Figure 1.4, and therefore excluded from the current investigation.

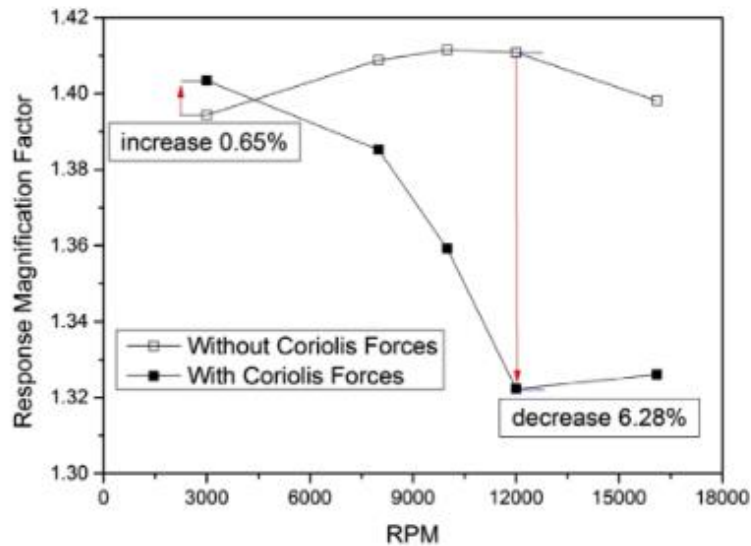


Figure 1.4 Response Magnification factor varying with speed from Xuanen et al. [6]

1.3.1 Modal Analysis

Modal analysis is used to determine a system’s vibration characteristics, like natural frequencies and mode shapes, which can then be combined with a pre-stressed structural analysis to conduct a transient dynamic analysis and harmonic response analysis. The eigenvalue problem

is solved for the system to study these characteristics. Cyclic symmetric structures have distinct vibrational modes, which can be classified into nodal diameter modes (ND), nodal circle modes (NC), and hybrid modes (ND-NC). Nodes are locations with zero displacements, and the diameters with zero displacements are known as nodal diameters. The circular mode shapes similar to Figure 1.5 (a) are classified as nodal circle modes. In contrast, the modes that are sinusoidal circumferentially with the nodes forming diametrical lines on the structure are categorized as the nodal diameter modes, as shown in Figure 1.5(b). Figure 1.5(c) shows the hybrid modes, a combination of nodal diameter and nodal circle modes.

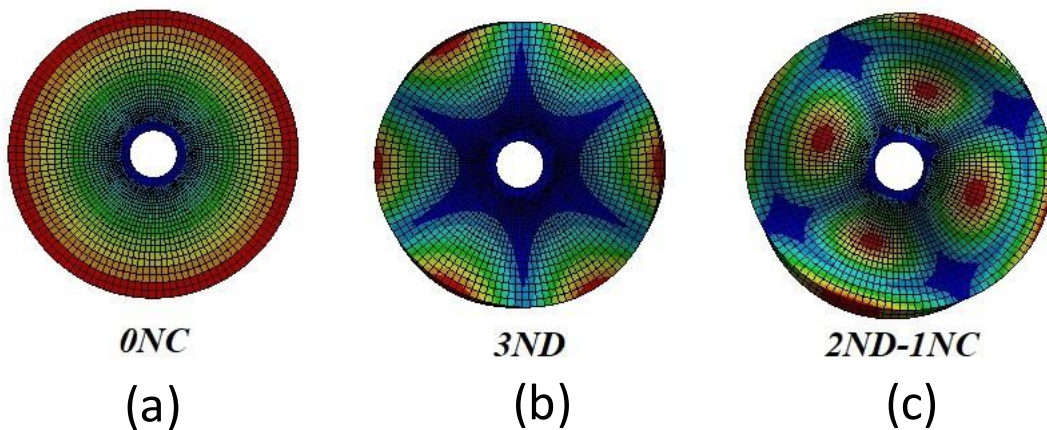


Figure 1.5 Disk mode shapes

In an IBR, blade or disk-dominated frequencies can be used to categorize the vibration, with blade modes further subdivided into families like first bending, first torsion, and so forth [7]. The disk modes are classified according to nodal diameters (ND) and nodal circles (NC). First Bending, First Torsion, and First Chordwise bending modes are illustrated in Figure 1.6 (a), (b), and (c), respectively.

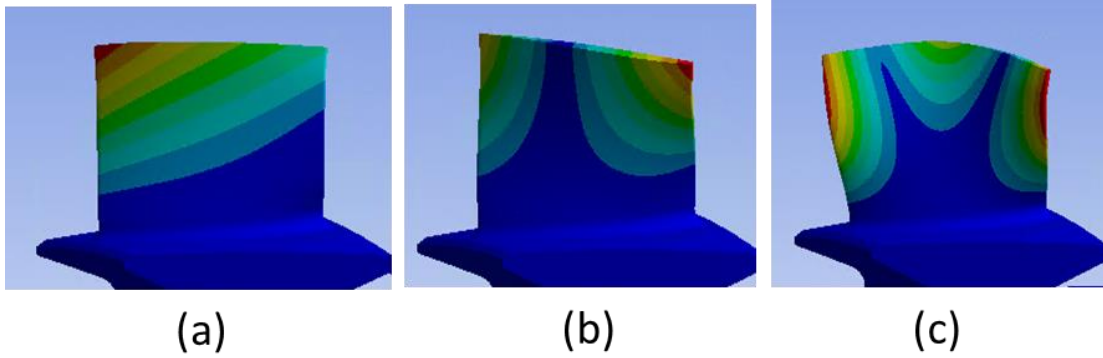


Figure 1.6 Blade mode shapes

In contrast to disk-dominated frequencies, which depend on the number of nodal diameters, blade-dominated frequencies are independent of this factor. The coupled system has various nodal diameters for each blade-dominated mode family. The torsion mode is usually excited due to the unsteady moment, unlike the bending mode, which is excited by force. Therefore the bending and torsion modes are often independent, as shown in Figure 1.7(a) and (b), respectively [8].

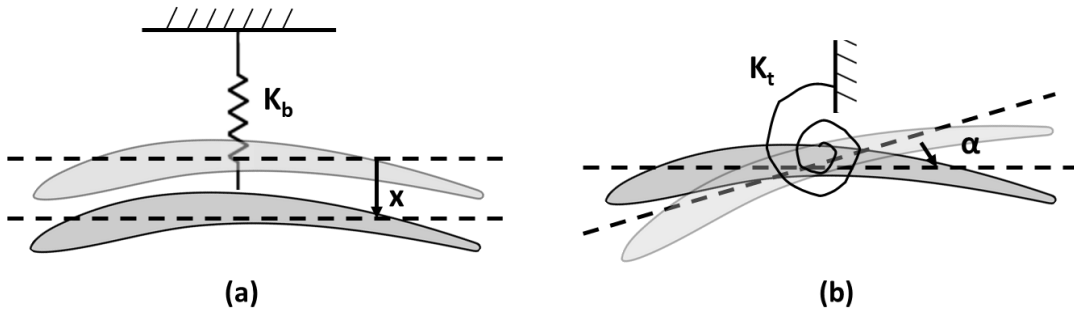


Figure 1.7 Mass-spring model of an airfoil section - reproduced from Leng [8]

The equations (1.12) and (1.13) are the EOM for the bending and torsion modes, respectively.

$$M\ddot{x} + C_b\dot{x} + K_b x = F(t) \quad (1.12)$$

$$I\ddot{\alpha} + C_t\dot{\alpha} + K_t \alpha = M(t) \quad (1.13)$$

The variable x is deflection, $F(t)$ is the unsteady lift, and C_b and K_b are the structural damping and stiffness for bending mode. Similarly, α is angular deflection, $M(t)$ is the unsteady moment, and C_t and K_t are the torsion mode's structural damping and stiffness. The harmonic blade vibration amplitudes with frequency ω for respective modes are calculated using equations (1.14) and (1.15).

$$\bar{x} = \frac{-F}{m\omega^2 - i\omega C_b - K_b} \quad (1.14)$$

$$\bar{\alpha} = \frac{-M}{I\omega^2 - i\omega C_t - K_t} \quad (1.15)$$

The cyclic symmetric structures have eigenvalues in pairs classified as degenerate solutions. The eigenvalues of nodal diameter 0 and nodal diameter $N/2$ for the systems with an even number of sectors have all the blades vibrating in the same phase and do not appear in pairs and are therefore referred to as non-degenerate solutions. The eigenvectors associated with the double eigenvalues are orthonormal to each other and appear as stationary orthogonal modes. A rotational excitation shown in Figure 1.8 can be constructed by a linear combination of these eigenvectors, known as a traveling wave, as the vectors are linearly independent [9]. The traveling wave could be a forward or backward traveling wave depending on the direction of propagation with respect to the rotor rotation.

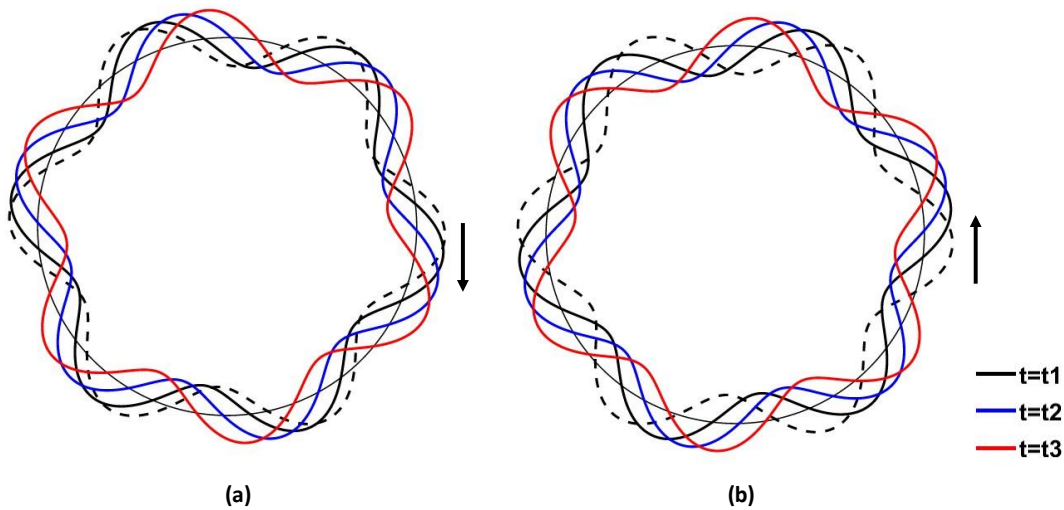


Figure 1.8 (a) Forward traveling wave and (b) Backward traveling wave.

The modal analysis method in Ansys Mechanical solves the EOM equations for each DOF to compute the eigenvalues and eigenvectors of the system. Ansys mechanical supports Block Lanczos, Supernode, Subspace, PCG Lanczos, unsymmetric, damped, and QR damped methods to solve for the system's eigenvalues. Block Lanczos is very robust in finding modes of large models, but this method cannot support FLUID elements in APDL. Ansys Parametric Design Language (APDL) is a structured scripting language that can interact with the Ansys Mechanical solver. When the interactions are too complicated or unsupported in the standard GUI, APDL is widely used to adjust simulation settings. APDL drives a finite element analysis program called Mechanical APDL (MAPDL). The PCG Lanczos, which is very similar to Block Lanczos, is only efficient in finding the first few modes.

Block Lanczos Algorithm

The Block Lanczos method implemented in Ansys Mechanical is an extension of the Lanczos algorithm. It iterates a block of vectors instead of only one vector to find eigenvalues of any given symmetric matrix. The concept of determining the sequence of estimates of the eigenvalues of a matrix from the block tridiagonal matrix was first proposed by Paige [10] and later developed by various researchers. This algorithm generates a banded tridiagonal matrix T_s by computing the orthonormal basis of the Krylov Space (Q_i). An example of the Block Lanczos algorithm using an initial arbitrary block Q_1 [11] on a symmetric matrix S is described in Equation(4.2).

$$A_i = Q_i^T(SQ_i) \quad (1.16)$$

$$P_i = SQ_i - Q_iA_i \quad (1.17)$$

$$Q_iB_{i+1} = P_i \quad \text{where, } i=1,2,\dots,N \quad (1.18)$$

$$T_s = Q^T S Q = \begin{bmatrix} A_1 & B_2^T & 0 & 0 & 0 \\ B_2 & A_2 & B_3^T & 0 & 0 \\ 0 & B_3 & A_3 & \ddots & 0 \\ 0 & 0 & \ddots & \ddots & B_N^T \\ 0 & 0 & 0 & B_N & A_N \end{bmatrix} \quad (1.19)$$

The generated sequence of blocks of Q_i for each iteration is used with the P matrix to check for convergence. The eigenvalues of block tridiagonal matrix T_s are computed and then used to

compute the corresponding eigenvectors. The eigenvectors are mutually orthonormal, simplifying the characteristic Equation to Equation (1.20) where λ_i are the eigenvalues. Ansys does not consider plasticity and only supports linear modal analysis. Any element specified as a nonlinear element is implemented as a linear element. Linear, isotropic, orthotropic, and temperature-dependent material properties can be applied to the model.

$$\det(T_s - \lambda_i I) = 0 \tag{1.20}$$

1.4 Forced Response

Vibration characteristics in a blisk

In turbomachinery, flow-induced vibration is classified into synchronous or non-synchronous vibration. Figure 1.9 shows the classification of Flow-Induced Vibration in Turbomachinery.

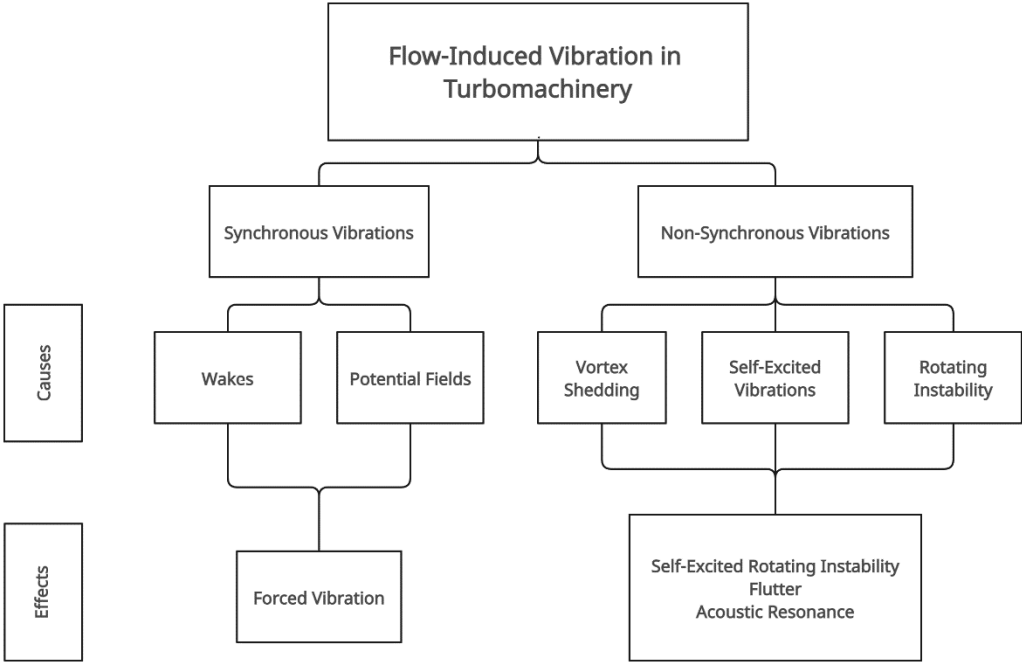


Figure 1.9 Flow-induced vibration -reproduced from Razvan [12]

The flow field distortions caused by upstream and downstream vane rows, struts, and inlet distortion give rise to forcing functions, making them a strong function of non-uniform potential

fields. The number of wakes produced by an upstream blade row, the potential field generated by blade rows downstream, and the total number of blade rows in adjacent compressor stages are utilized to determine the engine order [12]. This study focuses on the synchronous vibrations corresponding to specific engine orders (EOs), which are the machine's integral multiples of rotational frequency, mathematically represented using Equation (1.21)

$$f = EO * \frac{\Omega}{60} \tag{1.21}$$

Li [13] focused their research on the forced response of an embedded rotor blade row. They studied the primary forcing functions to predict the forced response of Rotor 2 in the Purdue 3-Stage axial compressor focusing on nodal diameter 11, which corresponds to the forcing function on 33 rotor blades by the adjacent stators with 44 vanes, Figure 1.10.

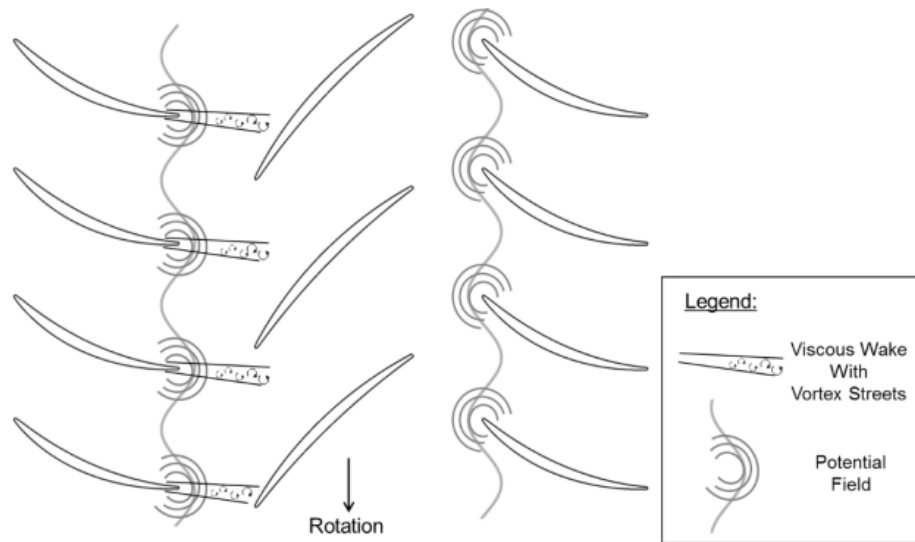


Figure 1.10 Primary forcing functions from Li [13]

She found that for a mistuned system, the amplification factor is a strong function of loading and observed a reduction in average response for chordwise bending mode in structures with weak structural coupling. Her research included the aerodynamic coupling effects, which did not heavily excite the modes. Therefore, the Fundamental Mode Mistuning model was recommended as a tool for studying mistuning for the modes excited by engine orders in this setup.

The loading-dependent aerodynamic coupling effects are neglected in this study to evaluate the reduced order models with different excitations excluding these dynamic changes.

Figure 1.11 shows frequencies with the corresponding ND. The frequencies fluctuate for the lower nodal diameters due to disk participation in the mode shape. Due to low disk participation, the blade modes with similar frequencies at various NDs appear horizontal. The “veering zones” marked in red are the areas where the system’s frequencies at the same nodal diameter are relatively closely spaced. Operating in these areas can be risky because it could result in energy exchanges between the modes. The regions where the frequencies cross are known as “crossing regions.”

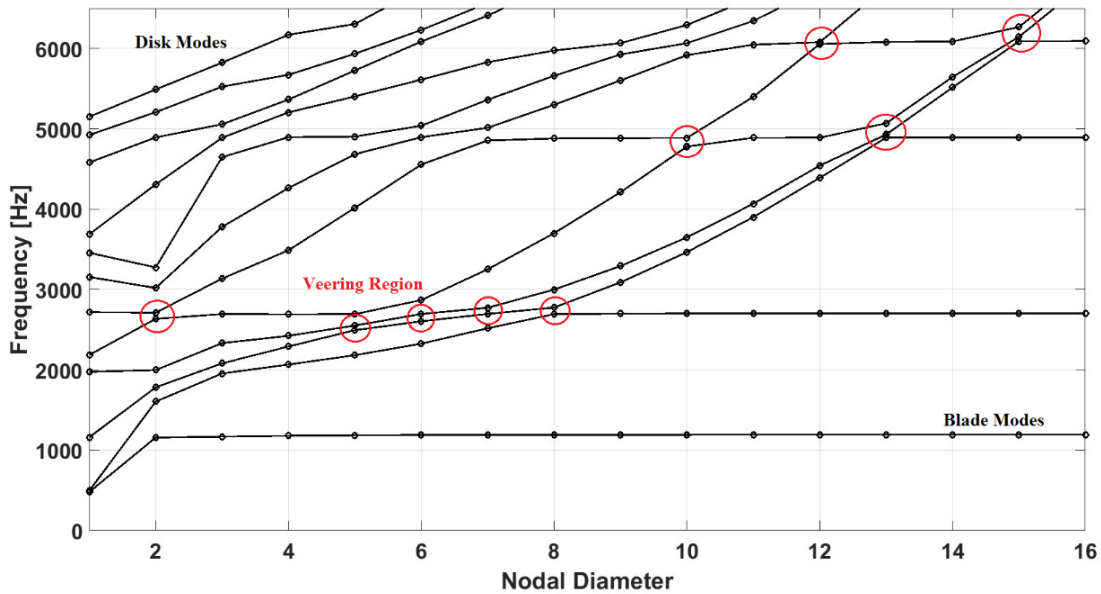


Figure 1.11 Nodal diameter vs. Frequency (Hz)

Factors like the low damping level, disk flexibility, and coupling between the blades and the disk amplify mistuning effects. Florence [9] found that multi-stage structures may have a more prominent amplification factor than single-stage ones. As a result, the ability to characterize and understand the influence of the structure’s dynamic behavior due to mistuning is essential to predict fatigue life. An accurate reduced-order model can reduce the computation cost to study such multi-stage effects.

Dynamic analysis tools

The Campbell and the ZigZag diagrams are standard tools designers use for dynamic structural analysis. The Campbell diagram, Figure 1.12, shows potential resonances where the engine order excitation coincides with the natural frequency of a mode. The resonant crossings are the intersection points of engine order lines and modal frequency. The natural frequency for most vibrational modes will increase as a function of speed due to centrifugal stiffening.

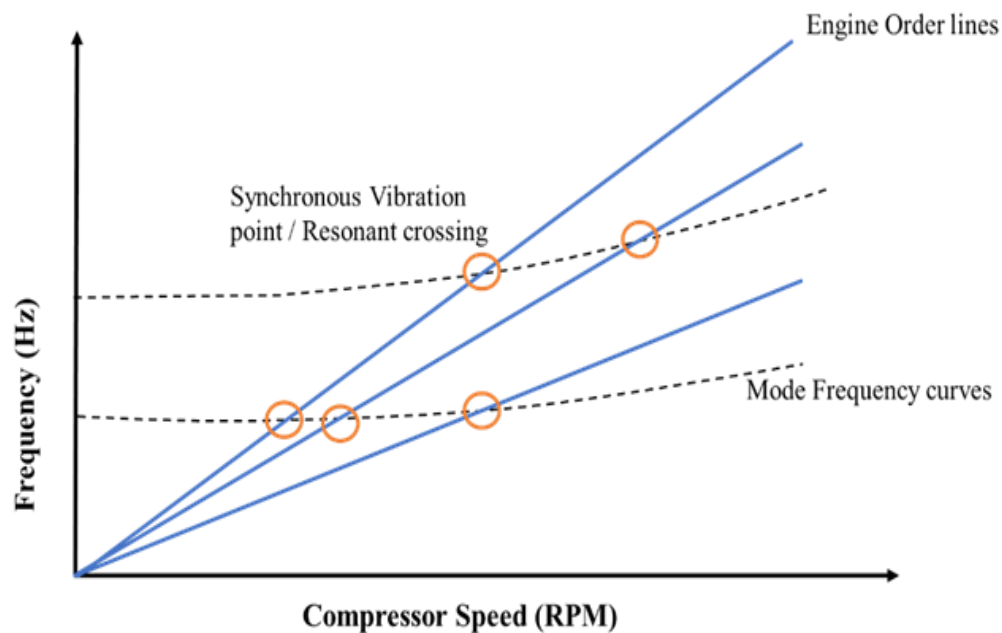


Figure 1.12 Campbell Diagram

However, previous research on turbines showed that the forced response was significant only for a few resonant points amongst a vast set of possible resonance points. The Zig-Zag diagram or Interference diagram shows the nodal diameters that can be excited by the excitation order. The forward traveling forcing wave, represented with a positive slope, travels in the same direction with respect to rotor rotation. In contrast, the backward traveling wave, represented with a negative slope in Figure 1.13, travels in the opposite direction. Each line represents a different EO in the diagram.

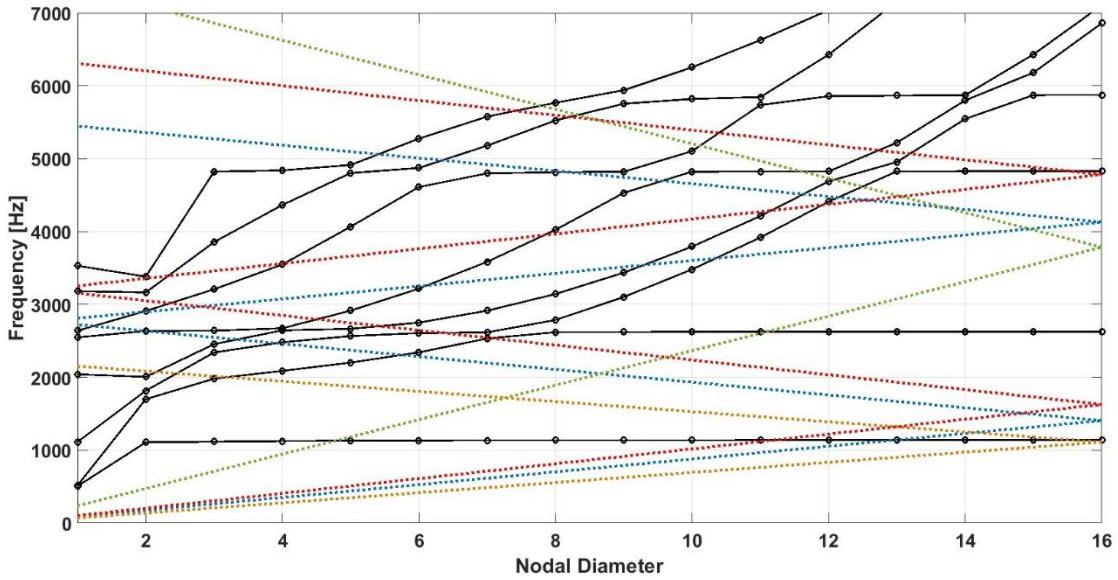


Figure 1.13 Zig-Zag Diagram

According to the Nyquist-Shannon sampling theorem, the maximum number of nodal diameters equals half the number of sectors in the structure. The harmonic indices, or nodal diameters, are between 0 and $N/2$ for an even number of sectors and $(N-1)/2$ for an odd number of sectors.

At resonance, the frequency of the excitation force is equal to the natural frequency, and the harmonic index of the mode corresponds to the harmonic of excitation. The periodic excitation must be of the exact wavenumber to excite a periodic mode structure. For a tuned system, resonant frequencies and responses are identical for all the blades, with a single peak in the frequency response at this frequency. However, mistuning can significantly change the resonant frequencies and forced response of each blade of the blisk.

1.4.1 Frequency splitting

The separation of the natural frequencies is one prominent consequence of mistuning, where the separation is directly proportional to the extent of mistuning. Ewins [14] found that the modes can be observed separately if the frequency separation is more than a factor of critical system damping. This trend causes multiple peaks in the frequency response, as shown in Figure 1.14, where the frequency splits by about 1% for blades mistuned to a 1% variation.

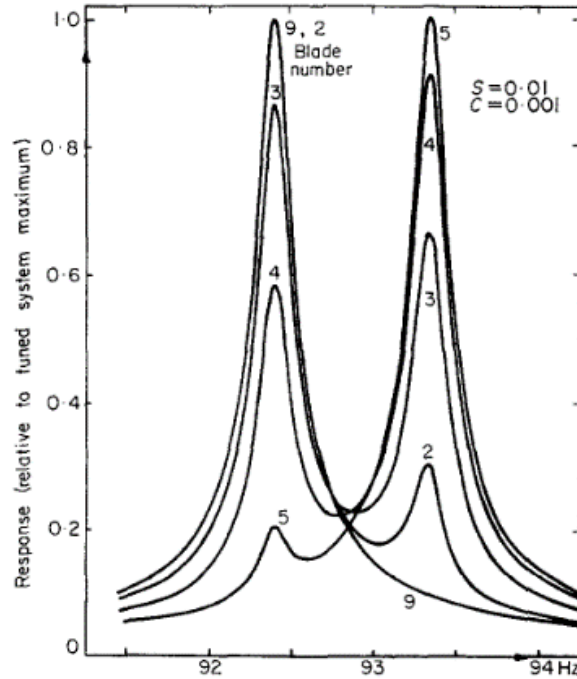


Figure 1.14 Frequency splitting from Ewins [14]

His research showed that this mistuning could raise blade stress by up to 20% for the deviations incurred due to manufacturing tolerances and wear over the engine's lifetime. Therefore it can be considered that all production engines experience this increase in blade stress. His studies also showed that when the same set of blades with similar deviations is rearranged, it can subdue the increase in stresses, which has encouraged research in the field of intentional mistuning to prevent premature failure.

1.4.2 Mode Localization

The propagating waves from the source reflect at the discontinuous boundaries of mistuned substructures and lead to the confinement of energy in that substructure, also referred to as localization. Mode localization causes the magnitude of vibration in a particular area of the structure to be higher than the overall magnitude of vibration. These vibrations are adverse in blisk configurations, which have much lower internal structural damping than blade-disk assemblies.

The periodic substructures use coupling coordinates to interact and have an equal number of pairs of characteristic waves as the number of coupling coordinates that exhibit frequency-dependent behavior [15]. Previous studies in this area concluded that mode localization increases when interblade coupling reduces. These behaviors can be classified into three types: frequency passbands, frequency stopbands, and frequency complex bands. The frequency passbands are undamped standing waves in contrast to stopbands and complex bands, which are attenuated standing waves and attenuated propagating waves, respectively. The strength of the substructure coupling affects the bandwidth of the passbands, which comprise natural frequencies equal to the number of substructures. The uncoupled substructure has a single frequency making the modal density a function of substructure coupling and the number of substructures. In cyclic symmetric structures, mode shapes are identical and sinusoidal in the circumferential direction in all substructures with the same interblade phase difference, and therefore, FEM is computationally inexpensive in tuned systems.

Pierre [16] investigated the effects of blade mistuning and concluded that the aeroelastic modes of a turbine grouped in N-mode groups, with each corresponding to a different blade mode, are highly sensitive to small random mistuning because of the weak aerodynamic coupling. While structural damping was not considered in his research, he discovered that a small deviation of 0.1% can result in excessive localization, which confines energy to a small number of turbine blades. Deterministic mistuning patterns have been optimized over the years to help predict the dynamic response, including the mistuning caused due to wear, thereby estimating the fatigue life and stresses.

Kaneko [17] used a spring-mass model to perform frequency response analysis incorporating Monte Carlo simulations to find the worst mistuning pattern and found that the acceleration rate changes the mistuning effect. The mistuning impact was diminished for larger acceleration speeds across the resonance zone. The larger the amplitude of the blade, the more significant the response reduction caused by an increase in acceleration rate. The reduction in vibration response was inversely related to the degree of damping. The most significant reduction in response occurred for ND-type vibrations or blisk response. Kaneko also concluded that the asymmetric vane spacing effectively reduces the resonant response for a mistuned-bladed disk. Past research showed that the frequency corresponding to the maximum amplitude increases as the acceleration increases and that mistuning could have the beneficial effect of suppressing the flutter

by decreasing the work done on the fluid. Kaza et al. [18] studied similar effects by developing a mistuned bladed disk. They found that mistuning has a fair chance of reducing the flutter response or speeding up the circumferential propagation of the flutter, and thus it was difficult to conclude that mistuning had only beneficial or detrimental effects on a particular system.

1.4.3 Intentional mistuning and Damage assessment

The beneficial effects of mistuning led to exploring the concept of intentional mistuning. Judge et al. [19] used a lumped parameter model to evaluate intentional mistuning and discovered that it could significantly lower the maximum response of a bladed disk due to random mistuning. They used the Monte Carlo method to randomly mistune the originally intentionally mistuned system designs (h1, h2, h3, and h4 in Figure 1.15). The system's sensitivity to random mistuning was reduced, with the magnification being relatively constant.

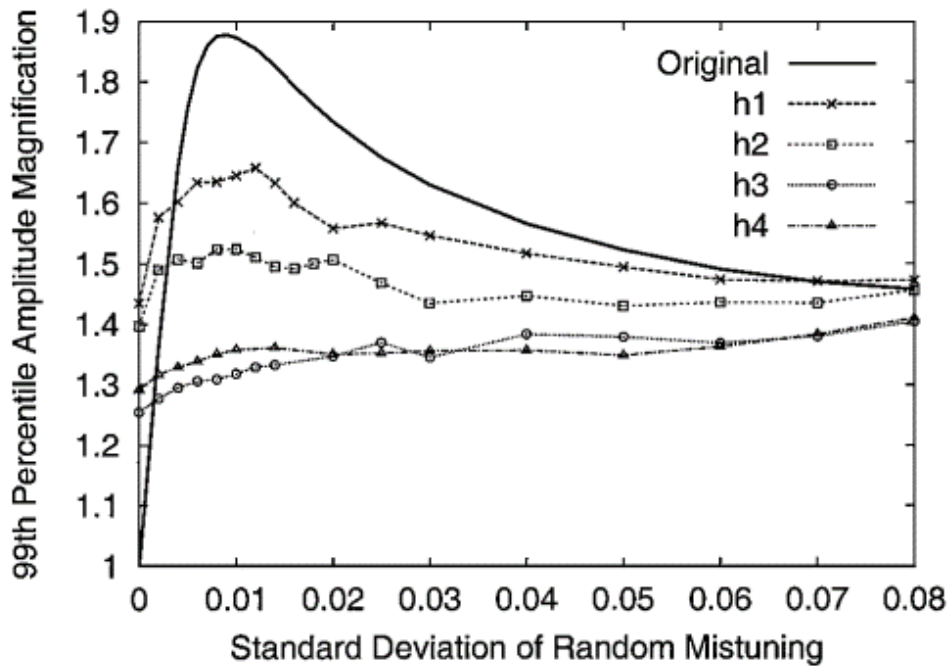


Figure 1.15 Magnification Factor corresponding to EO1 of intentionally mistuned designs from Judge et al. [19].

Mignolet et al. [20] studied the effects of the coupling strength of the blades and damping on the maximum forced response of the harmonic intentionally mistuned pattern. They concluded

that the responses localized by damping are highly sensitive to wavelength fluctuations. Understanding such dynamic behaviors of a mistuned system could help determine the system’s life. An efficient crack detection method would assist the system’s engine health monitoring and damage assessment. Laihao et al. [21] proposed a dynamic model to study nonlinear vibrations and developed a system that can characterize the cracks on the rotor blades and serve as a monitoring device.

Rehman et al. [22] used the Modal assurance criterion (MAC) technique to study different cracks and their damage index on a turbo fan blade to study the damage detection when the turbomachine is in operation. The modulus of elasticity of the elements in the FEM model was changed at the location of the crack to study the frequency variations. A high damage index was observed for the crack near the blade tip and at three-quarters of the length of the blade.

1.5 Harmonic Analysis

Harmonic analysis is used to compute the response in a structural member produced by a cyclic load. Harmonic analysis in Ansys Mechanical computes the steady state response of a linear system and can only take time-varying sinusoidal loads with the same frequency as described in Figure 1.16. It does not consider any nonlinear or transient effect while solving the EOM. The transient dynamic analysis allows the harmonic loads to be expressed as time history functions which can be used to capture the transient effects. Ansys supports various types of damping, which must be specified to prevent infinite responses at the resonant frequencies. Structural damping integrates the hysteretic behavior of the structure as a coefficient of the stiffness matrix.

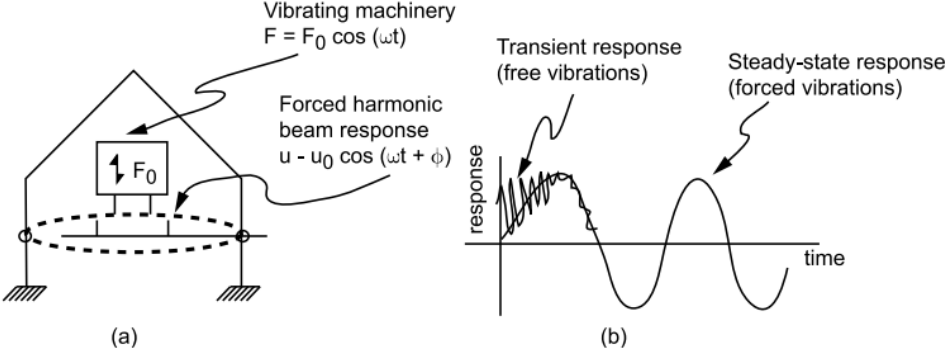


Figure 1.16 Harmonic analysis system from Ansys Structural Analysis Guide [23].

Ansys Mechanical supports full, frequency sweep, and mode superposition methods for harmonic analysis. Mode-superposition method is faster and computationally less expensive than the full and frequency sweep method as it combines the mode shapes (eigenvectors) computed in the preceding modal analysis step to compute the response. A mode-dependent damping ratio can specify different damping ratios for other vibration modes. This method computes the response using Discrete Fourier Transform (DFT) to calculate eigenvectors with the mode superposition method. The detailed mathematical formulation of mode superposition is provided in Appendix A.

1.6 Reduced order modeling

1.6.1 Lumped parameter model and beam frame assembly model

A lumped parameter model, a cyclic chain of spring-mass oscillators, is often used to model a basic bladed disk model. Lumped parameter model oscillators usually have one or two degrees of freedom, one being the motion of the blade and the other related to the disk's motion per sector. Figure 1.17 (a) shows a simple reduced order two DOF lumped parameter model with blades and disk modeled as lumped masses coupled with interblade coupling stiffness k^c [24]. Modeling the system as a lumped mass system is computationally cheaper and can capture some fundamental dynamics, but they only give comparable results to the first three fundamental modes. These models are, therefore, widely used in the preliminary stages of design owing to their simple structure.

In a beam frame assembly model, the blades are modeled as beam frame structures, as shown in Figure 1.17 (b), assembled using a spring-dashpot system to model the rotor. This model has a superior capability of predicting mistuning by using lumped mass at physical coordinates. A simulated annealing algorithm incorporating a structural identification approach is used for every frame arrangement. Although these approaches are simple, they are less accurate than FE models for predicting dynamic responses.

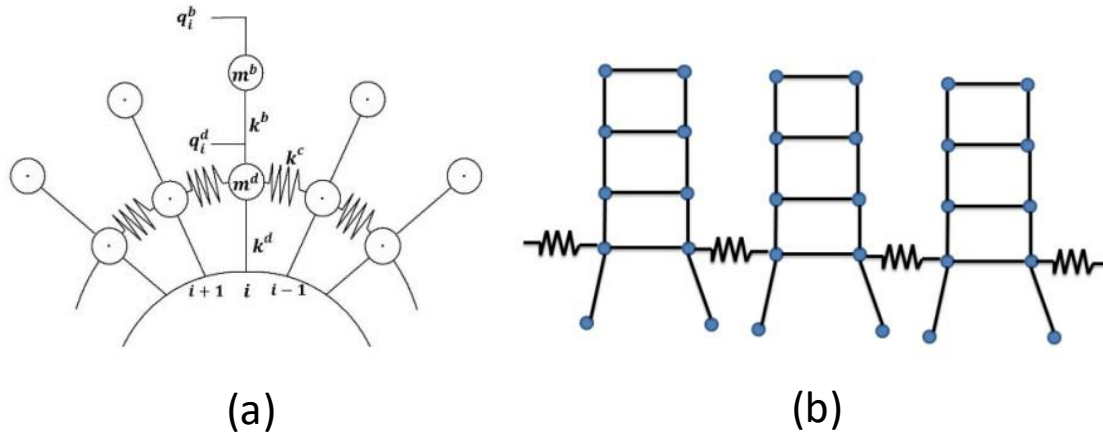


Figure 1.17 (a) Lumped mass parameter model (b) Beam frame assembly model from Yuan et al. [24]

1.6.2 FE-based reduced order models

The central concept for reduction approaches is to swap out the degrees of freedom (DOF) for a collection of global variables that indicate the amplitudes of potential displacement modes. Gladwell [25] used a lumped mass system and assumed the interface between the substructures to be rigid. The lower natural frequencies of each substructure were computed and coupled with Rayleigh-Ritz analysis to represent the complete system. This approach requires the branches or substructures to be chosen appropriately for adequate accuracy.

General formulation of reduced order modeling

A transformation matrix transforms the structure's nodal displacement vector to reduced coordinates. These matrices are generally expressed using Equation (1.22), where X is the physical DOF, and x is the reduced DOF. Transformation or reduction matrices (T) are built with different modes to relate the system's physical DOF to the reduced space DOF. Each reduction technique has a different parameter or set of modes constituting the transformation matrix.

$$X = Tx \tag{1.22}$$

$$M\ddot{X} + C\dot{X} + KX = F_{exc} \tag{1.23}$$

The tilde superscript matrices in Equation (1.25) represent a reduced space after projecting onto the subspace T.

$$T^T M T \ddot{x} + T^T C T \dot{x} + T^T K T x = T^T F_{exc} \quad (1.24)$$

$$\tilde{M} \ddot{x} + \tilde{C} \dot{x} + \tilde{K} x = \tilde{F}_{exc} \quad (1.25)$$

The EOM in reduced space is generally represented as follows,

$$[\mu] \ddot{x} + [c] \dot{x} + [k] x = [\gamma_{exc}] \quad (1.26)$$

Guyan Reduction / static condensation

The Guyan reduction method ignores the inertial equilibrium terms to reduce the number of degrees of freedom of the system to reduce the dimensions of the system. The degrees of freedom to be retained are classified as master DOF, while the degrees of freedom to be omitted are classified as slave DOF. The unloaded DOFs (Slave DOF (x_s)) are expressed in terms of the loaded DOFs (Master DOF (x_m)) as described in the equations (1.27), (1.28), (1.29), and (1.30). This reduction method has a low order of accuracy as it does not include the inertial term and only accounts for the static behavior of the system. This method does not have a general formulation and needs to be optimized for each mode of vibration by manually selecting the master DOF to get results with acceptable accuracy.

$$Kx = f \quad (1.27)$$

$$\begin{bmatrix} K_{mm} & K_{ms} \\ K_{sm} & K_{ss} \end{bmatrix} \begin{bmatrix} x_m \\ x_s \end{bmatrix} = \begin{bmatrix} f_m \\ 0 \end{bmatrix} \quad (1.28)$$

$$K_{sm} x_m + K_{ss} x_s = 0 \quad (1.29)$$

$$x_s = -K_{ss}^{-1} K_{sm} x_m \quad (1.30)$$

$$S = -K_{ss}^{-1} K_{sm} \quad (1.31)$$

Equation (1.31) gives the static condensation matrix (S) with “static modes” in their columns that indicate the static response of master nodes when slave nodes are given a unit displacement. The Linear Guyan transformation matrix is expressed in Equation (1.32).

$$\begin{bmatrix} x_m \\ x_s \end{bmatrix} = \begin{bmatrix} I \\ -K_{ss}^{-1}K_{sm} \end{bmatrix} [x_m] \quad (1.32)$$

$$\begin{bmatrix} x_m \\ x_s \end{bmatrix} = [T_G][x_m] \quad (1.33)$$

$$K_G = T_G^T K T_G \quad (1.34)$$

$$M_G = T_G^T M T_G \quad (1.35)$$

These reduced matrices K_G and M_G are used to compute the vibration amplitude of the system using the EoM.

Craig Bampton Formulation (Fixed Interface Formulation):

The interior and interface degrees of freedom are separated in the substructure EOM, which would reduce the system to a combination of static and dynamic modes. In contrast to the Guyan basis in this formulation, the interface nodes are the master DOF of each substructure, while the interior nodes are the slave DOF. The static response of the system is computed by performing static condensation and giving unit displacement to the interface DOF while all the other DOFs are fixed [26]. The static modes (ψ : attachment modes) computed with static condensation do not contain the dynamic characteristics (ϕ) as they ignore the inertial terms. The dynamic characteristics must be computed by fixing the interface DOFs using Equation (1.38) and included in the formulation.

$$\begin{bmatrix} x_i \\ x_b \end{bmatrix} = \begin{bmatrix} -K_{ii,j}^{-1}K_{ib,j} \\ I \end{bmatrix} [x_b] \quad (1.36)$$

$$v_j = \begin{bmatrix} \psi_j \\ I \end{bmatrix} = \begin{bmatrix} -K_{ii,j}^{-1}K_{ib,j} \\ I \end{bmatrix} \quad (1.37)$$

$$(K_{ii,j} - \omega_r^2 M_{ii,j})\{\phi_{i,j}\}_r = 0 \quad (1.38)$$

$$\phi_j = \begin{bmatrix} \phi_{i,j} \\ 0 \end{bmatrix} \quad (1.39)$$

The equations (1.37) and (1.39) are combined to get the CB (fixed interface formulation) reduction matrix in Equation (1.40)

$$T_j^{CB} = \begin{bmatrix} \phi_{i,j} & \psi_j \\ 0 & I \end{bmatrix} \quad (1.40)$$

Equation (1.41) shows the transformation of physical DOF to Craig-Bampton DOF where $q_{i,j}$ represents the modal coordinate vector associated with the fixed-interface modes.

$$\begin{bmatrix} x_{i,j} \\ x_{b,j} \end{bmatrix} = T_j^{CB} \begin{bmatrix} q_{i,j} \\ x_{b,j} \end{bmatrix} \quad (1.41)$$

$$K_{CB} = T_j^{CBT} K T_j^{CB} \quad (1.42)$$

$$M_{CB} = T_j^{CBT} M T_j^{CB} \quad (1.43)$$

$$K_{CB} = \begin{bmatrix} \Omega & 0 \\ 0 & \tilde{K} \end{bmatrix} \text{ and } M_{CB} = \begin{bmatrix} I & \tilde{M}_{ib} \\ \tilde{M}_{bi} & \tilde{M}_{bb} \end{bmatrix} \quad (1.44)$$

Craig-Chang Formulation (Free Interface Formulation)

The Craig-chang formulation also reduces the system by taking dynamic and attachment modes instead of static modes. The attachment modes have different transformation formulations for a constrained and unconstrained system. Unlike the static modes, the attachment modes are computed with the inverse of the stiffness matrix, the flexibility matrix [27]. When the component is unconstrained, the inverse does not exist; therefore, the rigid body modes are taken to make the matrix non-singular. The attachment modes are computed by applying unit force on the system's interface, while the dynamic modes are computed with an unconstrained interface. The transformation matrices for constrained and unconstrained cases are described in equations (1.45) and (1.46).

$$T_j^{CC} = \begin{bmatrix} \phi_{i,j} & \psi_{b,j} \\ \phi_{b,j} & \psi_{i,j} \end{bmatrix} \quad (1.45)$$

$$T_j^{CC} = \begin{bmatrix} \phi_{i,j} & \psi_{b,b} & \psi_{i,r} \\ \phi_{b,j} & \psi_{i,b} & \psi_{b,r} \\ \phi_{r,j} & \psi_{r,b} & \psi_{r,r} \end{bmatrix} \quad (1.46)$$

The subscript b stands for boundary DOF, i stands for interior DOF, r stands for rigid body DOF, ϕ is the dynamic modes, and ψ is the attachment modes. These transformation matrices reduce the order of the system in the same way as the Craig-Bampton method.

1.7 Mistuning

Structural mistuning is generally included in the system by including mass and stiffness matrix variations. The mistuned mode shapes are the linear combination of the tuned bladed mode shapes. The eigenvalue problem incorporating mistuning is transformed as Equation (1.48).

$$[K + \delta K] - \omega^2[M + \delta M] = 0 \quad (1.47)$$

$$[K + \delta K]\tilde{\phi} = [M + \delta M]\tilde{\phi}\tilde{\Lambda} \quad (1.48)$$

The symbol, $\tilde{\phi}$ is the linear combination of tuned blisk mode shape and $\tilde{\Lambda}$ are the eigenvalues, while δM and δK are the deviations of mass and stiffness from the tuned system, respectively. This research focuses on the Component Mode Mistuning and Fundamental Mode Mistuning models and compares them in the blade-dominated, disk-dominated, and veering regions.

Component Mode Mistuning

CMM combines component mode synthesis and system modes-based approaches by substructuring the blisk into a tuned blisk and mistuned cantilever blade blades, as shown in Figure 1.18. It was first proposed by Lim et al. [28] and then implemented into Ansys Mechanical as a commercial tool with an extension of projecting mistuning into a reduced-order model proposed by Bladh et al. [29]. CMM is implemented with Craig Bampton's approach of a fixed interface to represent the blade motion.

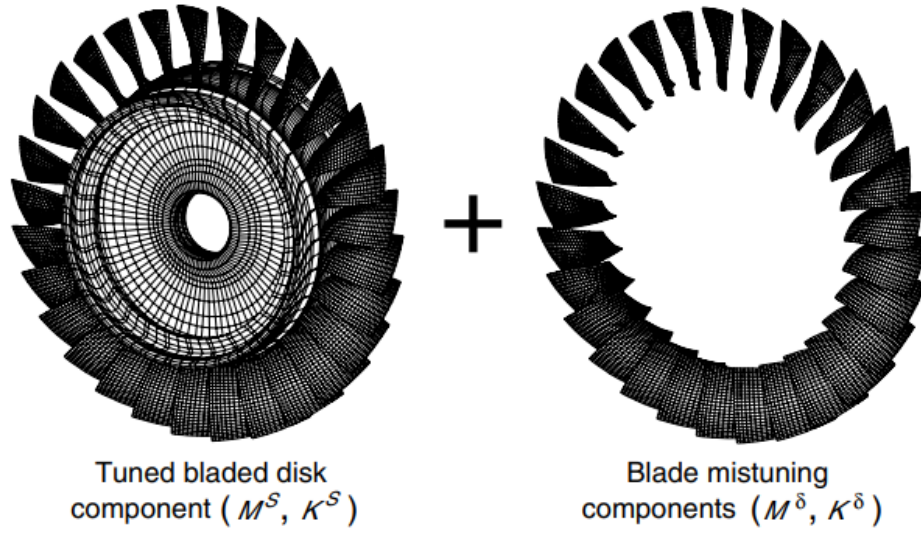


Figure 1.18 Substructuring of a mistuned bladed disk from Bladh et al. [29]

This model assumes small displacements at the blade interface and includes mistuning as a function of stiffness or frequency in modal space. The displacement compatibility constraint satisfied at the blade interface yields a synthesized representation in Equation (1.50) for the mistuned system.

$$(-\omega^2 m + (1 + j\nu)k)x = F \quad (1.49)$$

$$(-\omega^2 [\mu]^{syn} + (1 + j\nu)[k]^{syn}) \begin{bmatrix} X_\phi \\ X_\psi \end{bmatrix} = [\gamma_{exc}] = [\phi\psi]^T F \quad (1.50)$$

The synthesized mass and stiffness matrices are characterized in terms of normal and attachment modes of the tuned system with damping ($j\nu$). The tuned system modes are the normal modes (ϕ), while attachment modes (ψ) are computed using a sequential unit force excitation to each interface DOF. The modes of the mistuned system are computed using a fixed interface approach, simplifying the constraint modes as an identity matrix without any normal modes.

$$[\mu]^{syn} = [\mu]^{tuned} + [\mu]^\delta \quad (1.51)$$

$$[\mu]^{syn} = \begin{bmatrix} I & \phi^T M \psi \\ \psi^T M \phi & \psi^T M \psi \end{bmatrix} + \begin{bmatrix} \phi_b^T \delta M \phi_b & \phi_b^T \delta M \psi_b \\ \psi_b^T \delta M \phi_b & \psi_b^T \delta M \psi_b \end{bmatrix} \quad (1.52)$$

$$[k]^{syn} = [k]^{tuned} + [k]^\delta \quad (1.53)$$

$$[k]^{syn} = \begin{bmatrix} \Lambda & \phi^T K \psi \\ \psi^T K \phi & \psi_b$$

The general formulation of synthesized matrices is given in equations (1.52) and (1.54). Mass and stiffness matrices of a tuned system are represented by M and K , respectively. The deviations of mass and stiffness matrices are represented by δM and δK . The subscript b represents the blade DOF while the eigenvalues of the tuned system and the structural damping are represented by Λ and v , respectively. The CMM method was developed, assuming the blade mistuning is small compared to the tuned system. This assumption enables the mistuned modes to be expressed as a subset of tuned normal modes, which are closely spaced, and therefore the modes out of the frequency range, along with static modes, can be neglected. The synthesized Equation further simplifies as equations (1.55), (4.2), and (1.57).

$$[\mu]^{syn} = [I + \phi_b^T \delta M \phi_b] \quad (1.55)$$

$$[k]^{syn} = [\Lambda + \phi_b^T \delta K \phi_b] \quad (1.56)$$

$$x = [X_\Phi] \quad (1.57)$$

The displacements at the blade-disk boundary cannot be captured with only cantilevered blade normal modes. Therefore, a supplementary mode set (ψ^B) of cantilevered blade interior DOF is included in the formulation whose order corresponds to the number of boundary DOFs. The projection of mass and stiffness of the blade to the boundary modes with modal participation factors (q) and retained tuned cantilevered blade normal and boundary modes (U) are substituted together in equations (1.58) and (1.59) to obtain the complete synthesized matrices for mass and stiffness mistuning.

$$[\mu]^{syn} = I + q^{mT} (I \otimes U^{mT}) \delta M (I \otimes U^m) q^m \quad (1.58)$$

$$[k]^{syn} = \Lambda^s + q^{kT} (I \otimes U^{kT}) \delta K (I \otimes U^k) q^k \quad (1.59)$$

$$U^m = \begin{bmatrix} \phi_b^m & \psi_b^m \\ 0 & I \end{bmatrix} \text{ for mass mistuning} \quad (1.60)$$

$$U^k = \begin{bmatrix} \phi_b^k & \psi_b^k \\ 0 & I \end{bmatrix} \text{ for stiffness mistuning} \quad (1.61)$$

The mode participation factors (q^m and q^k) have one mode which dominates in each column, with the blade motion being dominated by a tuned mode that transforms the equations into a basic form which is solved to compute the eigenvalues.

$$[\mu]^{syn} = I + \sum_{n=1}^N q^{mT} \text{diag}(\mu^\delta) q^m \quad (1.62)$$

$$[k]^{syn} = \Lambda^s + \sum_{n=1}^N q^{kT} \text{diag}(k^\delta) q^k \quad (1.63)$$

Finally, equations (4.2) and (1.63) are substituted in Equation (1.50) to compute the eigenvalues and response. The CMM model incorporated in Ansys Mechanical supports both stiffness and frequency mistuning but does not support geometric and mass mistuning. One of the main disadvantages of this method is that it does not include geometric mistuning with cyclic symmetry ROM which is an essential type of mistuning when non-uniform wear is considered. Mass and geometric mistuning can be investigated using Ansys CMS substructuring reduction. Mistuning of the full blisk model can be achieved by perturbing the mass and stiffness matrices by differing amounts. Stiffness-type mistuning is incorporated by changing Young's modulus of each blade, and frequency mistuning is introduced in the system with a factor to modify each natural frequency, modifying the frequencies in the Craig Bampton reduced stiffness matrix.

$$E_n = [1 + \delta_n]E \quad (1.64)$$

$$\delta f_n = \left[\frac{\omega_{i,mistuned}^n}{\omega_{i,tuned}^n} \right] - 1 \quad (1.65)$$

The APDL command “CYCFREQ, MIST” defines the mistuning for the blade elements in the FEM model.

Fundamental mode mistuning (FMM)

This model was developed by Feiner [30], targeting the isolated family of blade modes. This model does not depend on the geometric or physical aspects that affect the blade frequency. This model uses modal damping ratio, engine order excitation, and tuned system frequencies to compute the forced response without any finite element data like mode shapes and stiffness matrices.

The subset of the nominal modes method is adopted in FMM, which computes the mistuned modes as a weighted sum of selected tuned system modes to reduce the order of the system and transform the structure in terms of sector matrices. This method supports geometric, density, and stiffness types of mistuning by normalizing the equations of motion with the tuned system mass matrix. This method assumes that the mistuned frequencies are closely spaced as SNM considers the same family of modes for reducing the matrices. Therefore, the frequencies are approximated as the average tuned system frequency with deviations and solved using Equation (1.66).

$$[(\Lambda + \delta K) - \omega_i^2(I + \delta M)]\phi_i = 0 \quad (1.66)$$

The symbol Λ is the modal stiffness matrix, I is the modal mass matrix, and ΔK and ΔM are the deviations corresponding to mistuning. The eigenvector (the mistuned mode - Φ_i) corresponds to the mistuned frequency ω_i . A vector weighting factor (β) combines the tuned system modes (ϕ_i) to compute the mistuned system modes.

$$[(\Lambda + \Delta K) - \omega_i^2(I + \Delta M)]\phi_i^o \beta_i = 0 \quad (1.67)$$

The deviation matrices of mass and stiffness are combined into a matrix (A_j) which approximates this matrix into a single mistuning matrix using Equation (1.69) owing to the SNM assumption of this formulation.

$$(\Lambda + A_j)\beta_i = \omega_i^2\beta_i \quad (1.68)$$

$$A = A_j = (\Delta K) - \omega_i^2(\Delta M) = (\Delta K) - \omega_{avg}^2(\Delta M) \quad (1.69)$$

The frequencies of a family of modes are assumed to be closely spaced, which is used to approximate ω_i as the average of tuned system frequencies of a mode family. FMM uses the isolated blade frequency deviations to express terms in a matrix [A] using the sector modes related to cantilevered blade modes. The resulting [A] matrix in Equation (1.71) is a function of DFT and the fractional change in blade frequencies ($\Delta\omega$) whose eigenvalues are computed to find mistuned frequencies (ω_j) and mistuned mode shapes (β_j).

$$A_n = 2\omega_{avg}^2 \left[\frac{1}{N} \sum_{n=0}^{N-1} e^{\frac{2\pi}{N}inp} \Delta\omega_n \right] = 2\omega_{avg}^2 \Omega \quad (1.70)$$

$$(\Lambda + 2\omega_{avg}^2 \Omega) \beta_j = \omega_j^2 \beta_j \quad (1.71)$$

This FMM reduced order model was evaluated for a simplified test rotor with variations of 0.2, 0.8, and 0.008 standard deviations, resulting in a maximum deviation of 1.6% compared to the completely mistuned Ansys model. This model's simple formulation and low computational cost can be taken advantage of by understanding its limitations.

1.8 Research Objectives

This research aims to study the CMM and FMM reduced order models and understand the limitations of these reduced order models when applied to Purdue 3-stage rotor blisk. The CMM model is incorporated in Ansys Commercial, while the FMM model is an in-house code by Leng [31]. Rotor 2 of the PAX100 configuration was chosen as the geometry for this study since it has been thoroughly investigated for the forced response as part of the GUIde Consortium. Full blisk models are computationally expensive and are not a viable choice in the early design stages. It would be highly beneficial to take advantage of the FMM method, which has a computational cost similar to a mass-spring model to predict the response. Therefore this study will guide future modeling of different setups knowing the limitations and accuracy of each model, leading to a reduction in the computational cost to evaluate a mistuned system. This research focuses on determining model fidelity in the regions of high disk participation and veering. Including aerodynamic effects will allow for future validation of the experimental data.

This objective is accomplished by simulating the reduced order models for various mistuning values and comparing the results to the mistuned full blisk model, which acts as a benchmark. A grid convergence investigation was first carried out for the FEM models to confirm the accuracy of the spatial discretization. Next, the modal frequencies and forced response of these mistuned reduced order models are computed and compared with full mistuned blisk for five mistuning cases of 0.1%, 0.5%, ping test values, 5%, and random deviation. This study focused on the 1B and 1T blade modes. The accuracy of reduced models depends on the number of the retained blade and tuned system modes. The average error is computed for these models as a function of modes retained to recognize the minimum requirement for a family of modes. To compare amplification, these models are simulated with similar excitation forces at engine orders 3, 5, and 11. The deviations used in the 5% standard deviation case are arranged in ascending order and compared to the original case to investigate a case of intentional mistuning.

2. COMPUTATIONAL METHODOLOGY

Two computational models, one of the full blisk and the other of sector geometry, were developed to study the vibration characteristics of Rotor 2. The models were mistuned by introducing deviations in Young's modulus, translating into equivalent deviations in the stiffness for a linear isotropic system. This chapter describes the setup of the computational model and the mistuning test cases with various standard deviations. Gridpro was used to mesh, and Ansys Mechanical with APDL command sequence was used to solve these cases. Matlab was used to further compile and post-process the data.

To study the sole effects of mistuning, forced response in this study is uncoupled with the fluid interaction. Therefore, this study does not include the stiffness and damping matrices modifications due to unsteady fluid interactions. The effect of these interactions can be incorporated into these models in the preceding steps using the mapped pressure results from transient CFD to generate a loading vector for harmonic analysis instead of a constant load excitation used in this study.

2.1 Purdue 3-stage Axial Compressor Facility

Three axial stages follow an inlet guide vane (IGV) in the Purdue 3-Stage axial compressor, a scaled model of the backstages of a modern high-pressure compressor. The flow path of the compressor is illustrated in Figure 2.1. With a corrected design speed of 5000 rpm, the compressor matches the Reynolds numbers and Mach values that are characteristic of the rear stages found in engines. The IGV and rotor blade profiles are double circular arc (DCA) configurations, while the stator blade profiles are the NACA 65-series airfoil design. A 1400-horsepower three-phase alternating current motor powers the compressor with an encoder on the shaft and feedback control to maintain the speed within 0.1% of the target speed. In this facility, different configurations of Stator 1, as summarized in Table 2.1, can be used to study the engine order influence on the resonant response of Rotor 2. The baseline configuration of this compressor consists of IGV (Inlet guide vane), Stator 1 (S1), Stator 2 (S2) with 44 vanes, Stator 3 (S3) with 50 vanes and Rotor (R1), Rotor 2 (R2) and Rotor 3 (R3) with 36, 33 and 30 vanes, respectively.

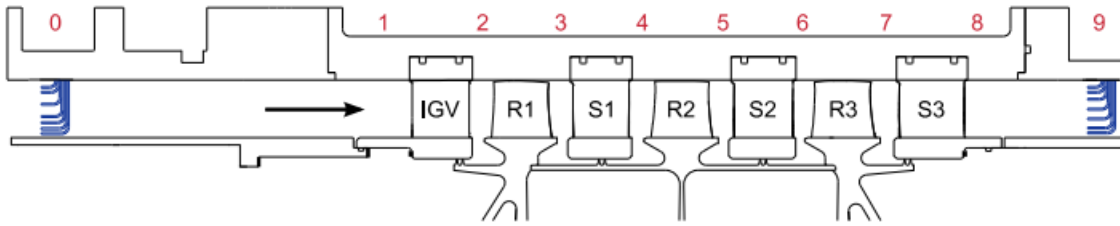


Figure 2.1 Purdue 3-stage axial compressor flow path

The experiments can be designed to study steady-state and transient aerodynamics near the mechanical resonant conditions of R2. The full vane passage characteristics are captured through a circumferential traverse of the stator vanes, which are individually indexable. Matthews [31] studied the unsteady aerodynamics at resonant conditions for three engine order crossing speeds. Concurrently, Aye-Addo [32] studied the forced response for the Baseline and Non-Uniform Vane spacing configurations as a part of GUIde 5. Detailed documentation of the Purdue 3-stage axial compressor setup, data acquisition systems, and data processing techniques can be found in the referenced thesis.

Table 2.1 PAX100 compressor Configurations

Configuration	IGV	R1	S1	R2	S2	R3	S3
Baseline	44	36	44	33	44	30	50
Reduced Vane count	44	36	38	33	44	30	50
Non-uniform vane spacing (NUVS)	44	36	38 (18 and 20 vane sectors)	33	44	30	50

The Nodal diameters that are excited by these configurations are summarized in Table 2.2

Table 2.2 Excitation Orders on Rotor 2 in different configurations

Case	Configuration	S1	R2	S2	Nodal Diameter Excitations
1	Baseline	44	33	44	11
2	Reduced Vane count	38	33	44	5,11
3	Non-uniform vane spacing (NUVS)	38 (18 and 20 vane sectors)	33	44	3,7,11

2.2 FEM models

A single sector with cyclic boundary conditions is computationally more efficient for tuned systems as it can be expanded into a full model. Premeshed cyclic symmetry defines the independent cyclic DoFs and dependent cyclic DoFs, ensuring that the mesh matches between high and low sides with similar transformations, as shown in Figure 2.2. The matched faces corresponding to the periodic rotational boundaries must have the same topology and geometry with equal surface area. Blade elements and Interface nodes are defined using named selections in the CMM model as interior blade DoF and interface DoF to mistune the system. Defining the blade interface is extremely important for the reduced models as these models compute the blade modes excluding other bodies to compute the frequencies of the mistuned system.

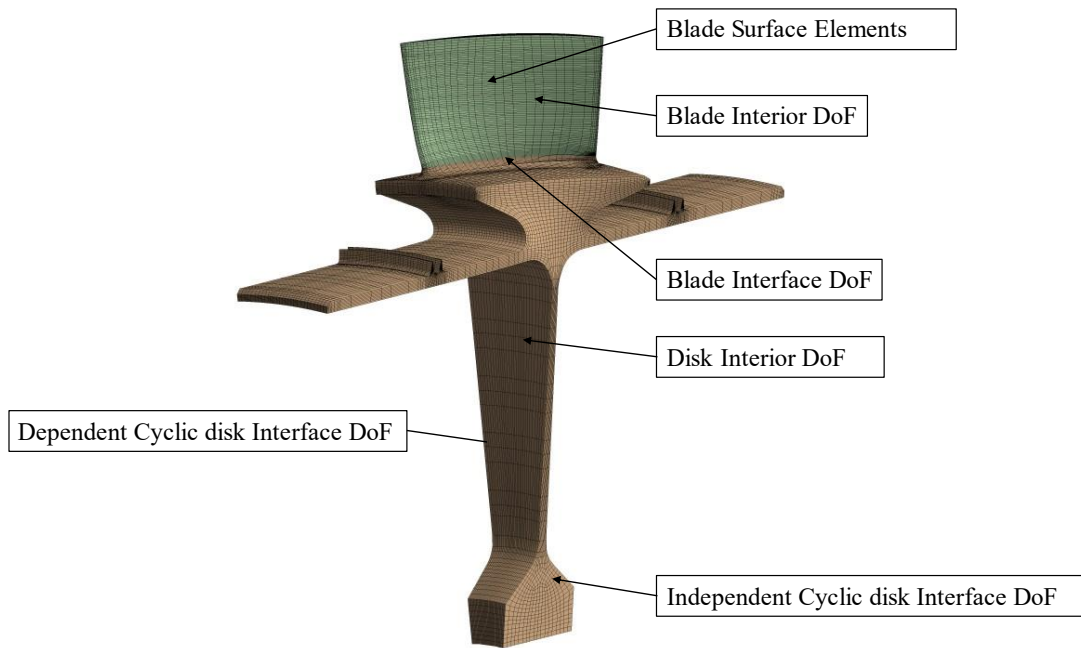
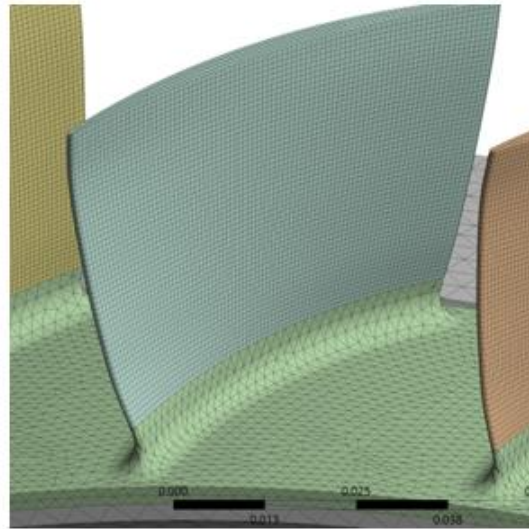


Figure 2.2 Single Sector FEM model

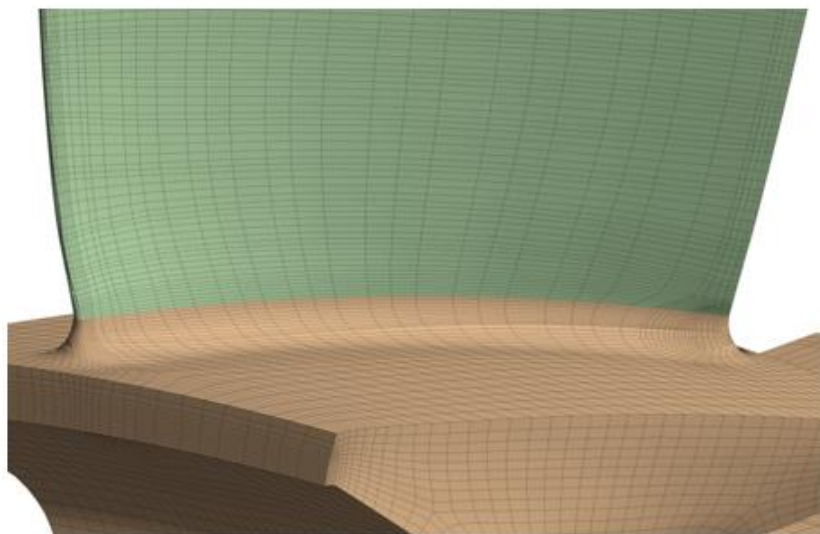
This study includes features like fillets and chamfers in the model, which are usually excluded in previous studies to simplify the models. An initial mesh was generated on a sector model using Ansys. The geometry was split into three parts (blade, hub, and root) to achieve a sweepable blade and root, which can be meshed with higher-quality hexahedral elements. The fillet could not use a hex-dominant meshing and, therefore, was meshed as tetrahedral elements. Ansys does not support the multizone meshing feature with the match control in the cyclic symmetry constraint, thereby restraining the meshing, resulting in a lower-quality mesh. The splits created additional bonded contacts between the bodies, introducing errors in the results. Meshes made in Ansys Mechanical and GridPro in the hub and fillet region are illustrated in Figure 2.3.

A FEM model of the full blisk was developed in Ansys to compare the results and understand the mesh dependency of these structural results. The full blisk was meshed using two approaches to compare. Meshing the full blisk as an entire body and expanding the sector mesh in Ansys with bonded contacts were attempted to generate a full blisk FEM model. Comparing results between the full blisk and sector FEM models showed a large discrepancy between the tuned frequencies. The full blisk mesh model was comparatively better for overall frequencies than the

expanded mesh, which was only conformal in the blade-dominated regions. These errors further propagated into the harmonic analysis to the extent that they could not be used for comparison.



(a) Ansys mesh in the hub region with fillet.



(b) GridPro mesh

Figure 2.3 GridPro mesh in the hub and fillet region.

Further refinement of the grid was not feasible due to the size of the full blisk DOF problem. These issues necessitated a Gridpro structured mesh. Gridpro was used to create a structured mesh for the cyclic model with 10.90909 degrees periodicity.

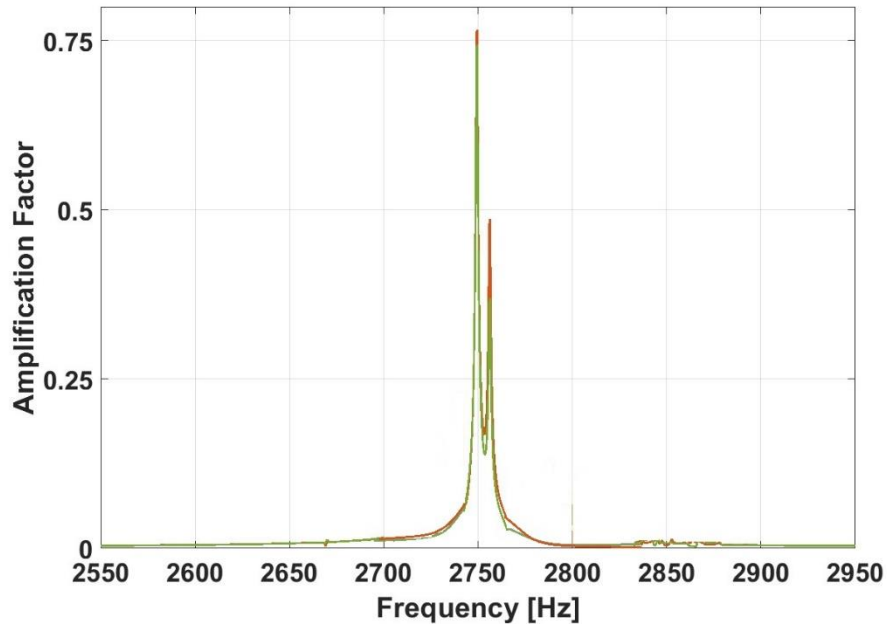


Figure 2.4 Effects of inherent mistuning on forced response due to the mesh.

Gridpro was initially used to create a topology and mesh the full blisk model. Gridpro optimized the grid to the CAD geometry at each node introducing an inherent mistuning. This inherent mistuning affected the response to the extent that taking this geometry as a benchmark for validation would not be an accurate comparison of these models. The effects of this inherent mistuning introduced by the mesh are illustrated in Figure 2.4. Multiple peaks indicate that the mode of this blade is excited with several modes, which implies mistuning. Considering these effects, the full blisk FEM model was generated for a single sector and then expanded by merging the nodes on the periodic surfaces to create a tuned system, as shown in Figure 2.5.

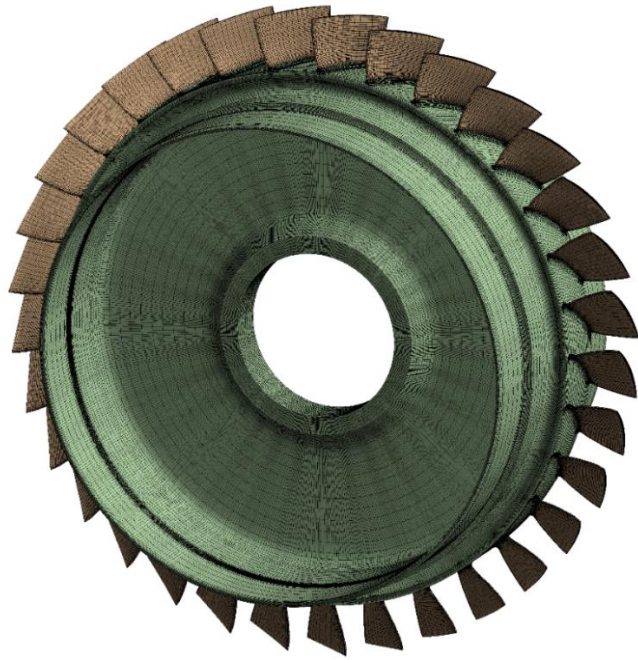


Figure 2.5 Full Blisk FEM model

Young's modulus of each blade was changed to mistune the FE models by defining new proportional material properties for each blade. For simplistic comparison, the FEM models are excited by a unit harmonic pressure forcing function loaded at each blade's pressure surface. A traveling wave force is considered for the blade DOF only, allowing for a more compact formulation. The probe location to monitor and compare forced response was chosen as a point near the trailing edge tip, as described in Figure 2.6.

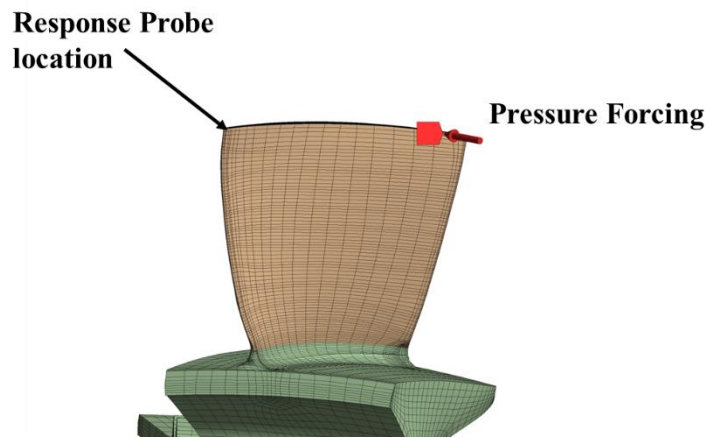


Figure 2.6 Forcing and response probe location of the FE models

The rotor model is fastened at the disk's outermost surfaces, roughly approximating the boundary conditions imposed by adjacent stages. The response amplitude is directly proportional to the magnitude of force, but the amplification factor used for comparison between the FMM and CMM models is independent of this factor. The specific nodal diameter with respect to engine order is simulated by including an associated phase angle to the respective force on each blade of the blisk. The interblade phase angle is computed for each nodal diameter as follows,

$$IBPA = \frac{2 \pi ND}{N_{blades}} \quad (2.1)$$

2.3 Mistuning cases

The cantilevered blades are mistuned proportionally with isotropic blade variations. Variation in Young's modulus matrix includes stiffness variations in the blades using the relation in Equation (2.2). The delta is computed using the system's ratio of mistuned and natural frequencies to include frequency mistuning.

$$E = E_o (1 + \delta) \quad (2.2)$$

$$\delta = \frac{\omega^2 - \omega_n^2}{\omega_n^2}, \quad \text{for frequency mistuning} \quad (2.3)$$

Mistuning patterns with standard deviations of 0.1%, 0.5%, 0.45% SD (Ping test results), 5% SD, an arranged 5% SD case, and random mistuning cases are used to study FMM and CMM models are described in Figure 2.7 and Figure 2.8. The reduced order models have higher accuracy for low levels of mistuning in general; therefore, high variations are also included in this study to understand the errors.

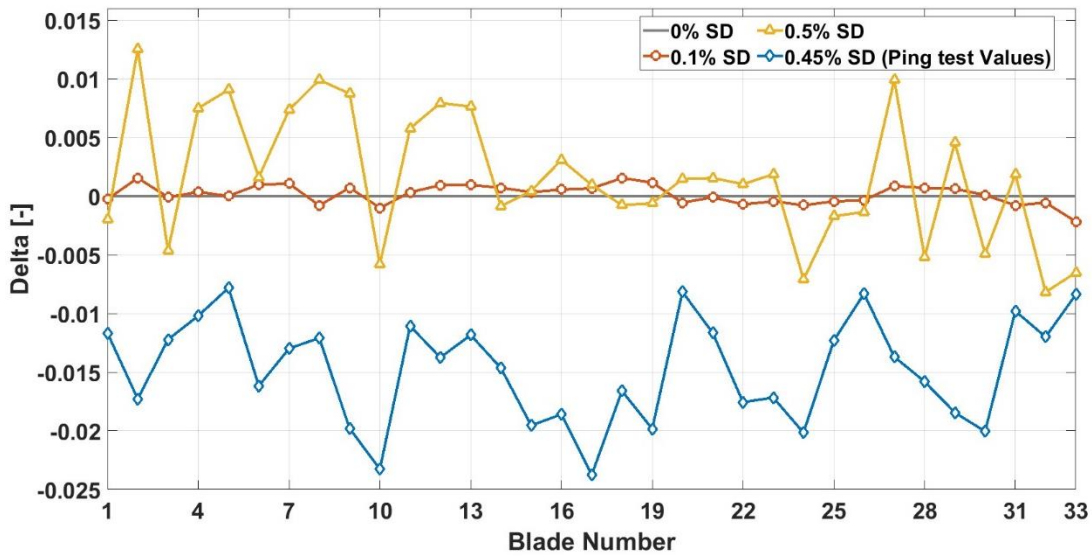


Figure 2.7 Mistuning pattern for a case study with small proportional mistuning

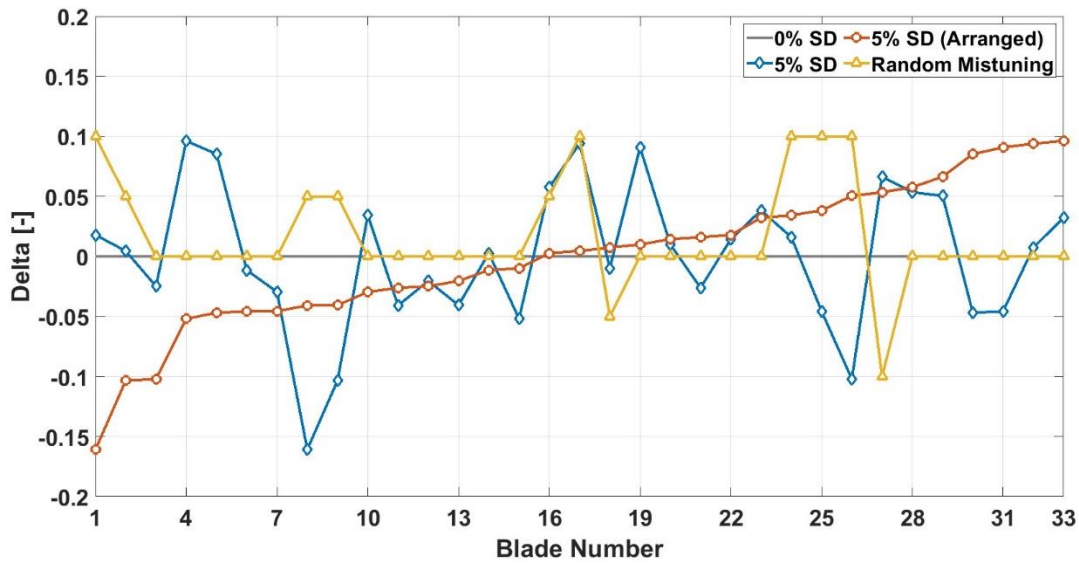


Figure 2.8 Mistuning pattern for a case study with proportional mistuning.

Ansys APDL command sequence

Ansys Mechanical does not directly implement the CMM model of mistuning as a method. APDL command sequence is used to implement it into the Mechanical module. The static structural analysis with cyclic symmetry must have cyclic symmetry with the mode superposition option turned on using the “CYOPT, MSUP, ON” command to set up the analysis for harmonic analysis in the later stages. APDL command sequence was also used to include the variations in

the stiffness matrix and selection of blade modes, along with exporting the modal participation factors and the results.

3. SIMULATION AND RESULTS

3.1 Grid Convergence Study

A grid convergence study must be used to assess the models to verify the FEM models of the tuned system. A coarse mesh is computationally less expensive but typically results in a higher numerical error, while a fine mesh can provide us with a numerical solution that is more accurate, but it is more computationally expensive, has longer run times, and requires more memory. The number of equations to be solved for the current problem is of order three; therefore, doubling the number of elements will increase the size of the matrices by three times. A balance between computational cost and quality is carefully examined and chosen to get an optimal mesh refinement. Higher accuracy with optimal mesh can be achieved with local mesh refinement around complex geometry. Table 3.1 describes the element count and associated number of equations (DOFs) used in the grid convergence study.

Table 3.1 Mesh elements and number of equations for grid convergence study

	Single Sector Model	Number of Equations (Sector Model)	Full blisk Model	Number of Equations (Full blisk Model)
Coarse mesh	21300	74715	702900	2465595
Medium mesh	58832	199011	1941456	6567363
Fine mesh	151986	496746	5015538	16392618

The most straightforward comparison that can be made for structural analysis is to compare the frequencies. The natural frequencies of the first four modes as a function of the number of elements are plotted in Figure 3.1(a). The maximum difference between the medium and fine mesh for the first 200 frequencies was around 0.8%, as illustrated in Figure 3.1(b). Note that this grid convergence study was conducted for the tuned system case with the same boundary conditions and at 100% speed. Some leniency is given for the structural analysis, which is relatively less mesh dependent than CFD models. A convergence criterion of less than 1% was chosen, considering the computational cost of the full blisk model.

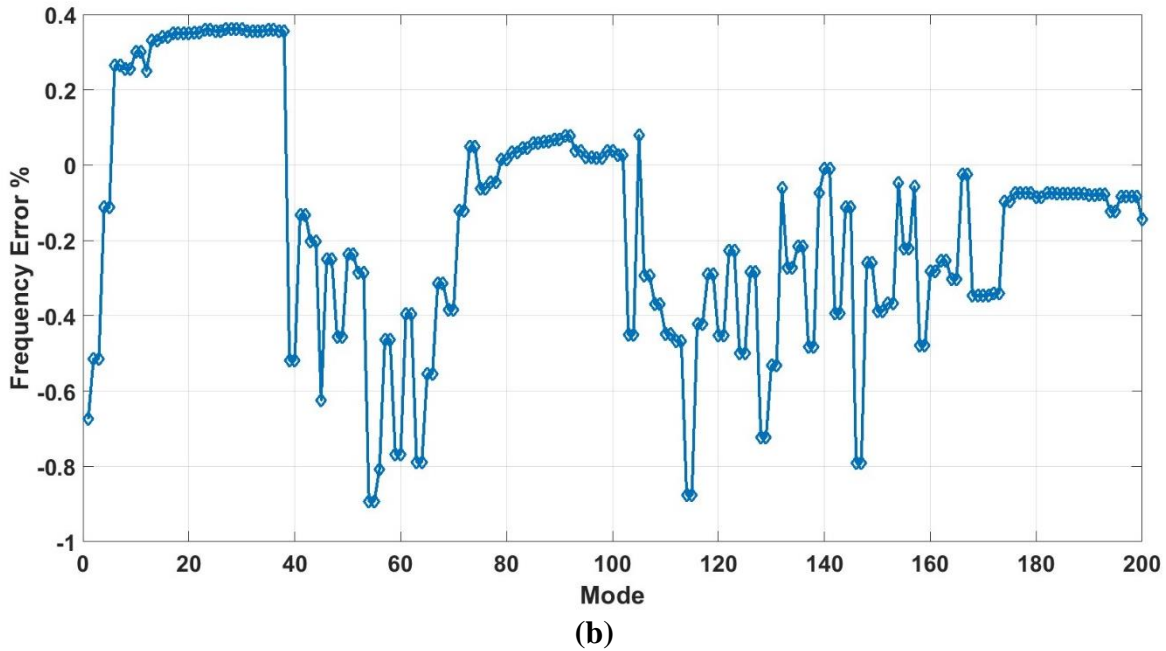
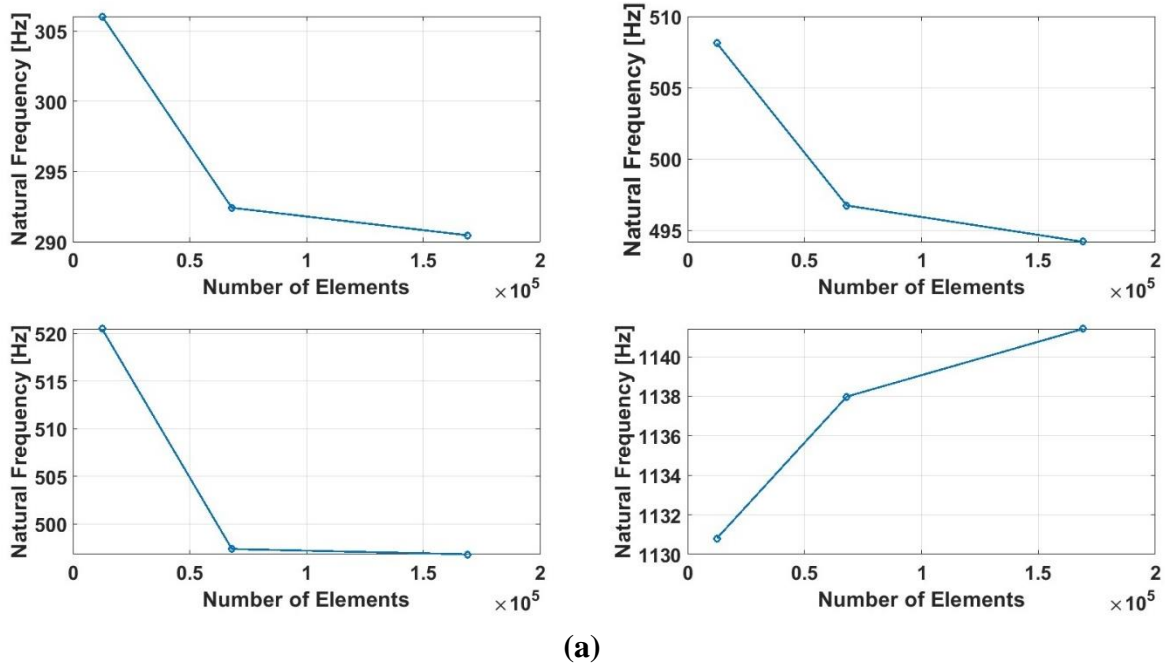


Figure 3.1(a) Natural frequency of first four tuned system modes as a function of mesh size (b) Percent error between Medium and Fine meshes of the first 200 modes

The Grid Convergence Index (GCI) method developed by Celik et al. [33] is widely used to estimate the grid discretization error in CFD grids. This method uses the Richardson extrapolation to compute a higher-order solution. This method was adapted to structural analysis

to conduct a detailed grid convergence analysis of these FE models. The grid refinement decreases the discretization error, and the solution asymptotically approaches the Richardson's Extrapolation higher-order approximation. GCI (Grid Convergence Index) estimates the error for each grid with respect to Richardson's extrapolation, where the grid sizes with N elements are defined using Equation (3.1) for a volume (V). The grid refinement factor (r) greater than 1.3 was chosen as recommended, as shown in Table 3.2. The grid spacing is normalized by h_{fine} .

$$h = \left[\frac{\sum_{i=1}^N \Delta V_i}{N} \right]^{1/3} = \left[\frac{V}{N} \right]^{1/3} \quad (3.1)$$

$$r = \frac{h_{coarse}}{h_{fine}} \quad (3.2)$$

Table 3.2 Spacing and Grid refinement factor of the FE models.

	Coarse mesh	Medium mesh	Fine mesh
Normalized grid size (h_{norm})	0.51945	0.7288	1
Grid Refinement Factor	1.4031	1.3721	

The Richardson extrapolated and GCI values of ϕ are computed using equations (3.3) and (3.4), respectively.

$$\phi_{ext}^{21} = \frac{r_{21}\phi_1 - \phi_2}{r_{21} - 1} \quad (3.3)$$

$$GCI_{21} = \frac{1.25 \left(\left| \frac{\phi_1 - \phi_2}{\phi_1} \right| \right)}{r_{21}^p - 1} \quad (3.4)$$

GCI_{21} measures the percent error between solutions using fine and medium meshes, while GCI_{32} measures the percent error between solutions using medium and coarse meshes. The GCI values and the frequency error relative to the extrapolated values of the first 50 modes for each grid refinement are plotted in Figure 3.2 and Figure 3.3.

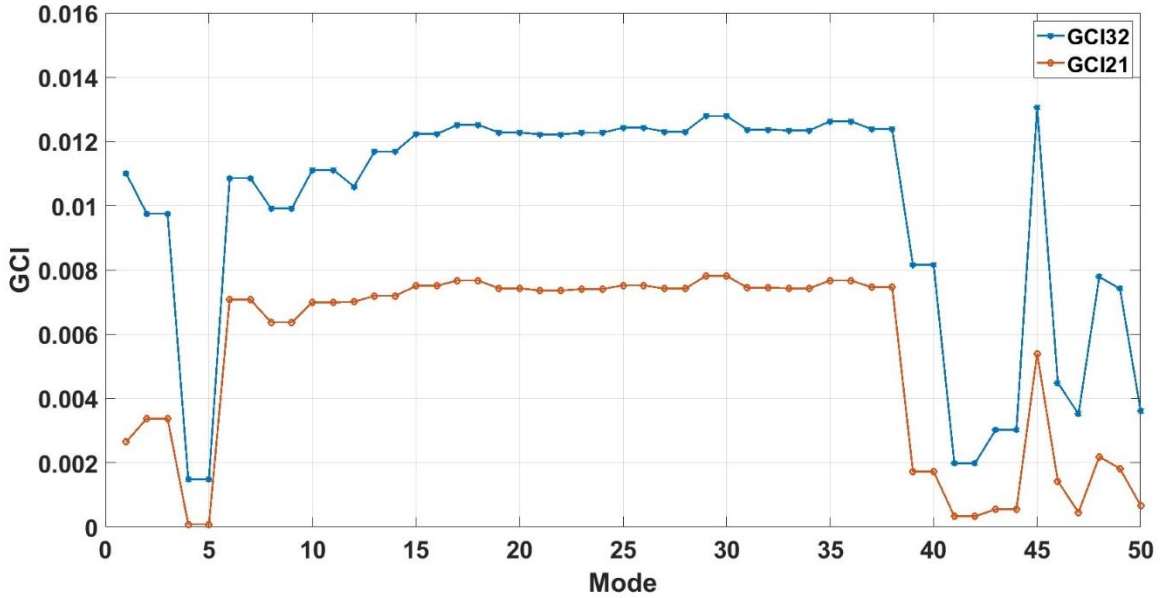


Figure 3.2 GCI for the first 50 modes

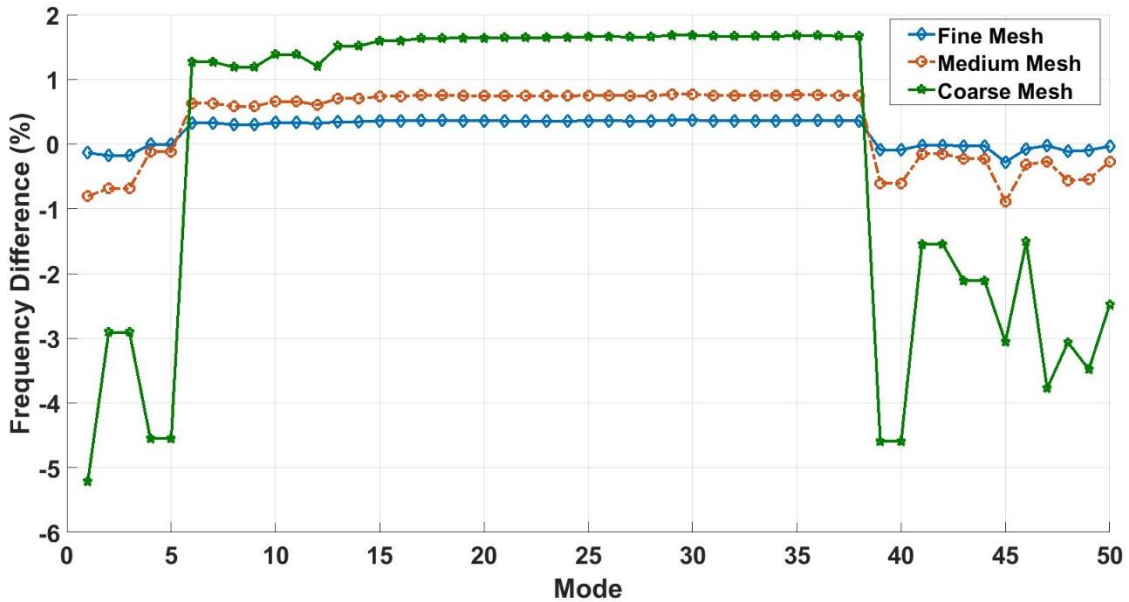


Figure 3.3 Frequency error percent relative to the extrapolated frequency for different levels of grid refinement.

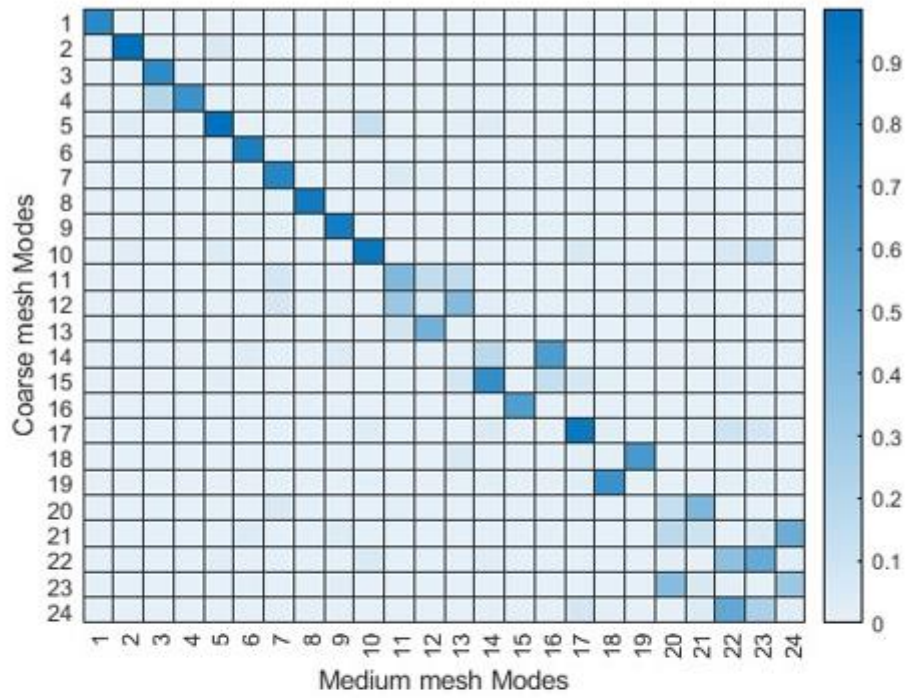
It is crucial to verify the mode shapes and frequencies to quantify the convergence adequately. Modal Assurance Criterion (MAC) is often used with natural frequency convergence criterion as an additional assurance factor for validation.

Modal Assurance Criterion (MAC)

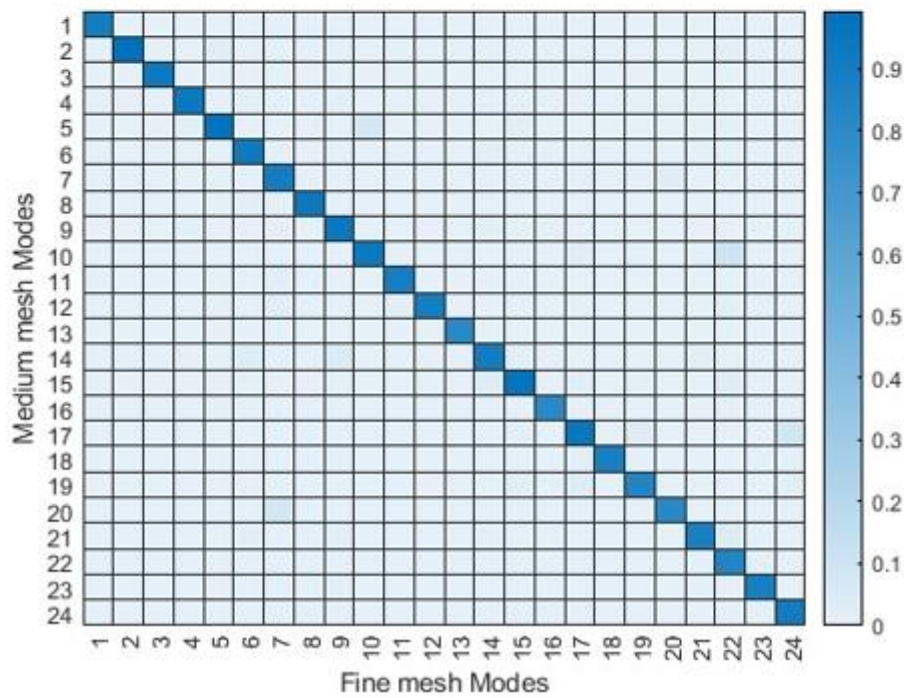
The modal assurance criterion is often used to relate the mode shapes and provides a correlation between vibration shapes with lower sensitivity to minor differences. The normalized scalar product of the two sets of vectors $\{\phi_A\}$ and $\{\phi_B\}$, as described in Equation (3.5), is used to calculate the MAC value [31]. The MAC matrix with computed elements is constructed from the resulting scalars, which can take a value between 0 and 1. Zero represents no consistent correlation between the mode shapes, and one represents a consistent correlation.

$$MAC(i, j) = \left[\frac{|\{\phi_A^T\}_i \{\phi_B\}_j|^2}{(\{\phi_A^T\}_i \{\phi_A\}_i)(\{\phi_B^T\}_j \{\phi_B\}_j)} \right] \quad (3.5)$$

The modal assurance criterion can only represent consistency without any information about validity or orthogonality. If similar errors exist in both solutions, MAC will still have good consistency; therefore, this method cannot identify incomplete vectors and local discrepancies. The cases where there are sufficient degrees of freedom to distinguish independent modes without any unmeasured forces on the system and noise in the system, the MAC can be used as an indicator of validity [32]. Ansys Mechanical computes the MAC and matches the nodal solutions from two results files using the “RSTMAC” APDL command. The MAC values are computed by mapping the solution from one grid to the other by specifying node tolerances. MAC was applied to compare the coarse, medium, and fine mesh modal shapes on the first 24 modes. The computed MAC values are plotted in Figure 3.4. While the medium and fine mesh has a good correlation between them, the medium and coarse mesh has a good correlation for the lower modes but loses accuracy for higher modes. The worst case in the medium and fine mesh was mode 16 with a MAC value of 0.8. Further mesh refinement could drive the MAC matrix to unity, but the expanded full blink model would be computationally too expensive for comparison.



(a)



(b)

Figure 3.4 MAC Matrices ((a) Coarse and Medium mesh, (b) Medium and fine mesh)

As the full blisk FEM model is an expanded cyclic symmetry FEM model, the GCI's and MAC grid convergence analysis give similar values as that of the cyclic symmetry model in the tuned case. The relative difference between the cyclic symmetry tuned system and the full blisk tuned system for the different grids is shown in Figure 3.5. A relative error of $10E-4$ magnitude did not affect the GCI and MAC values for the fullblisk system compared to the cyclic symmetry system for these grids.

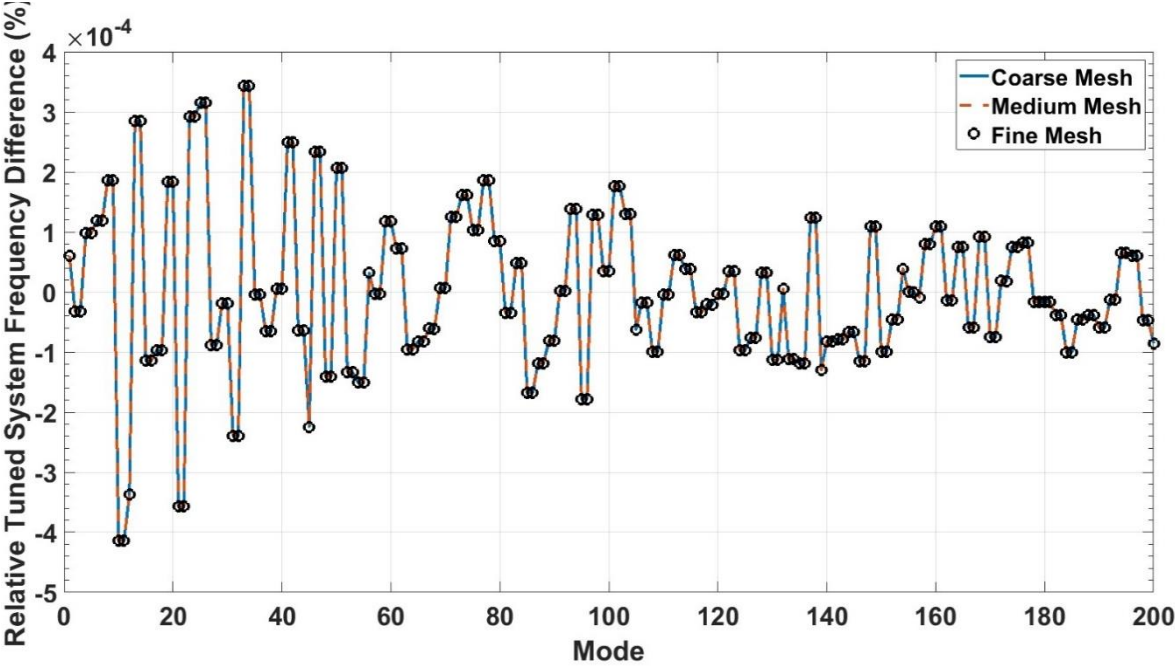


Figure 3.5 Relative Frequency Error for different grids.

The overall comparison of MAC values, GCI, and error percent in the frequencies showed that the medium mesh was optimal. Refining the mesh 2.6 times between fine and medium mesh increased the accuracy by only 0.4%, which is very small compared to the exponential increase in the computational cost.

3.2 Comparative Studies

The tuned system modes corresponding to the nodal diameter are shown in Figure 3.6. The veering regions corresponding to nodal diameters 3 and 5 are primarily excited in Purdue 3-stage

compressor and were chosen along with the first bending and torsion mode corresponding to ND 11 to study these reduced-order models.

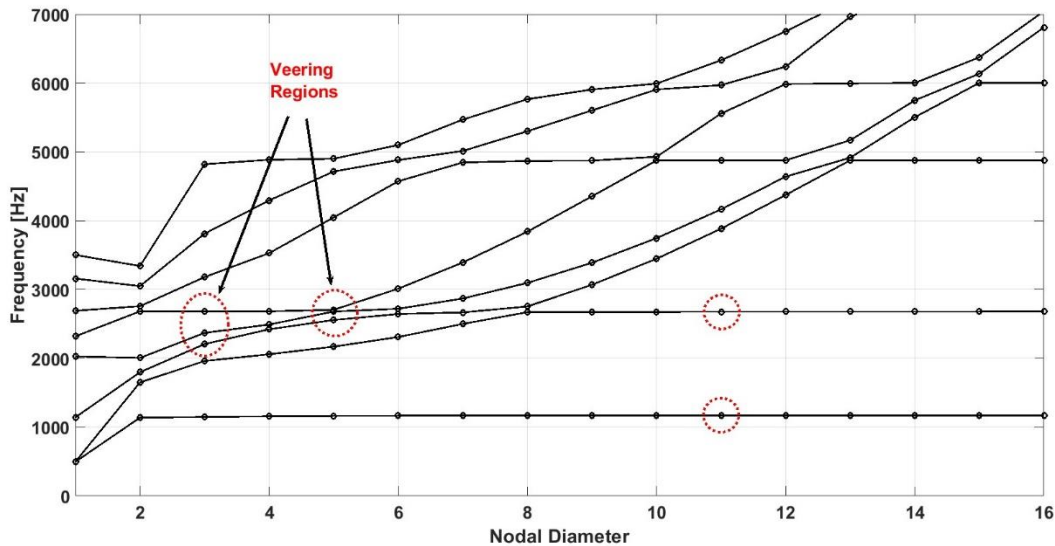


Figure 3.6 Tuned system modes.

3.2.1 CMM Method - Effect of Tuned system modes (TSM) and Cantilever blade modes (CBM)

CMM formulation uses a combination of TSM and CBM modes to compute the harmonic response of the system. Therefore it is essential to understand the influence of the number of modes. Retaining isolated family modes and retaining all the computed modes were compared with the full blisk frequencies. Retaining the isolated family modes is a computationally efficient choice in cases where mistuning is very small and frequencies of the mistuned system are very closely spaced, making the forced response a strong function of the family of modes.

An optimal mistuning of 0.5% standard deviation is chosen to study the influence of the retained blade modes and tuned system modes. To ensure that the effects of these parameters are evident and distinguishable, a comparatively higher standard deviation is chosen than in past studies. This decision was also made as this deviation is close to ping test deviation values, which would be used for validation in the future. The frequencies for a system with small deviations are closely spaced; therefore, the changes would be minimal to understand the effects. A structural

damping coefficient of 0.001 is considered in this study to compute the response, which is an average found using NSMS data in previous studies.

Tuned system modes (TSM)

The Ansys CMM method retains all the tuned system modes computed in the initial modal analysis with cyclic symmetry. The retained modes are selected by targeting a frequency range and specifying the number of modes to be computed. The frequency errors with different TSM, including ten cantilever blade modes, were computed for the first 200 modes. Overall, isolating the mode families gave better results than retaining all the solutions when fewer modes were targeted to be retained, which can potentially reduce the computational cost. Interestingly, retaining a higher number of modes does not give good results when the number of modes retained is less than 300. The errors introduced by retaining the lower frequency family are compensated by including the higher frequencies of the following family, as illustrated in Figure 3.7. The relative error and percent error of the frequencies are calculated using equations (3.6) and (3.7).

$$error = f_{full\ blisk} - f_{CMM} \tag{3.6}$$

$$error\ \% = \left(\frac{f_{full\ blisk} - f_{CMM}}{f_{full\ blisk}} \right) * 100 \tag{3.7}$$

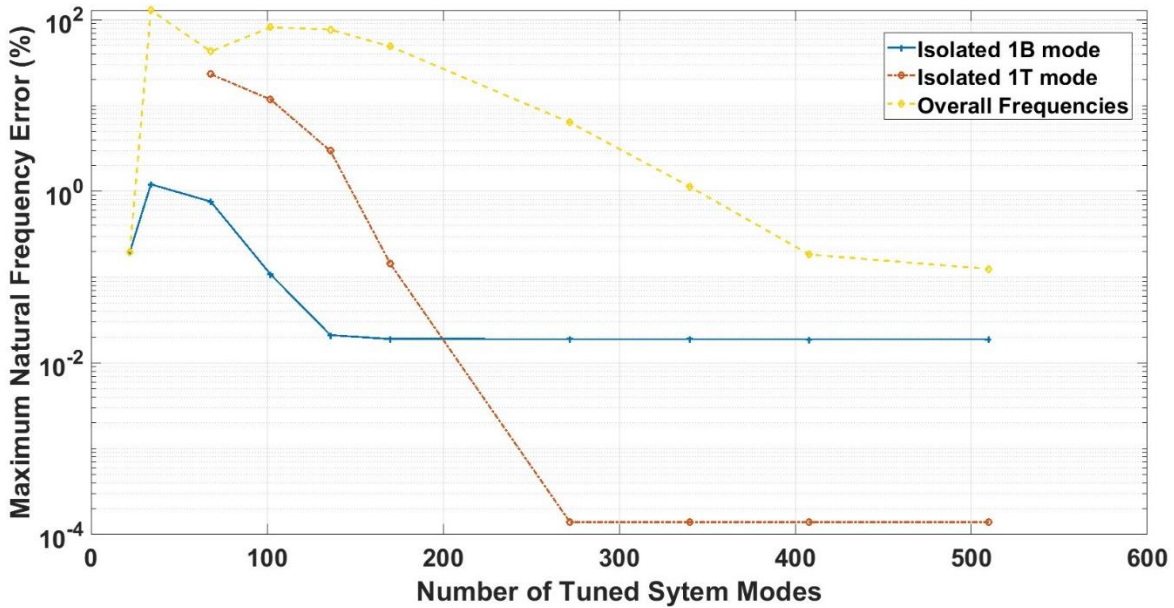


Figure 3.7 Effect of the number of tuned system modes retained (10 CBM).

Cantilevered blade modes (CBM)

Ansys computes the cantilevered blade modes using the specified blade elements and interface surface in the CMM method. The number of modes retained can notably impact the frequencies and response. The error is higher for frequencies not retained in the blade modes. Figure 3.8 depicts the relative frequency error and percent error calculated for ND 11, retaining the bending mode for the 1 CBM case.

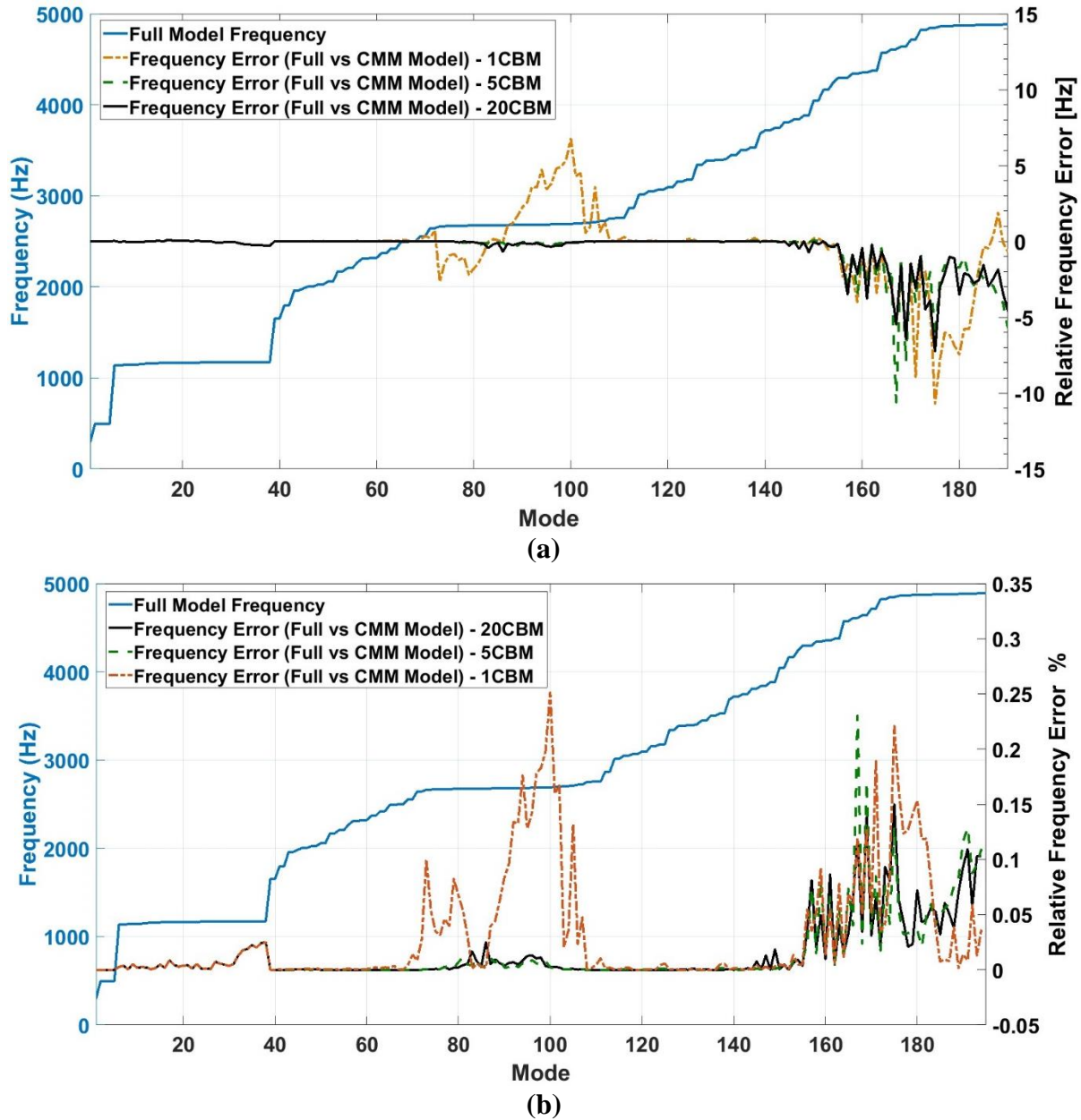


Figure 3.8 (a) Relative frequency error (b) Relative frequency error percent (ND 11) Note: Modal frequency is mapped to the left ordinate and the errors are mapped to the right ordinate.

Since the blades are mistuned in the system, significant errors exist in the blade-dominated frequencies and areas with low disk participation. Retaining only one cantilever blade mode can give comparable results for the sweep range of the same mode. This property can be used to optimize the number of retained modes with information about the target mode. The amplification factor for each blade is calculated using Equation (3.8) to compare the responses for each case.

$$A_{max,blade} = \frac{\max(\overline{x_{mistuned,blade}})}{\max(\overline{x_{tuned}})} \quad (3.8)$$

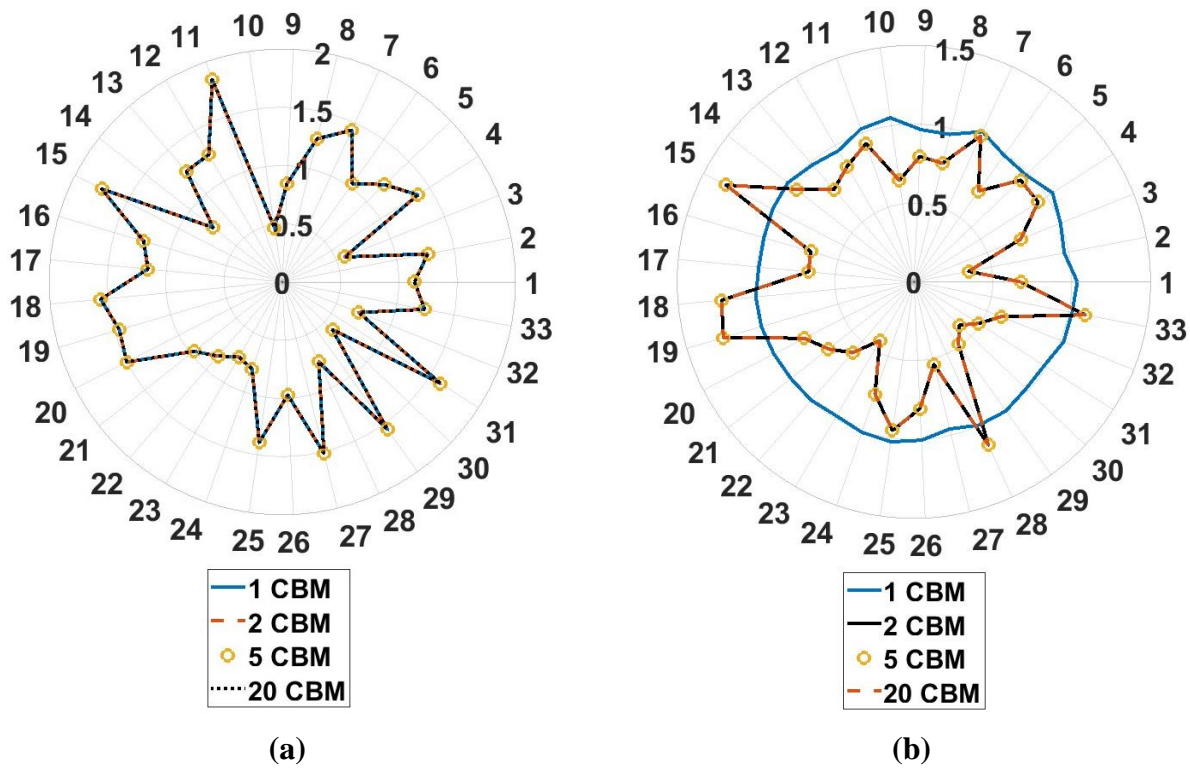


Figure 3.9 (a) Blade amplification factor for the first bending mode (b) Blade amplification factor for the first torsion mode (Retaining Bending Mode)(ND 11)

The retained bending mode gives good results for the bending mode, as shown in Figure 3.9 (a). Despite a tiny error of 0.25% in the frequency, retaining a different mode can significantly underestimate or overestimate the response, as illustrated in Figure 3.9 (b). In the second case, the bending mode of CBM is retained for the torsion mode sweep range to understand the influence of CBM.

A similar analysis is done for the first torsion mode at ND 5, which lies in the veering region and has a possible energy exchange between modes when the system is mistuned. As expected, the CMM model predicts the frequency within 0.3% error which is slightly higher than the blade-dominated mode in the preceding case. The error decreases monotonically with increased retained CBM, as illustrated in Figure 3.10. A similar trend of CBM affecting the forced response of the blade when a different blade mode is retained is shown in Figure 3.11. This trend indicates that for the CMM model, the TSM is insufficient to estimate the response and must include the participating CBM modes as minimum input to compute a comparable response.

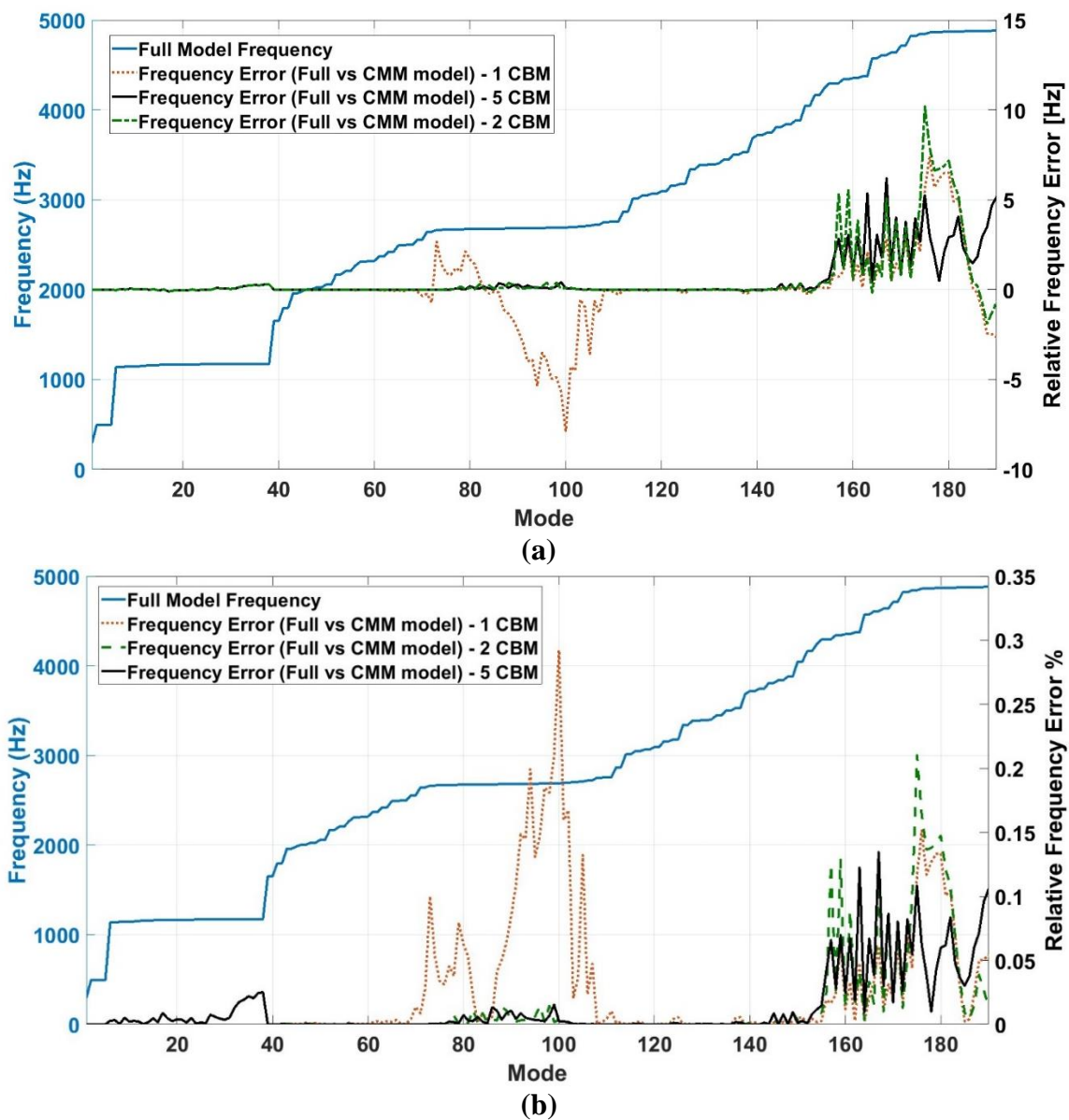


Figure 3.10 (a) Relative frequency error (b) Relative frequency error percent (ND 5).

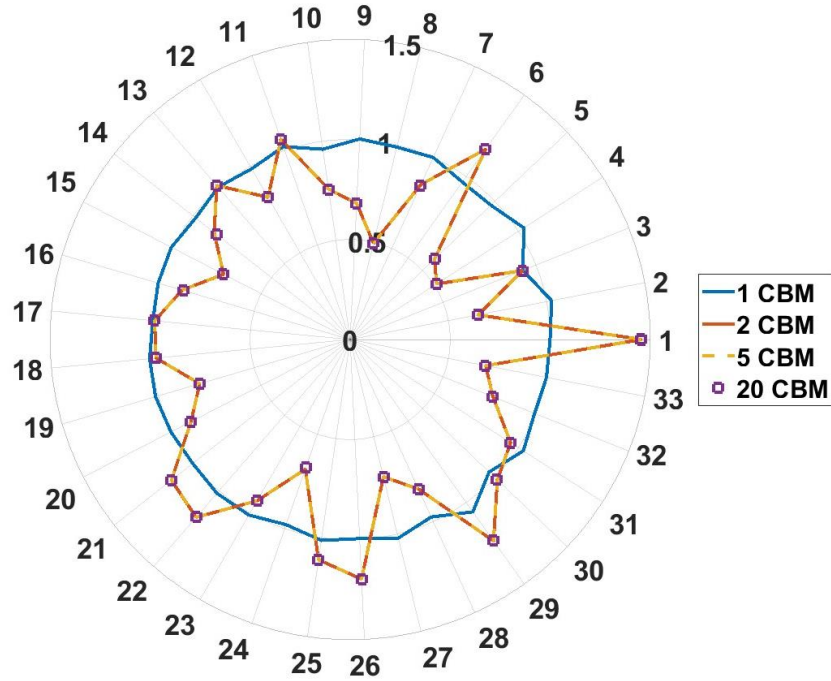


Figure 3.11 Effect of CBM on the forced response for the first torsion mode (ND 5)

The cases with high variations or nonproportional mistuning can have modal participation from numerous modes from a different family of modes. To ensure we capture this probable participation, at least one additional mode family must be included on either side of the modes considered. The cases of 400 TSM and 10 CBM are chosen to ensure that the complex behavior is captured and results are comparable for high mistuning cases, which can have several modes participating in the response.

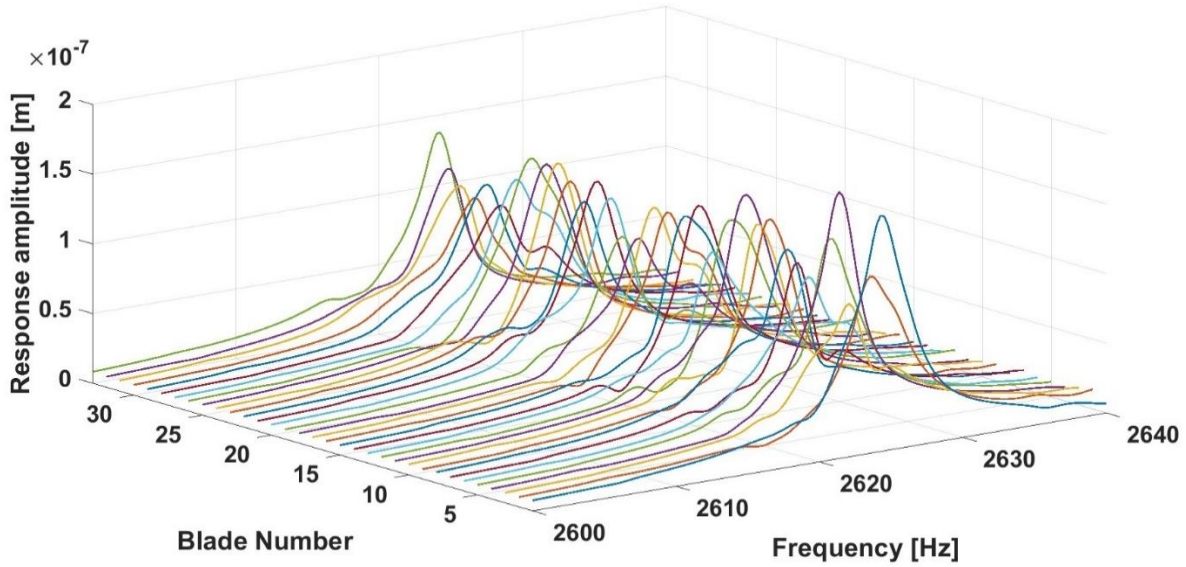
3.2.2 Small Mistuning Cases

Standard Deviation 0.1% (Nodal Diameter 11)

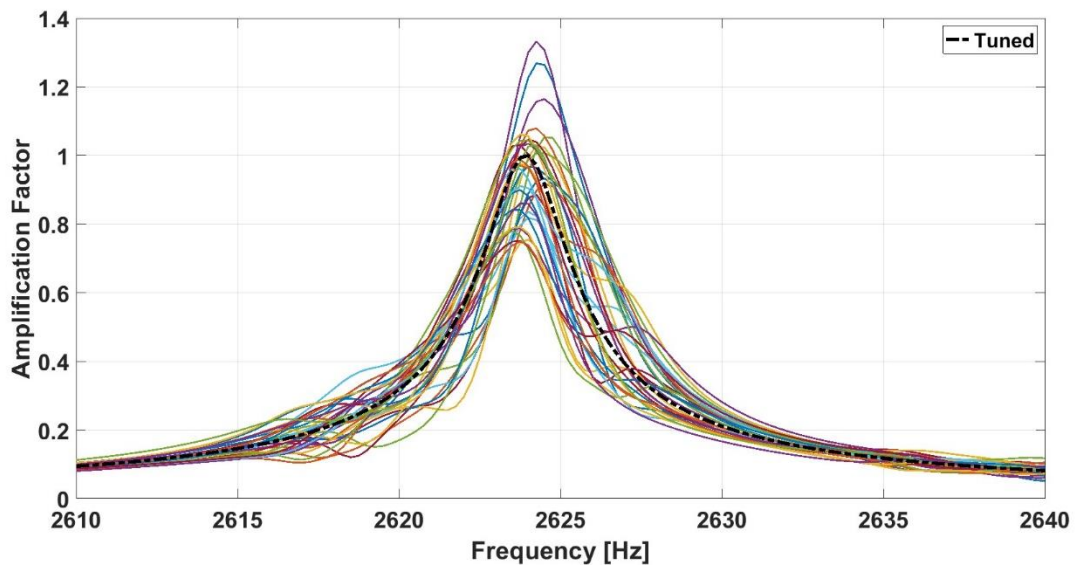
The cases with small mistuning can be adequately modeled with fewer modes, as the frequencies and response would be close to a tuned system. The response and amplification factor of the system with 0.1% standard deviation relative to the tuned system response of the full blisk of first torsion mode excited at ND 11 corresponding to EO 44 are shown in Figure 3.12 (a) and

(b). The response of each blade is normalized with the maximum tuned response to find the amplification factor through the sweep, using Equation (3.9).

$$A_{sweep,blade} = \frac{\overline{x_{mistuned,blade}}}{\max(\overline{x_{tuned}})} \quad (3.9)$$



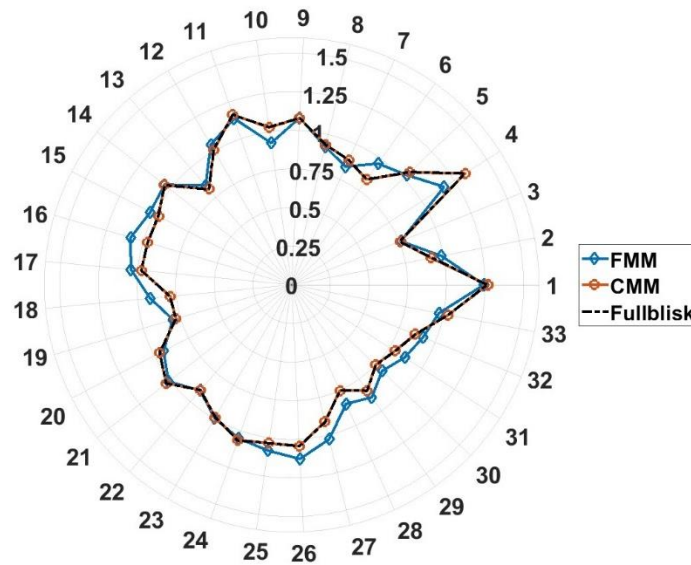
(a)



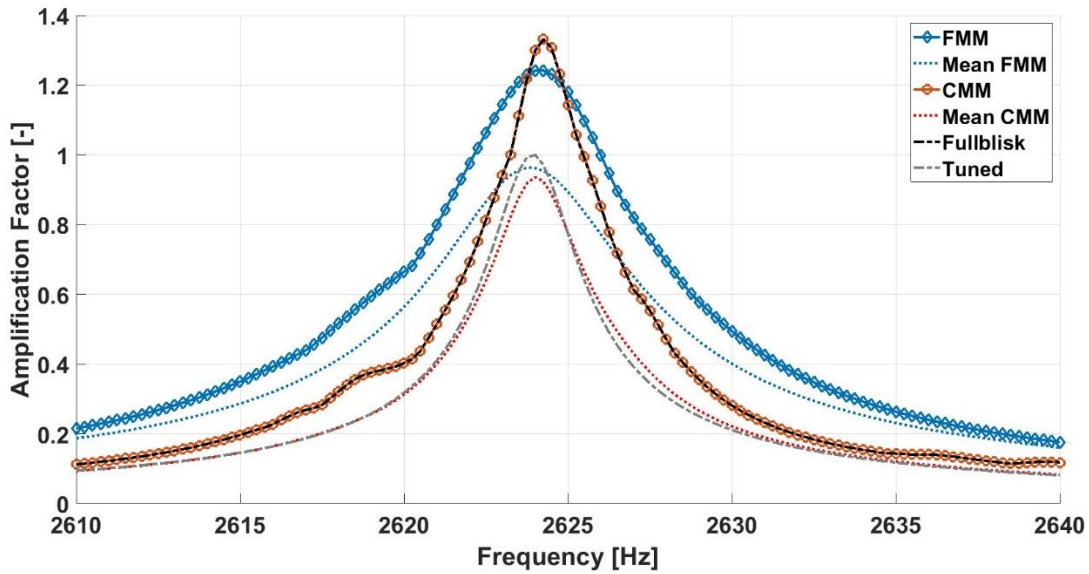
(b)

Figure 3.12 (a) Forced Response and (b) Amplification factor of Rotor 2 with 0.1% standard deviation mistuning (Full blisk - First Torsion Mode).

The mistuned frequencies, in this case, are closely spaced, and no significant frequency split is observed. The amplification factors calculated for each blade using CMM and FMM models are illustrated in Figure 3.13 (a). Despite being a very low-order model, the responses estimated by FMM have a reasonable correlation with the full blisk response. A minimal discrepancy of about 0.4% between CMM and full FEM results exists. Note that the CMM results closely match the full FEM results and appear as overlapped lines in the plot at the represented scale.



(a)



(b)

Figure 3.13 (a) Blade Amplification Factor and (b) Maximum response envelope (First Torsion Mode)

The maximum forced response envelope is the maximum response of the whole system corresponding to each frequency in the sweep range. The maximum mistuned forced response envelope normalized with the tuned response of each model using Equation (3.10) is plotted in Figure 3.13 (b).

$$A_{sweep} = \frac{\max (\cup \max (\overline{x_{mistuned,blade}}))}{\max (\overline{x_{tuned}})} \quad (3.10)$$

While FMM underestimated the peak amplification factor by about 0.089, CMM estimated it well. Overall, FMM estimates the individual blade responses pretty well for this case. The modal participation factor, commonly referred to as mode multiplier, measures a mode's contribution to a structure's reaction to force or displacement excitation in a particular direction and is plotted for the full blisk in Figure 3.14. The sum of the absolute values of these factors normalizes the modal participation factors. The normalized modal factors identify the dominant modes at a particular frequency. The mistuned modes, in this case, are prominently only excited by the modes in the same family. The cases where the response is the superposition of the same family of modes are excellent for the FMM model that considers the isolated mode family to calculate the responses.

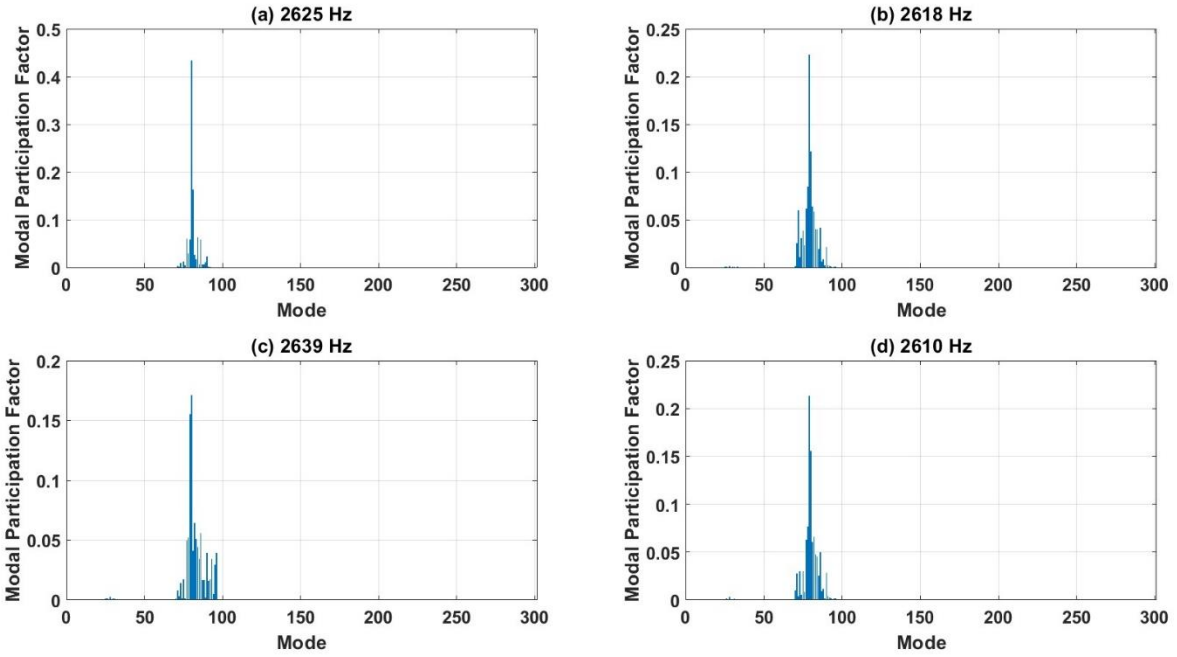
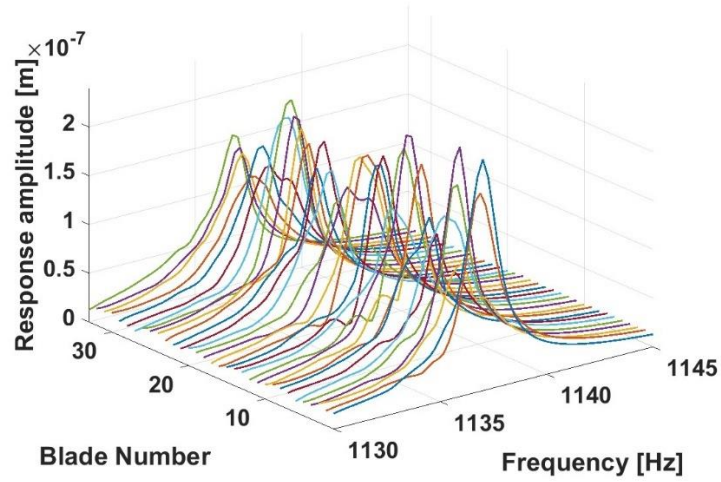
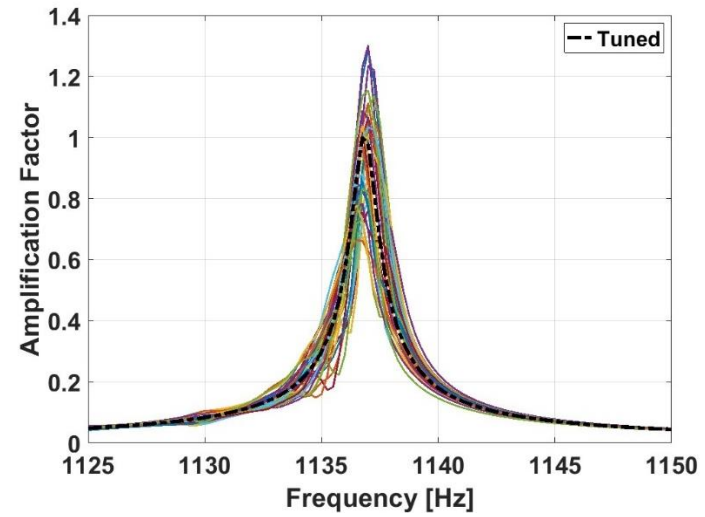


Figure 3.14 Modal participation factors (First Torsion Mode)

Similar results for the first bending mode are shown in Figure 3.15, Figure 3.16, and Figure 3.17.



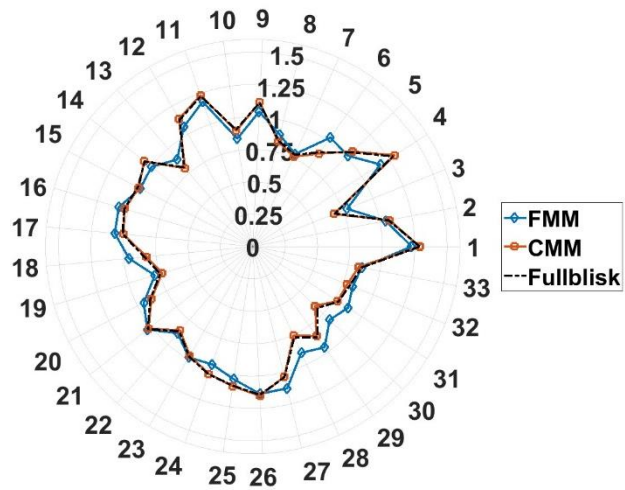
(a)



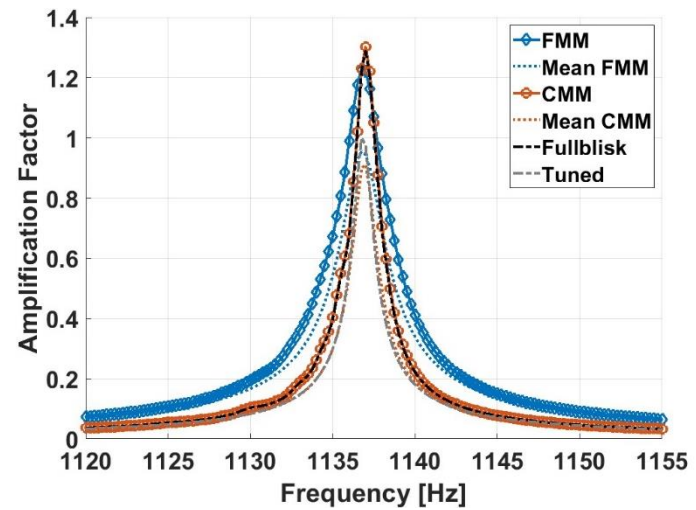
(b)

Figure 3.15 (a) Forced Response and (b) Amplification factor of 0.1% SD (Full blisk - First Bending Mode).

75



(a)



(b)

Figure 3.16(a) Blade Amplification Factor and (b) Maximum response envelope (First Bending Mode)

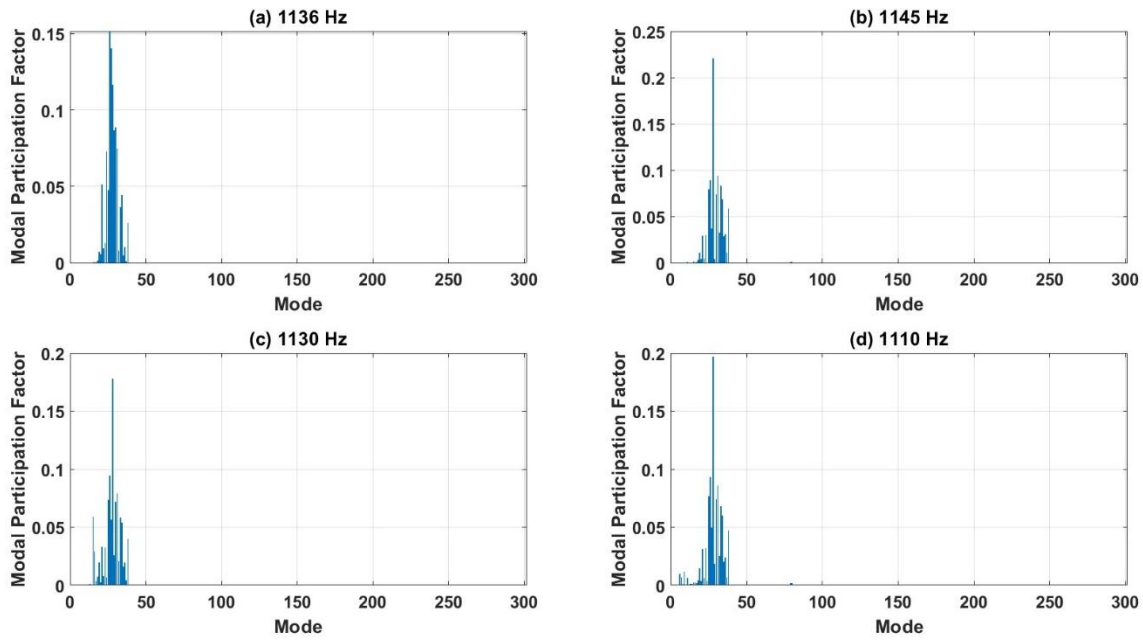


Figure 3.17 Modal participation factors (First Bending Mode (ND 11))

A similar modal participation factor and correlation trend are present for ND 3 and 5 with small mistuning. The sweep region corresponding to the torsion mode at ND 3 and ND 5 lies in the region of veering and consists of closely spaced modes with disk participation. An evident response is not observed at some resonant frequencies in this region, indicating that the corresponding frequency is majorly disk dominant. Therefore, the monitoring probe on the blade could not capture such displacements. Since only deviations in the properties of blades are considered in these reduced order models, disk dominant frequencies experience negligible effects of mistuning.

FMM formulation cannot simultaneously predict responses at all frequencies like CMM and full blisk model in the veering region due to its structure. Therefore, each frequency in this region is isolated, taking the corresponding mode family. This formulation would not consider the effects of modes from other families that might sometimes participate in the response. The mistuned frequencies predicted by the reduced-order models are shown in Figure 3.18. FMM and CMM accurately estimate the mistuned frequencies for this case, especially for the bending mode. The maximum error in the frequency prediction was less than 0.5 percent. Note that the FMM, CMM, and full blisk results appear to overlap due to the scale of the plot.

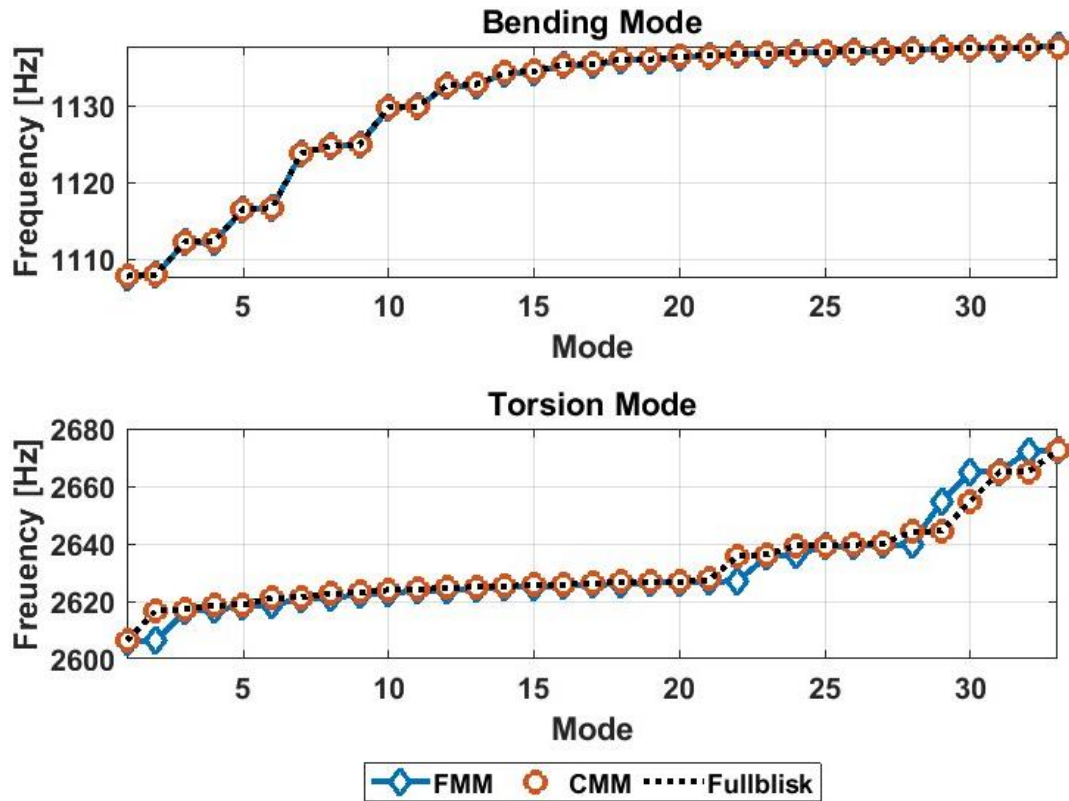
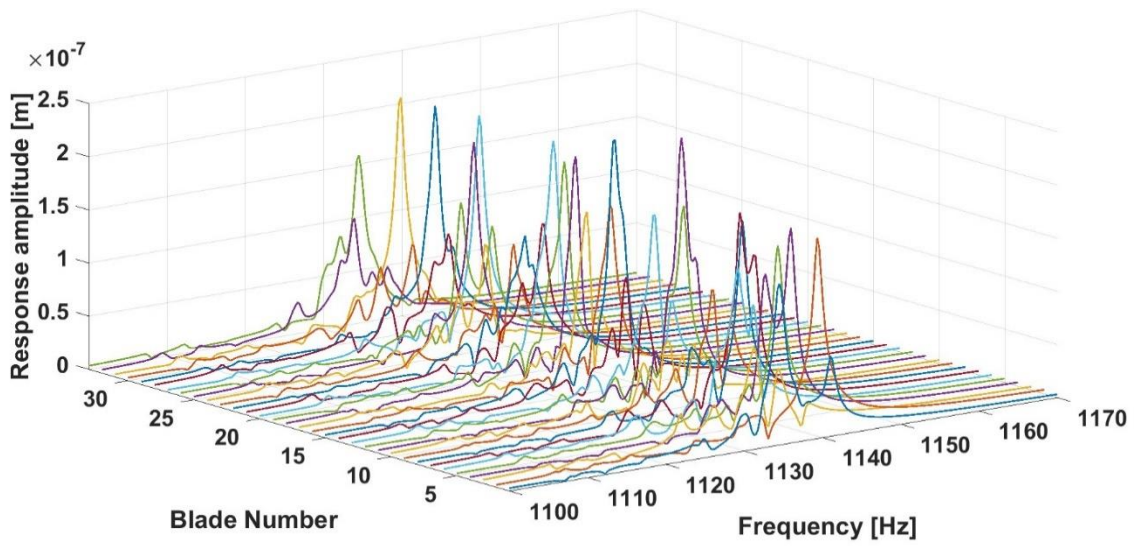


Figure 3.18 Mistuned frequency (0.1% SD).

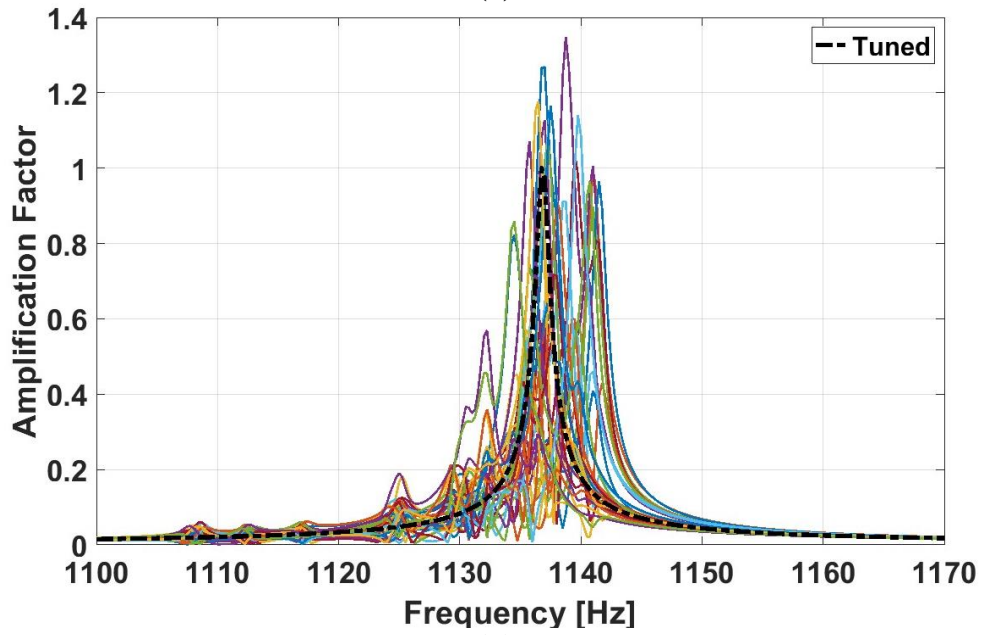
The veering regions corresponding to ND 5 and ND 3 are studied in detail with a higher standard deviation in mistuning values to explore the limitations of these models when there is substantial modal participation from other modes.

Standard Deviation 0.5% - Nodal Diameter 11

The effects of mistuning are evident in this case, with a significant change in the frequency response band. Additional peaks correspond to mistuned blade frequencies in the response and amplification factor, as depicted in Figure 3.19. The frequency excited at ND 11 is blade dominated; therefore, there is a significant increase in the frequency band.

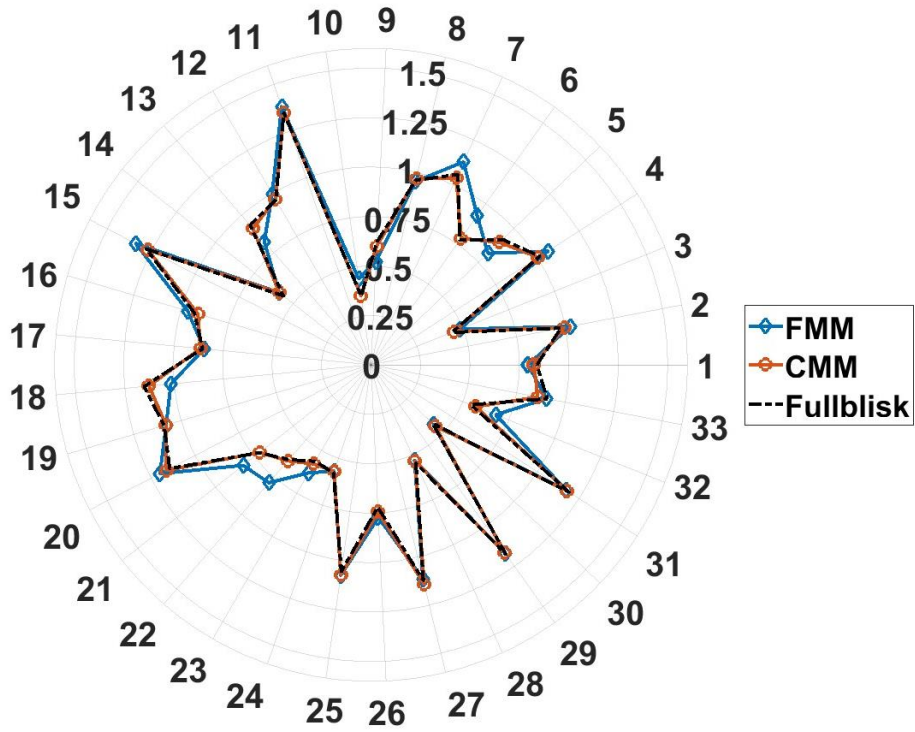


(a)

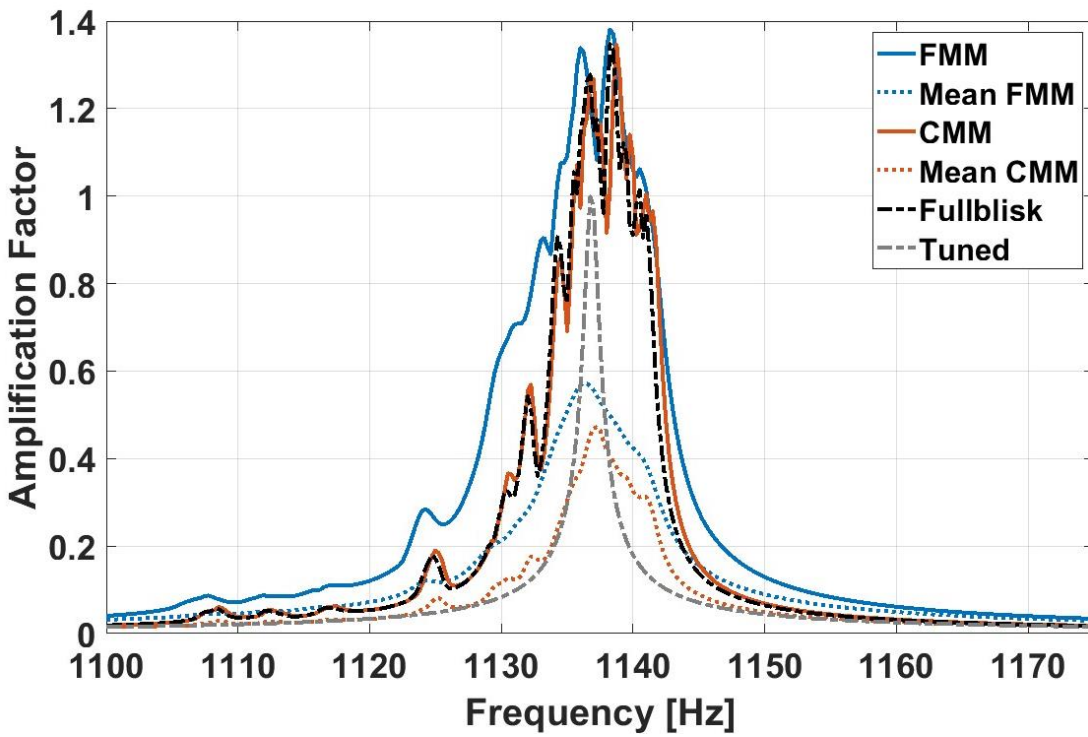


(b)

Figure 3.19 (a) Forced Response and (b) Amplification factor of Rotor 2 with 0.5% standard deviation mistuning (Full blisk - First Bending Mode).



(a)



(b)

Figure 3.20 (a) Blade Amplification Factor and (b) Maximum response envelope (First Bending Mode)

Figure 3.20 depicts the forced response results for the first bending mode. Note that the differences in the plots look severe due to the scale of the plots. FMM captured the overall shape and peak amplitude within 2 percent, while CMM captured it within 0.05 percent. The peak amplification factor was estimated well by both of the reduced order models. The modal participation factors in Figure 3.21 show no significant participation from other families of modes, indicating that the bending mode can be estimated accurately for blade dominant nodal diameters using the FMM method.

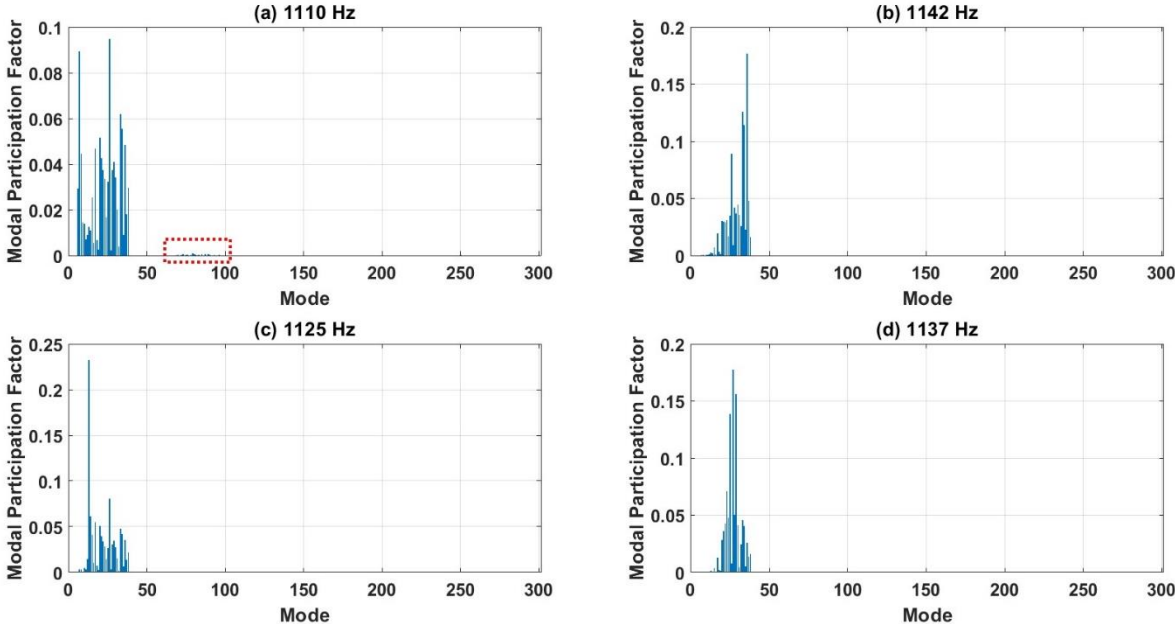
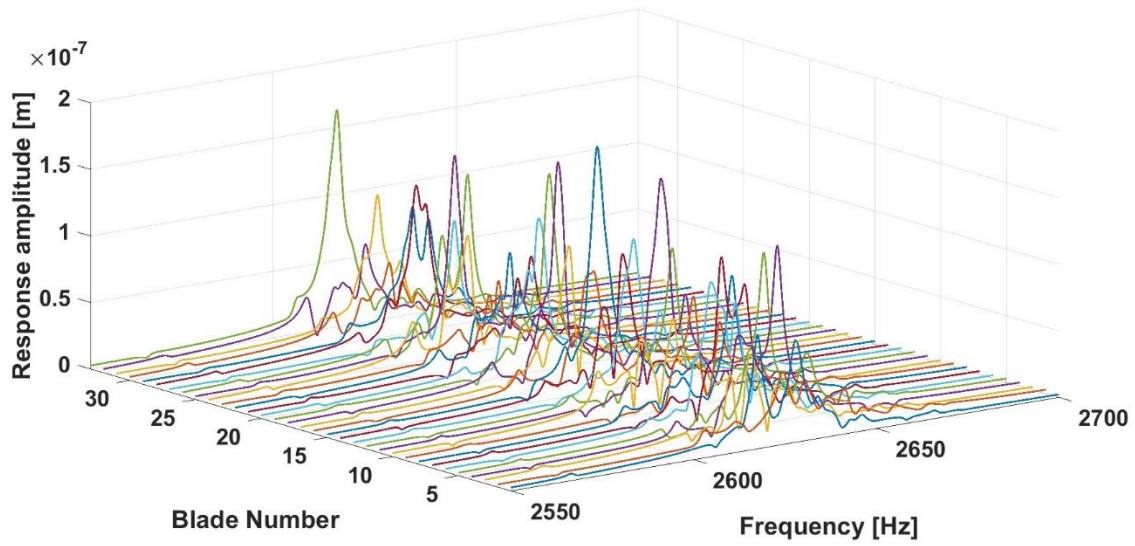
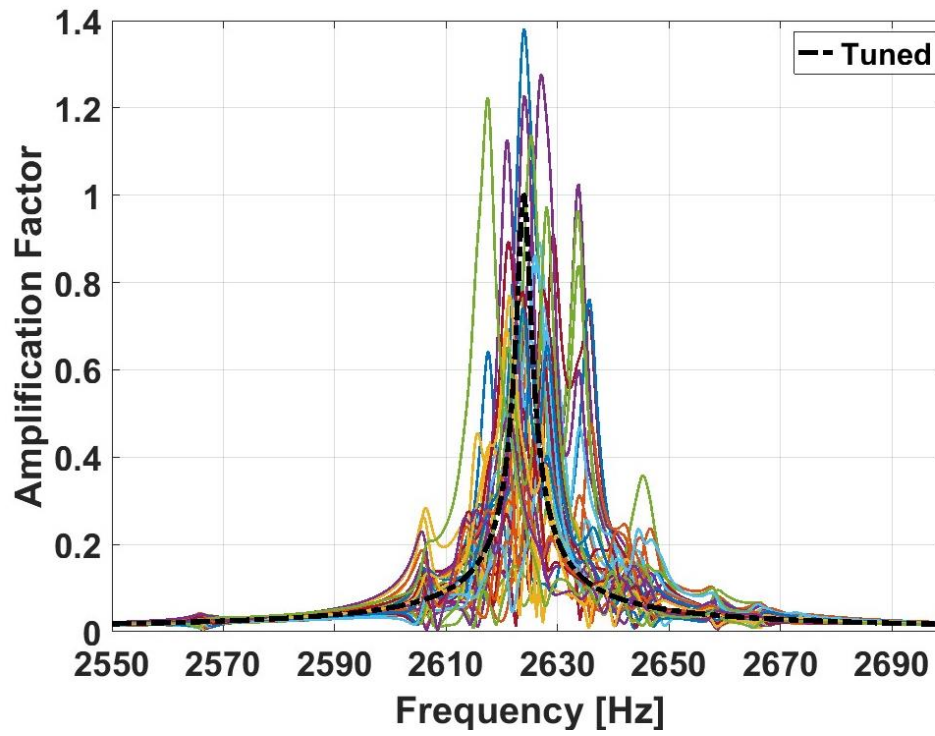


Figure 3.21 Modal participation factors (First Bending Mode (ND 11) – 0.5% standard deviation)

The first torsion mode’s response, amplification, and modal participation factors are illustrated in Figure 3.22 and Figure 3.23.



(a)



(b)

Figure 3.22 (a) Forced Response and (b) Amplification factor with 0.5% SD mistuning (Full blisk - First Torsion Mode).

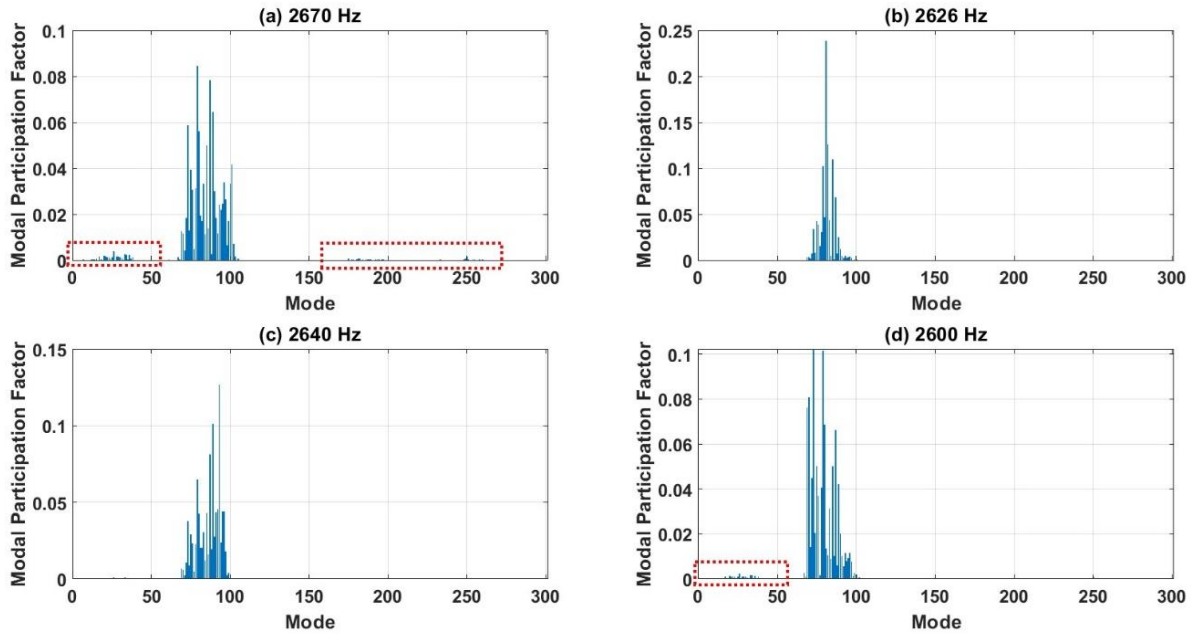


Figure 3.23 Modal participation factors (ND 11 – 0.5% standard deviation)

As highlighted, participation from other families of modes is observed in this case. Although small compared to dominant modes, this participation can affect the response. In such cases, selecting modes for the FMM method is crucial, especially for lower modes with significant disk participation. Unlike the bending mode, which has majorly blade-dominated modes, the torsion mode contains fifty percent modes with disk participation which might require additional considerations for the FMM model. As described in Figure 3.24, two selection approaches are used to assess the FMM model. In the first approach, modes are selected, as highlighted in red. In the following case, the family of modes close to the blade frequency is selected, as highlighted in blue.

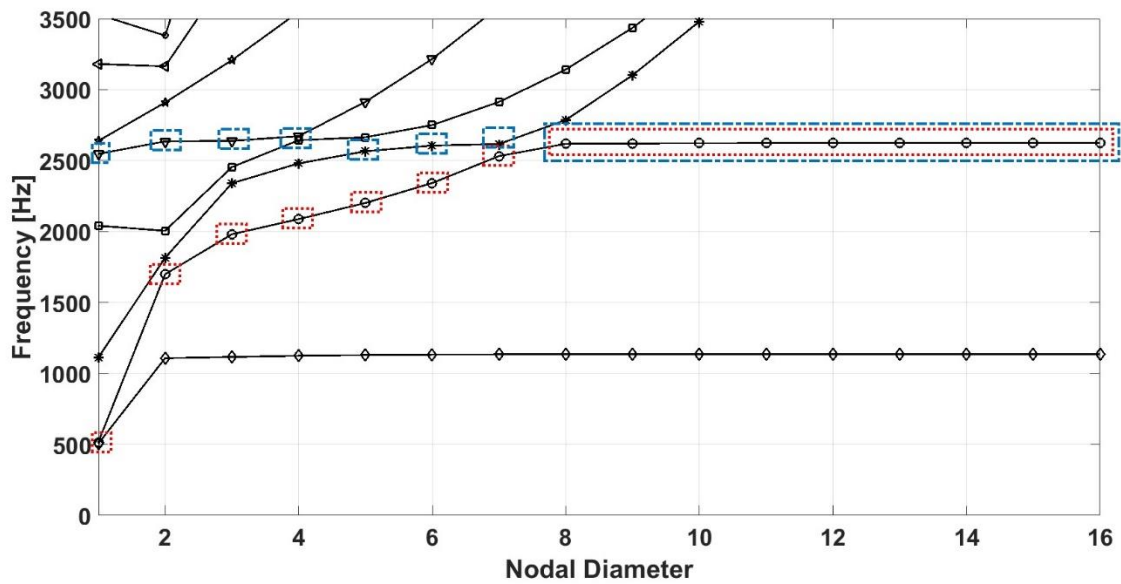


Figure 3.24 Tuned system mode selection approaches for Torsion Mode

The mistuned frequencies predicted by the reduced-order models are shown in Figure 3.25. FMM and CMM give accurate estimations of the mistuned frequencies for this case, with the maximum error in the frequency prediction within 0.5 percent. Note that the modal participation factors and mistuned frequencies are not plotted for the subsequent cases. The comparison between models is made with the response envelope and amplification factors. A comparison of changes in the frequency band is made in the later chapter for each case to assess the mistuning effects on the resonant frequencies.

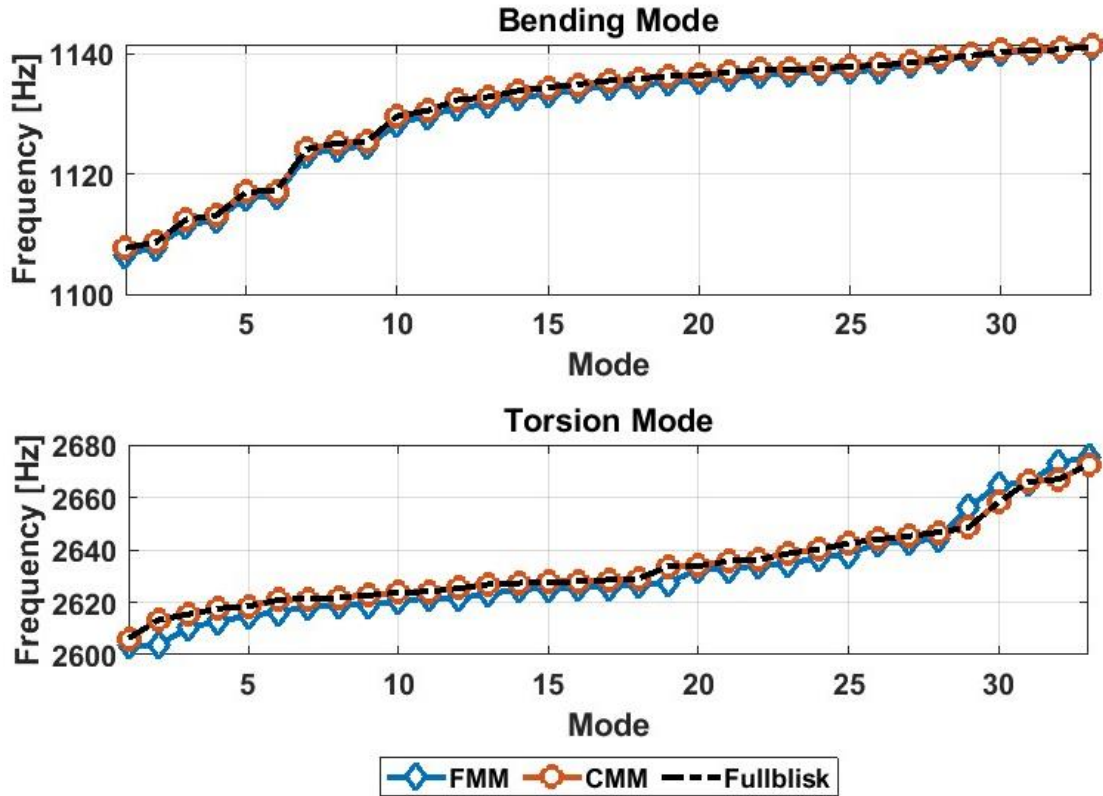


Figure 3.25 Mistuned frequency (0.5% SD).

The amplification factor and forced response envelope for the first and second approaches are shown in Figure 3.26 and Figure 3.27. The first approach, which considers an isolated family of modes, predicts the peak amplification factor within 0.5 percent but does not capture the response shape well. The second approach overestimates the peak amplitude by 6.4 percent but better captures the response shape and individual blade amplification factors. These differences indicate modal participation of several modes for this mistuning case. The good estimation of peak amplitude using the FMM method also suggests that the isolated family modes are the dominant modes in the response. A detailed comparison of individual blade responses is done for this case and plotted in Figure 3.28 and Figure 3.29. Small participation of other modes can change the response envelope and peak amplification factor.

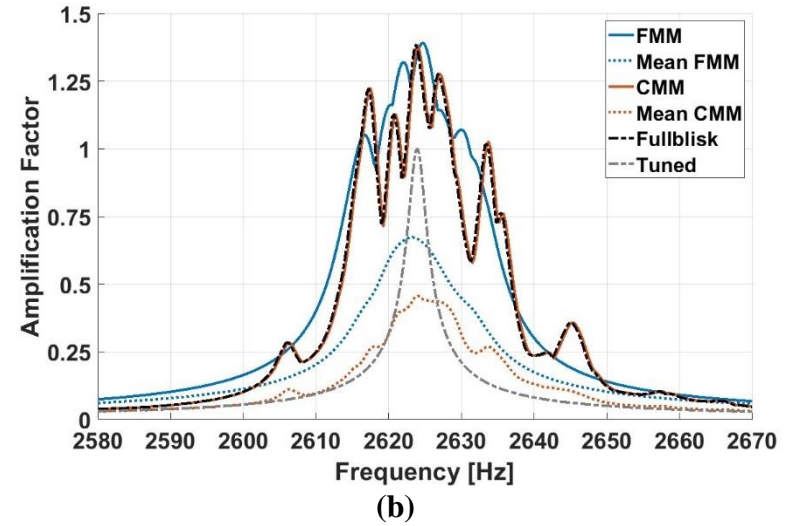
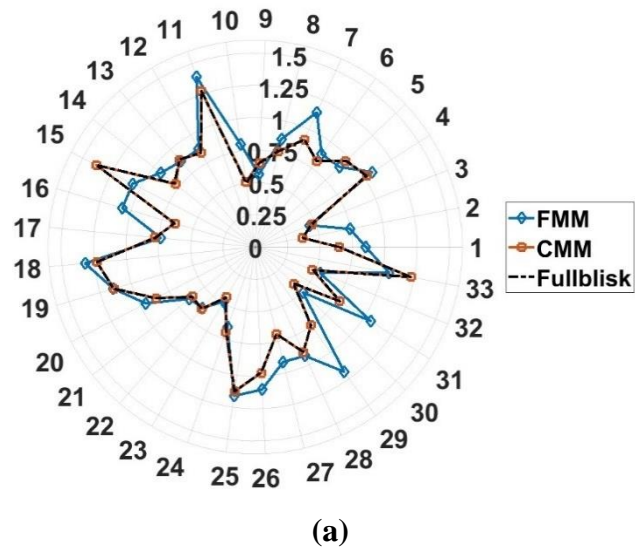


Figure 3.26 (a) Blade Amplification Factor and (b) Maximum response envelope (ND 11 - First approach)

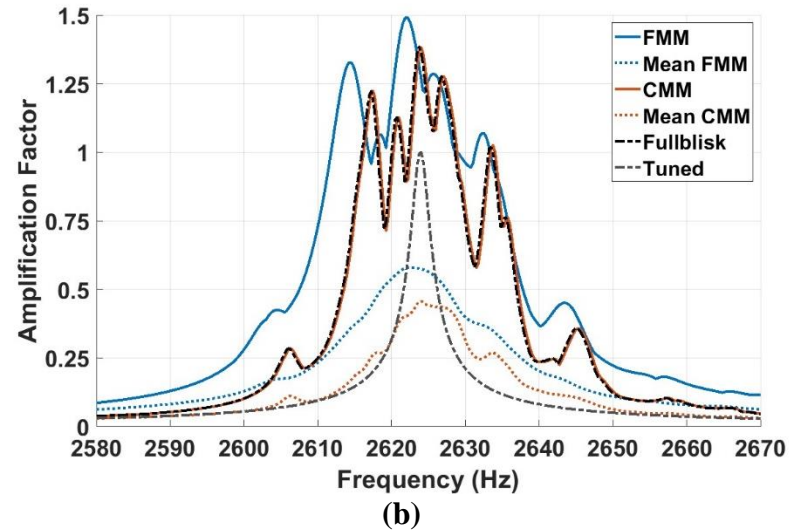
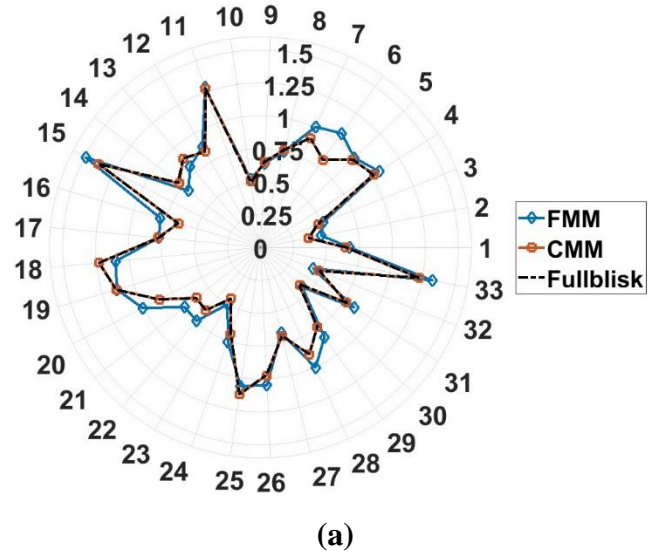


Figure 3.27 (a) Blade Amplification Factor and (b) Maximum response envelope (ND 11 - Second approach)

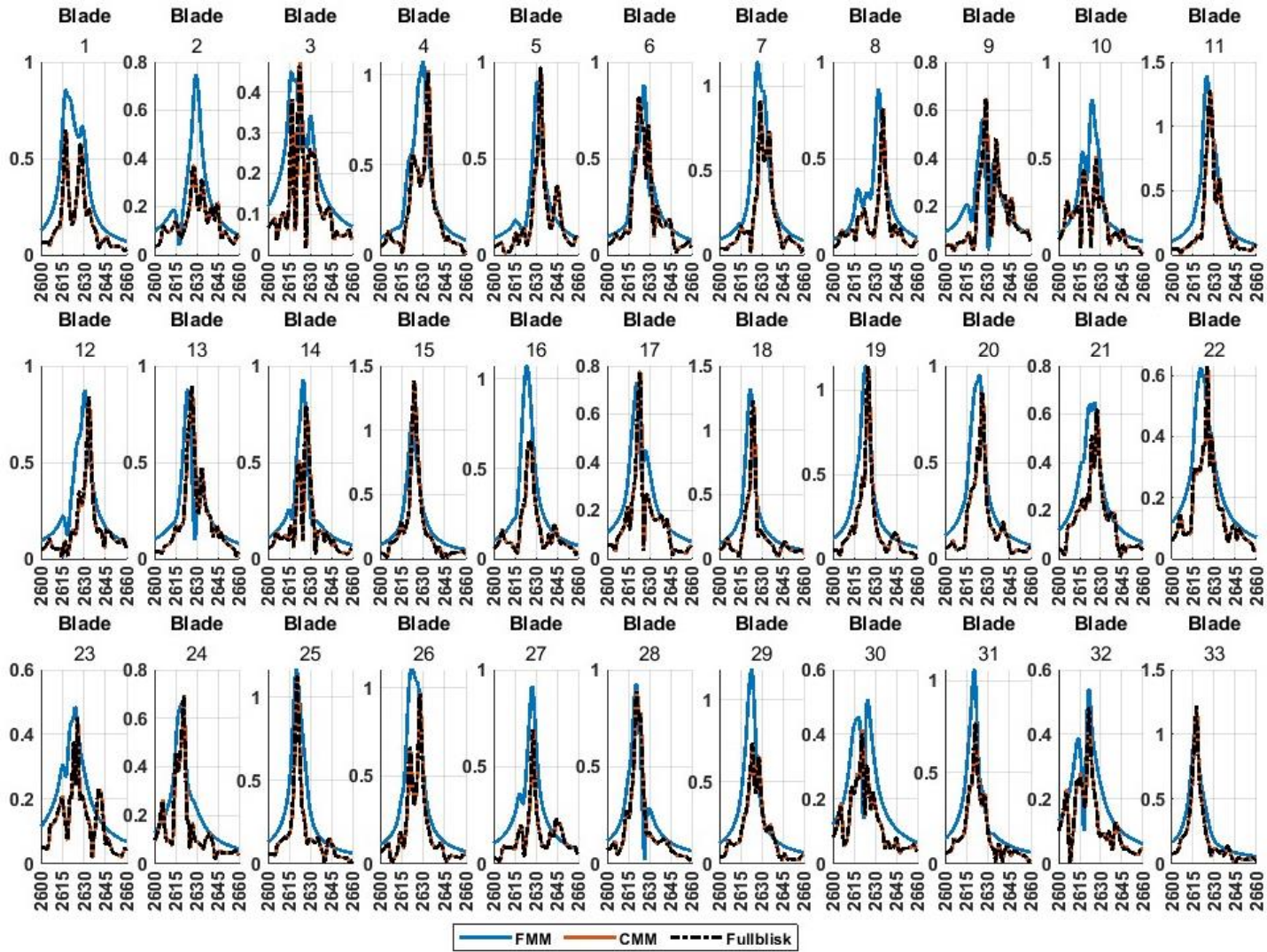


Figure 3.28 Blade Amplification Factor (First Approach)

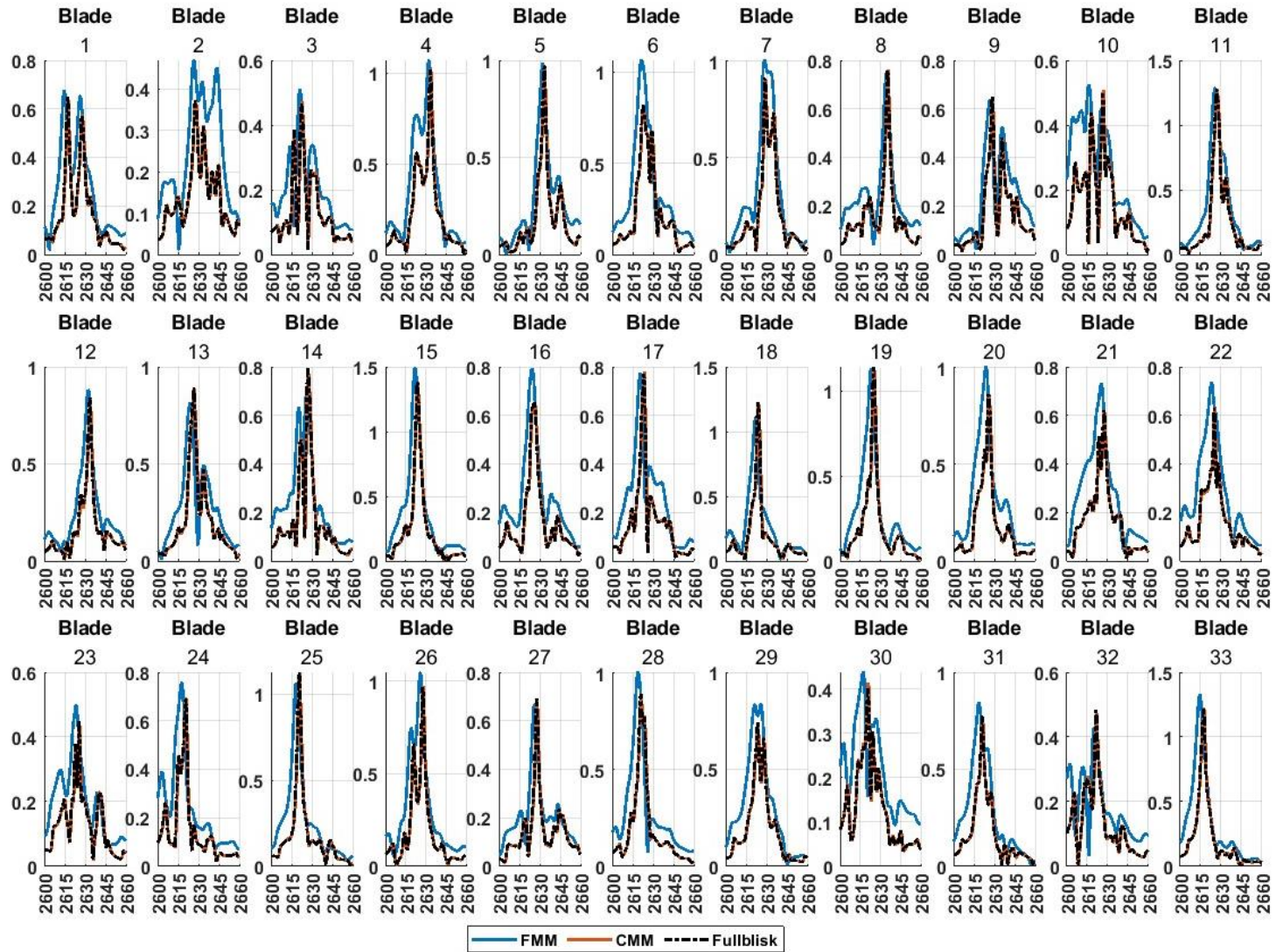


Figure 3.29 Blade Amplification Factor (Second Approach)

Figure 3.30 briefly compares the amplification factors for ND 3, ND 5, and ND 11 crossings of the first bending mode. The effect of the excitation order on the dynamic behavior of the mistuned system shows that mode localization is not only a function of the mistuning pattern.

Figure 3.31 compares the reduced-order models for these nodal diameters. FMM estimates the amplification factor well for the blade-dominant bending family. A slightly higher percent error is observed for the lower nodal diameter. This trend indicates that the FMM formulation is well suited for the higher frequency modes of the blade dominant mode family. The low-responding blades in ND 5 excitation case were the highest-responding blades in ND 11 case. The highest responding blades, 14, 32, and 11, for ND 3, ND 5, and ND 11 cases have an interesting trend of low deviation being sandwiched between high deviations. These types of deviation patterns have been predicted to be the worst case of mistuning in past research. The nodal diameters which are majorly excited in the system can be targeted to intentionally mistune the system by studying their behavior at these nodal diameters.

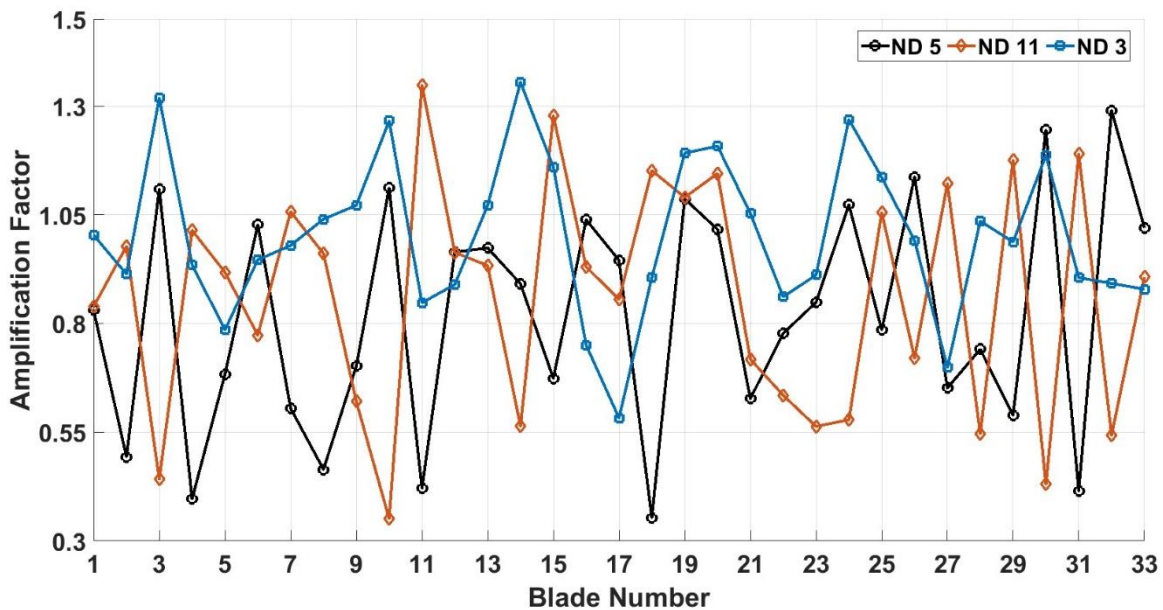


Figure 3.30 Comparison of Fullblisk amplification factor at ND 3, ND 5, and ND 11 crossings (0.5% Deviation)

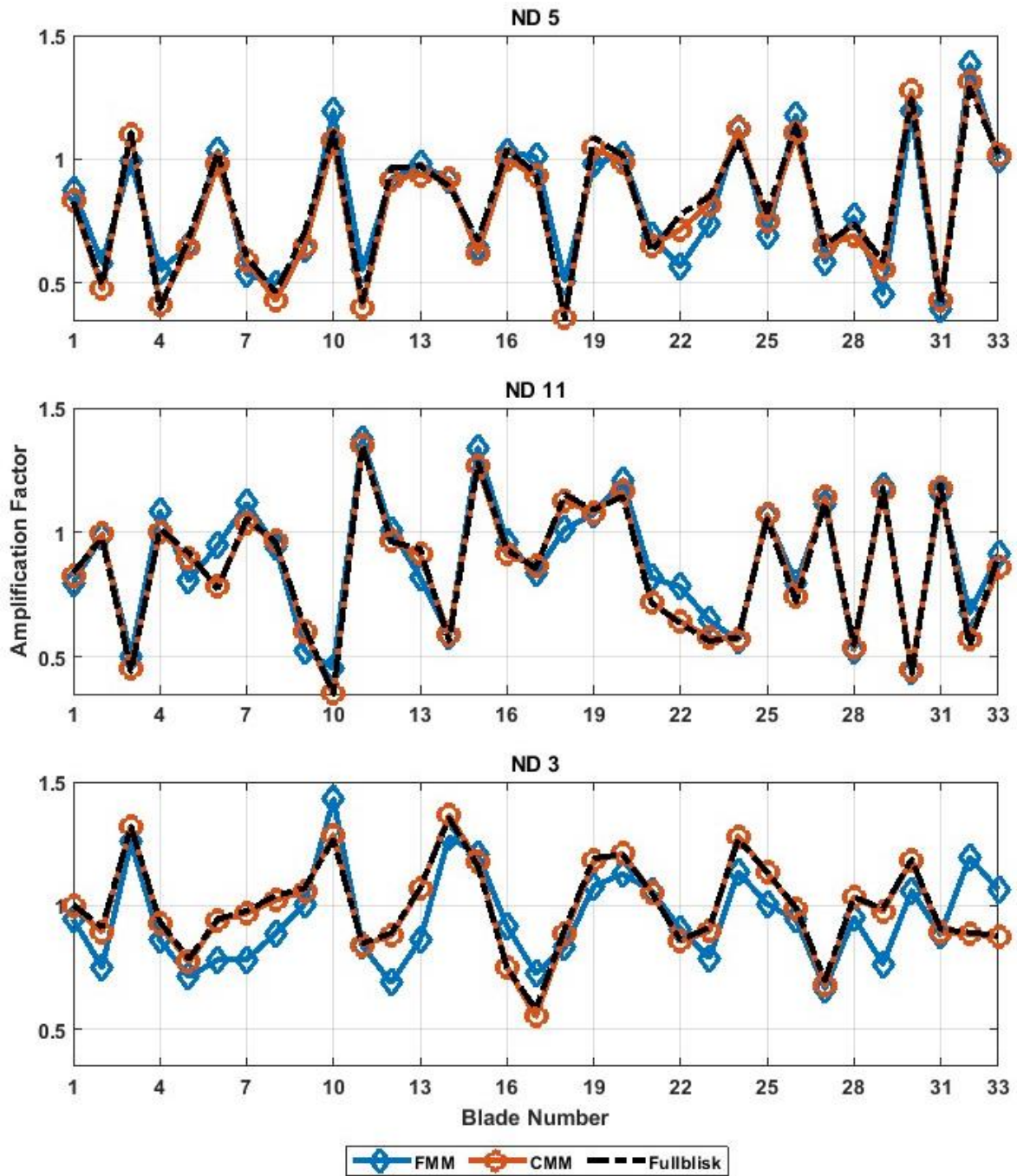


Figure 3.31 Amplification factors for ND 3, ND 5, and ND 11 crossings of 1st Bending mode (0.5% Deviation)

Veering Region ND 3 and ND 5

The veering region corresponding to ND 3 has three resonant frequencies ranging from 2000 to 3000 Hz. The energy exchange and several modal participation possibilities are significantly higher in the veering regions. The tuned response results showed that this range's first two resonant crossings are disk dominant, which are not significantly impacted by mistuning. In most cases, the response at these frequencies is similar to a tuned system, corresponding to tuned system frequencies of 2340.5 and 2454.7 Hz, as illustrated in Figure 3.32 (a). Therefore, the blade-dominated tuned system frequency of 2639.4 Hz is used as input to the FMM method. Since this mode lies in the region with disk participation selecting the isolated mode family corresponding to the resonant frequency does not give a comparable result, as the isolated mode family frequencies range between 2000 Hz and 5900 Hz. The amplification factors and response envelope computed using the approach of selecting the modes nearest to the mistuned frequencies are shown in Figure 3.33. Note that only the blade-dominated frequency range is shown to discern the effects of mistuning, and the differences between CMM and full blisk results are not evident due to the scale of the plot.

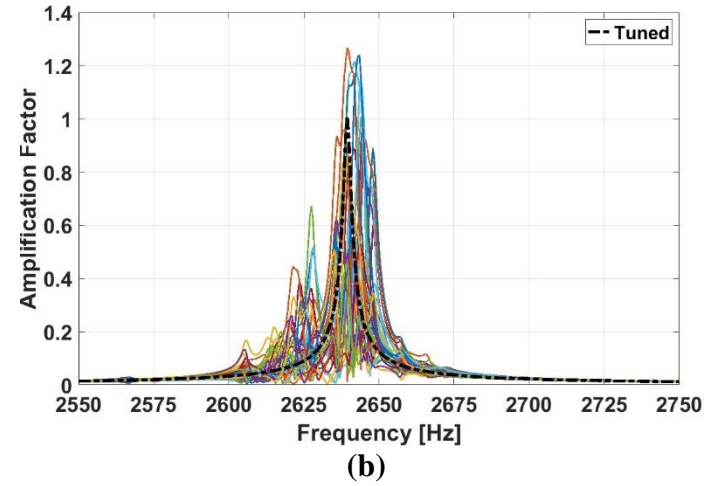
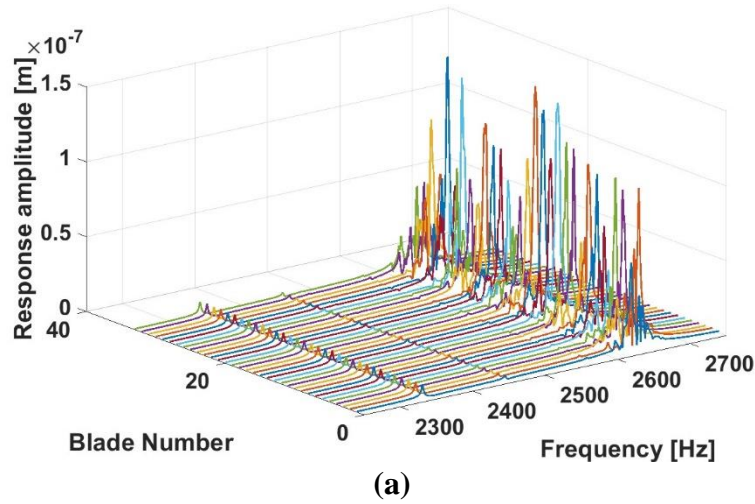


Figure 3.32 (a) Forced Response and (b) Amplification factor 0.5% SD mistuning (Full blisk – ND 3).

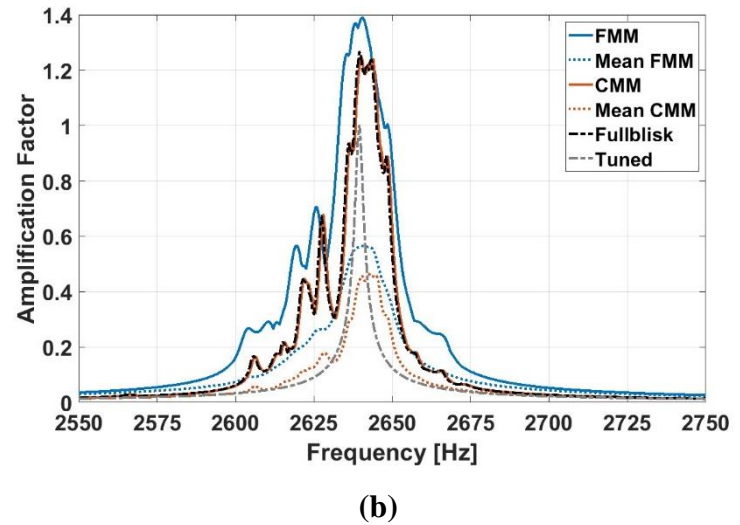
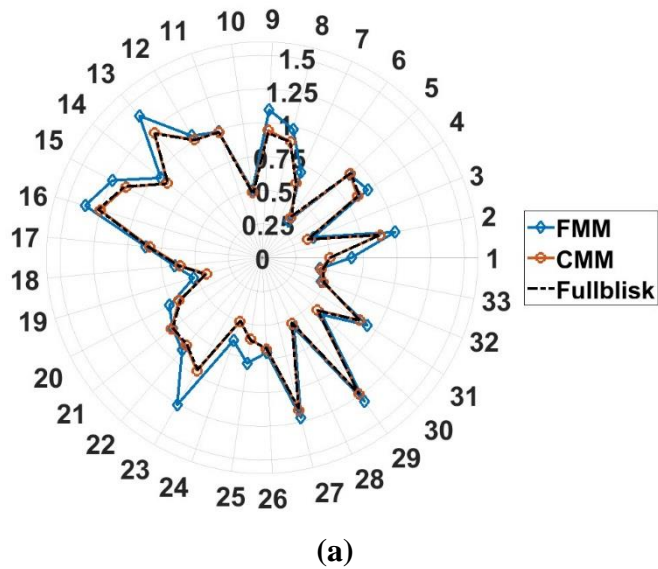


Figure 3.33 (a) Blade Amplification Factor and (b) Maximum response envelope (ND 3)

An error of 1.13 percent is observed for the CMM method, while a more significant error of 9.7 percent occurs in the peak response with the FMM method. The response envelope shape and trends are captured well by both CMM and FMM methods. The good estimation of the response envelope by FMM indicates that the included mode family dominates the response. In cases where the energy exchange between modes is minimal, FMM can be used to predict the response. The tuned system response can identify the disk-dominated and blade-dominated frequencies.

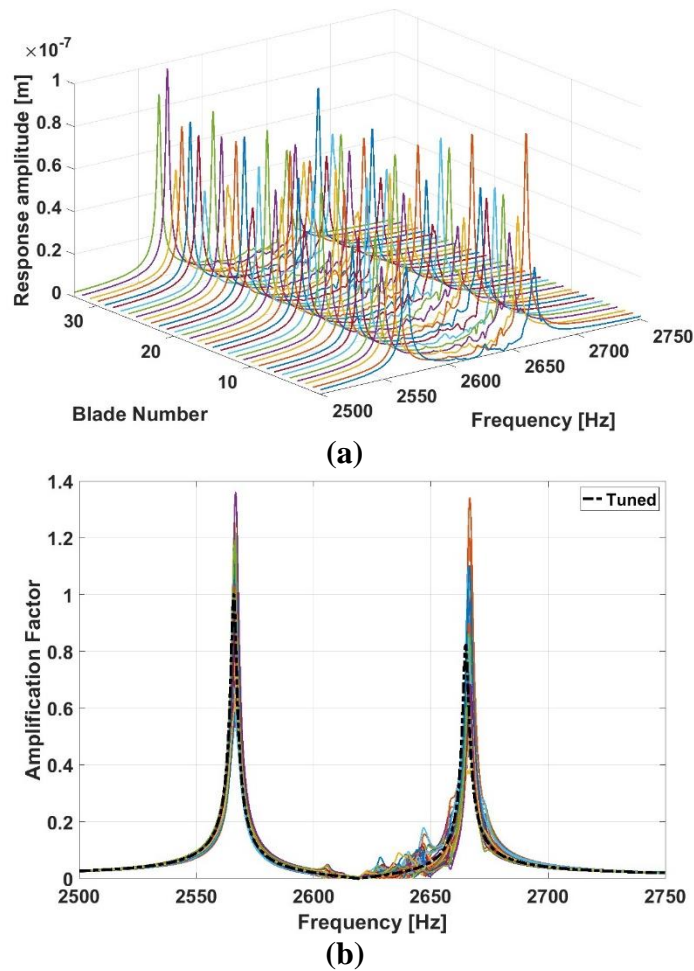


Figure 3.34 (a) Forced Response and (b) Amplification factor 0.5% SD mistuning (Full blisk – ND 5).

Figure 3.34 depicts the response and amplification factors corresponding to ND 5. Although the dominant frequencies are closely spaced, it is interesting that no significant observed frequency band increase exists. The frequency band at this nodal diameter shows minimal

interaction between modes, as shown in Figure 3.35. The two blade-dominant frequencies can be separated into individual sweeps, or a single sweep can be used in the current case for FMM formulation. Frequency sweeps from 2500 to 2650 Hz and 2600 to 3000 Hz, along with a single sweep, are used to study both peaks. Separating the sweep ranges gave a better estimation of the blade peak amplification than in a single sweep. This behavior shows that FMM is extremely sensitive to frequency selection as the interactions between modes increase, making this method unreliable in veering regions. The estimations could be entirely incorrect if one majorly participating frequency is not included in the input dataset. Note that the response is normalized by the tuned response of the first peak to compute the amplification factors for both responses.

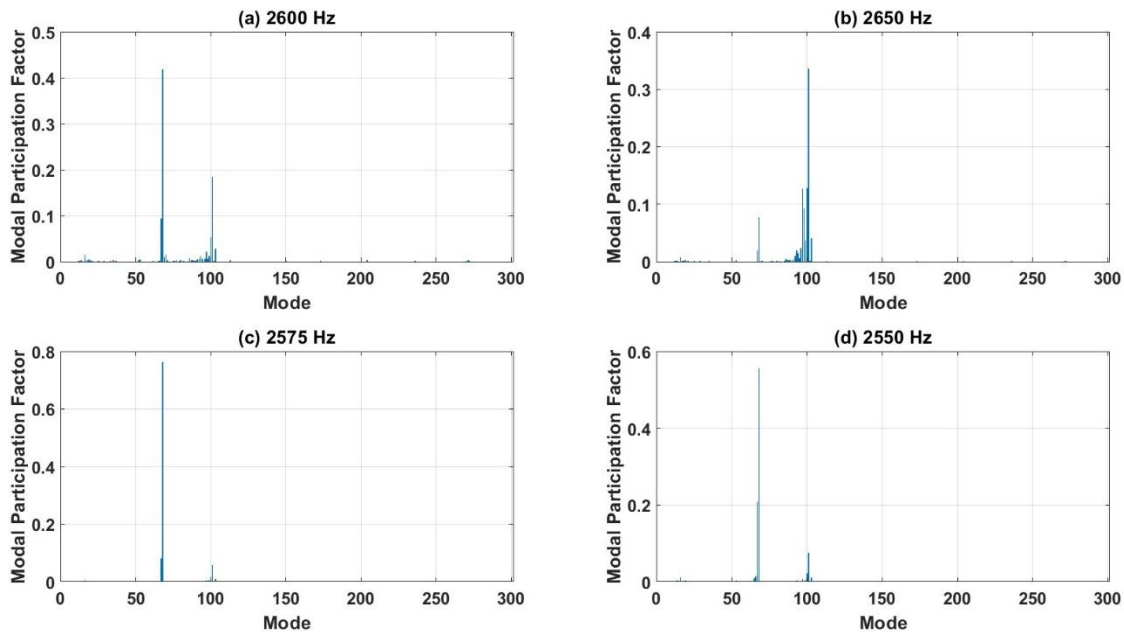


Figure 3.35 Modal participation factors (ND 5 – 0.5% standard deviation)

CMM and FMM formulations estimate the forced response envelope well, with a slightly higher error with the FMM formulation. In cases where only one blade family dominated the selected frequency band, FMM and CMM models predict the response well. CMM estimates the responses for both sweeps within 1.5 percent. A 9.9 and 17.94 percent error is observed for the respective sweeps with the FMM formulation, as illustrated in Figure 3.36 and Figure 3.37.

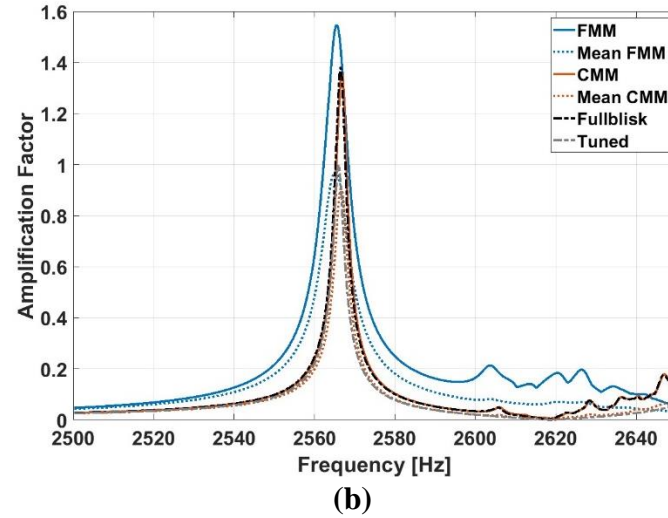
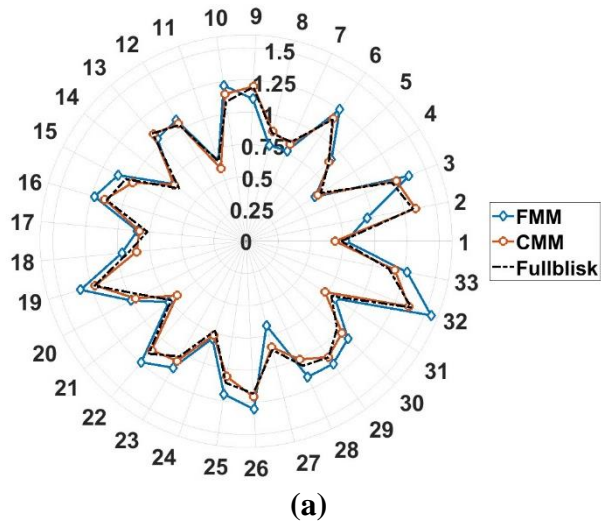


Figure 3.36 (a) Blade Amplification Factor and (b) Maximum response envelope (Sweep: 2500-2650 Hz: ND 5).

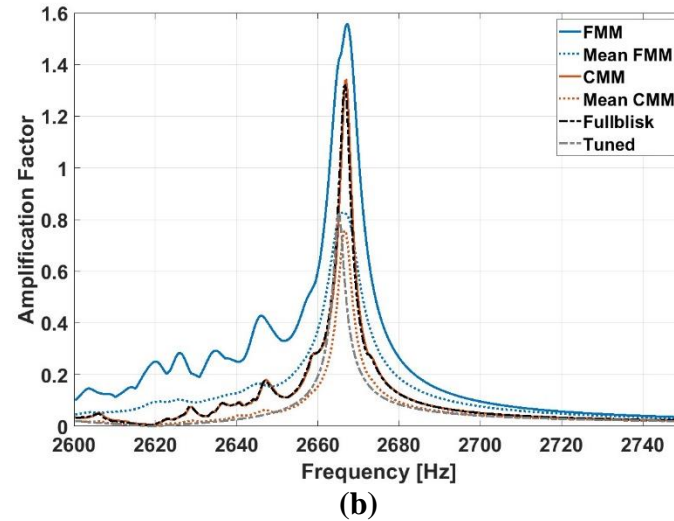
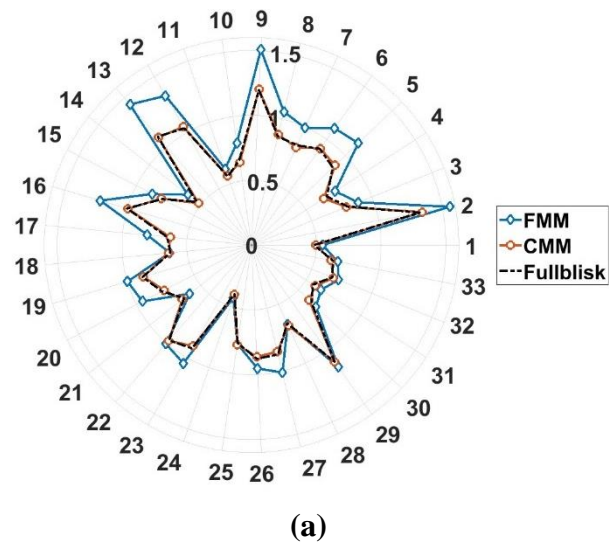


Figure 3.37 (a) Blade Amplification Factor and (b) Maximum response envelope (Sweep: 2600-3000 Hz: ND 5).

3.2.3 Frequency Mistuning

In this case, blade frequencies from the ping test are used to mistune the FE models using equations (2.2) and (2.3). The deviations are computed using the ping test results, leading to different deviations for each mode family. Each frequency can be mistuned independently in the CMM formulation in such cases. In contrast, for the full blisk, each mode sweep range must be individually set up with changed Young's modulus to mistune the system independently. In this case, the average deviation of the first three modes, which is about 1.5 percent with 0.45 percent SD, is taken to simplify the case. These models will be studied with independently mistuned frequencies, including aerodynamic coupling, to validate them in the future.

Figure 3.38 shows the blade amplification factors for the first bending family at ND 5, ND 11, and ND 3. The blade amplification factors are estimated well by CMM, while FMM fails to give a reasonable estimate, especially for ND 5 and ND 3 cases. The modal participation factors show minor participation from the first torsion mode family, which is unaccounted for in the FMM formulation. The assumption of the isolated mode family has resulted in an incorrect estimation of the amplification, especially for ND 3 and ND 5 cases. The peak amplification factor for ND 11 case was estimated within 0.5 percent by both formulations. Similar results are plotted for the first torsion mode and veering regions in

An error of 17 percent exists for the torsion mode, while much higher errors occur for the other cases, making FMM unsuitable for predicting forced response for cases with high modal interactions.

FMM estimated the amplification factors reasonably well for the previous 0.5 percent SD case with 0.0014 average deviation, which shows that the participation is notably affected by the mistuning pattern, average deviation, and not just the standard deviation. The FMM model gives a good prediction when the mistuned cantilever blade modes are close to the tuned system modes. The reduced order models can be combined with Monte Carlo analysis to explore the worst case of probable mistuning patterns to predict the fatigue life for the worst case. Previous research showed that when multiple blade-dominated modes are closely spaced, using frequency mistuning

to include all the blade-dominant eigenvalue mistuning patterns can predict the response accurately. This approach of independent mistuning would be used to validate these models with the experimental data.

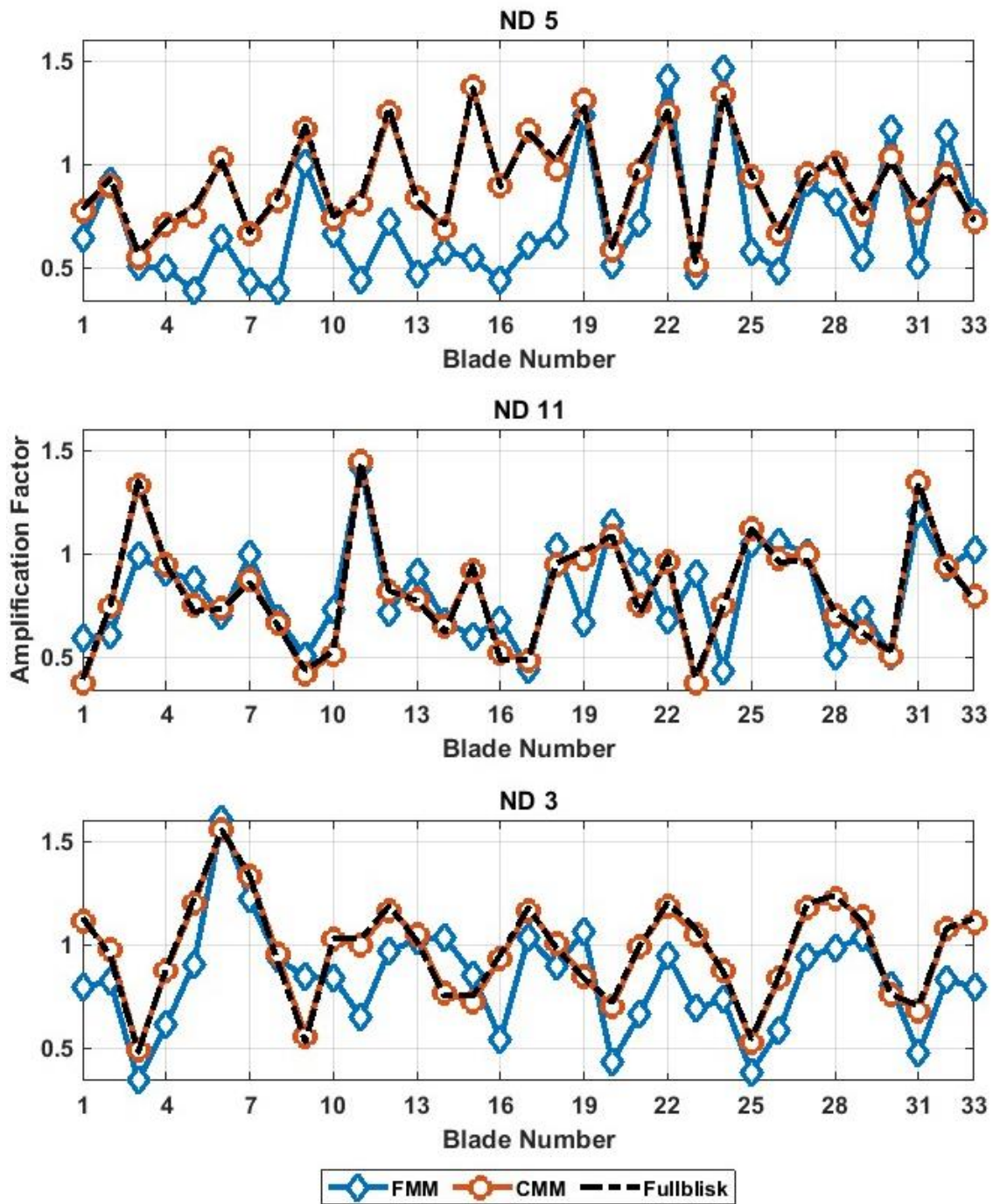


Figure 3.38 Amplification factors for ND 3, ND 5, and ND 11 crossings of 1st Bending mode (Ping test Frequencies (0.45% SD)).

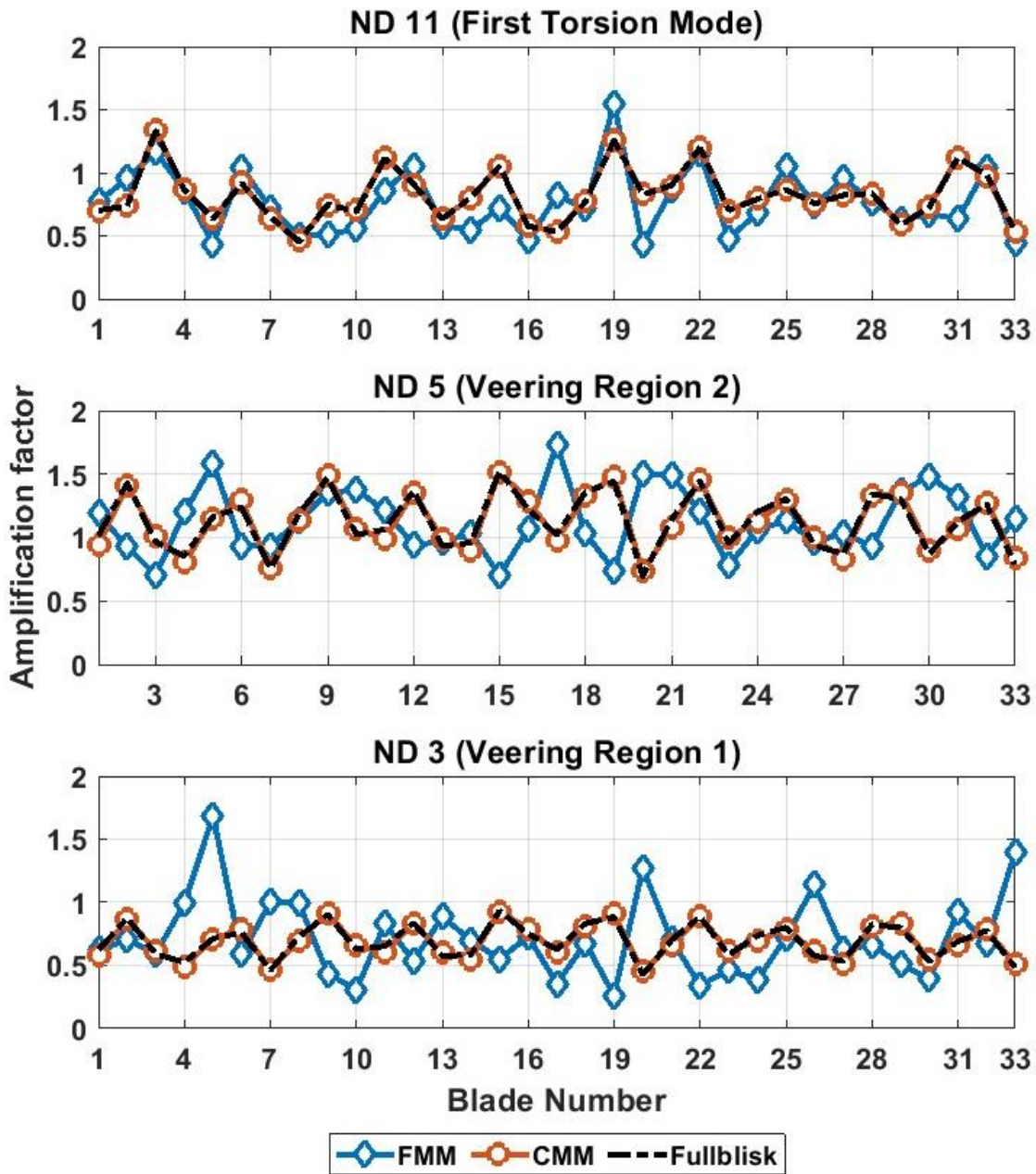


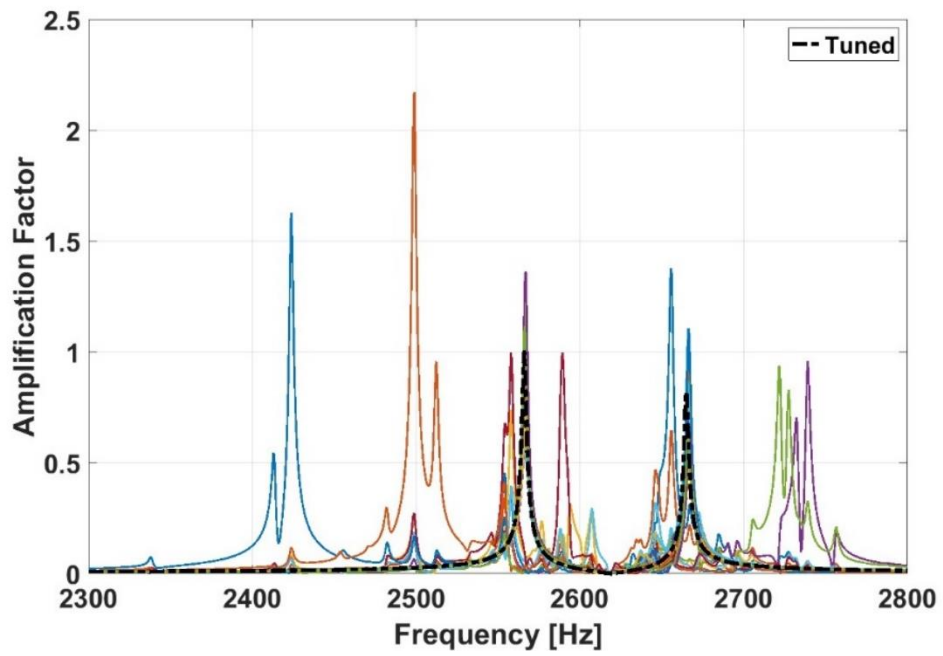
Figure 3.39 Amplification factors for ND 3, ND 5, and ND 11 crossings between 2000 to 3000 Hz (Ping test Frequencies (0.45% SD))

4. LARGE MISTUNING CASES

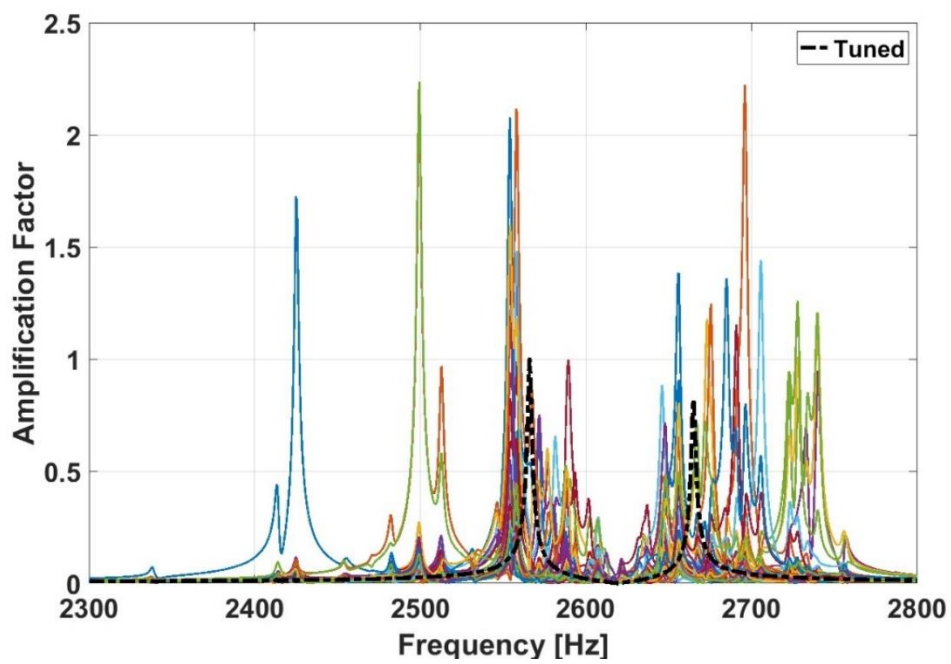
This investigation classifies standard deviations above two percent as large mistuning cases. High deviations may occur with uneven wear or damage. Minimal modal interaction from different families occurred in the previous cases with small mistuning. Even minimal interaction changed the response significantly. The cases with large deviations can have extensive modal interactions, which will affect the response substantially. This chapter investigates these cases to determine if CMM can capture such complex behavior.

Figure 4.1 (a) and (b) compare the forced response with 300 and 400 modes, respectively. Although the modal participation is small from the higher modes, a notable difference in the response is observed. The peaks at 2700 and 2550 Hz are not predicted with 300 modes. Modes 300 to 400 lie in the frequency range of 6500 Hz to 8400 Hz, and it is noteworthy how these modes affect the response for a mistuned system. The models cannot accurately capture the system's response if insufficient tuned system modes are included. The solution converges rapidly as the number of retained tuned system modes increases. As in previous cases, the dominant cantilever blade modes are required to estimate the amplification factor reasonably. Retaining at least 400 to 500 modes is recommended for large mistuning cases considering the effects of modal participation and CBM study.

In the veering or high modal density regions, where other modes strongly contribute to the response of the blade, the FMM method is incapable of accurately predicting the response due to its assumptions, as illustrated in Figure 4.2 and Figure 4.3 FMM gave a reasonable estimate of the maximum amplification of the sweep for the ND 11 case but could not capture the complex details of the response for the cases, as illustrated in Figure 4.2. The amplification factor is maximum for the veering region 2 (ND 5), where two blade-dominant modes interact.

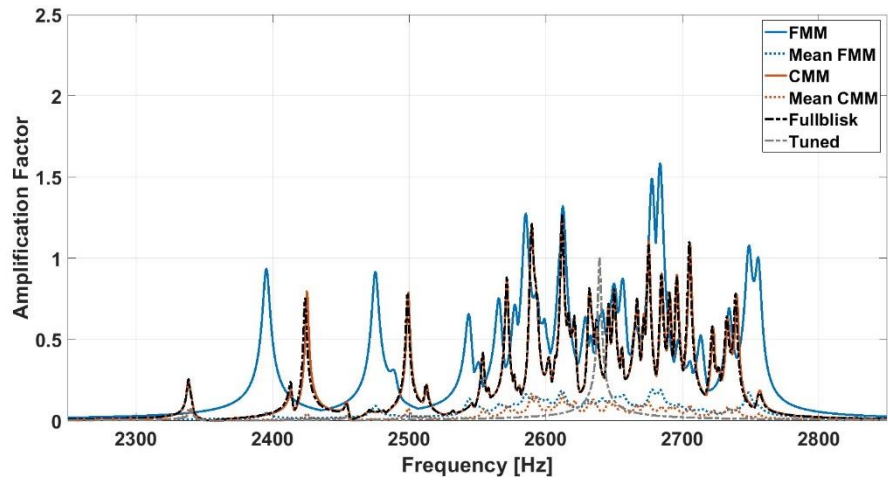


(a)

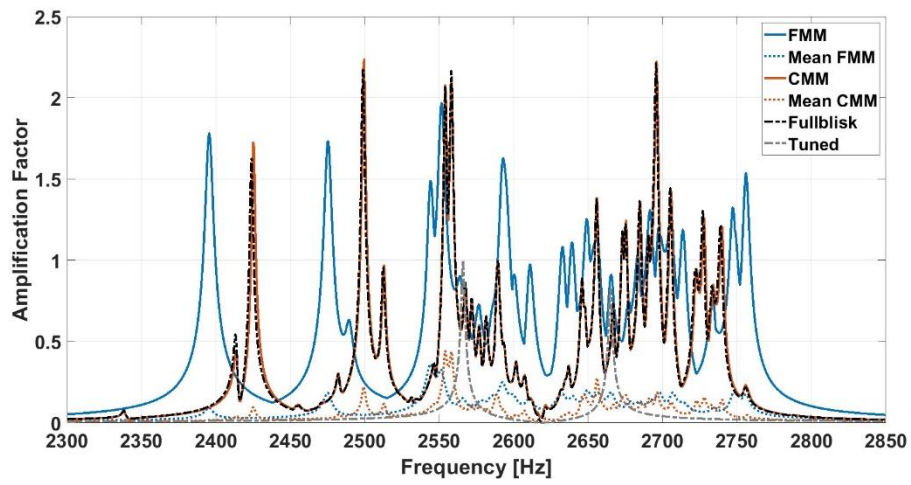


(b)

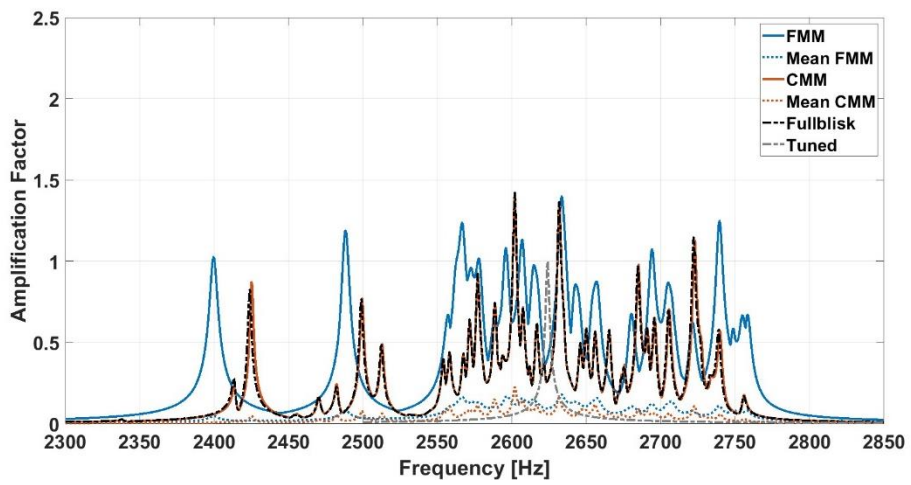
Figure 4.1 (a) Forced Response at ND 5 (Fullblisk - 300 Modes) (b) Forced Response at ND 5 (Fullblisk - 400 Modes)



(a)



(b)



(c)

Figure 4.2 (a) Maximum response envelope (ND 3) (b) Maximum response envelope (ND 5)
(c) Maximum response envelope (ND 11) [Frequency Sweep 2000-3000 Hz].

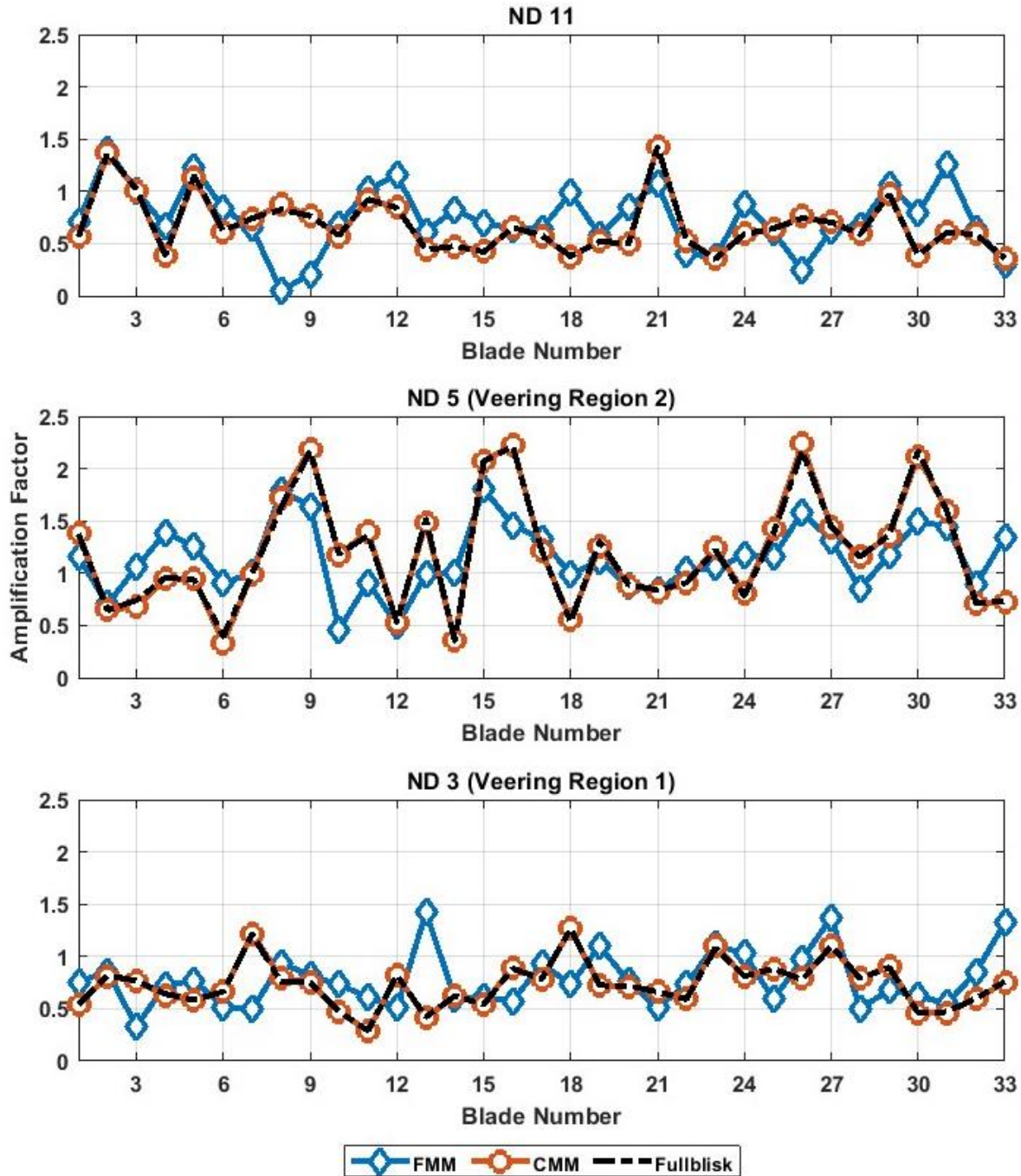


Figure 4.3 Amplification factors for ND 3, ND 5, and ND 11 crossings between 2000 to 3000 Hz (5% SD).

The blade amplification factors for sweeps in the 2000 to 3000 Hz are shown in Figure 4.3. In this case, FMM does not predict the blade responses well, while CMM predicted the responses within a 1 percent error. The FMM model could not accurately predict responses for the bending

mode, as shown in Figure 4.4. FMM models the response moderately well for the high nodal diameter cases. This behavior indicates that our current FMM formulation cannot predict responses well for cases with high modal interactions and where mistuned blade modes are far from the tuned modes.

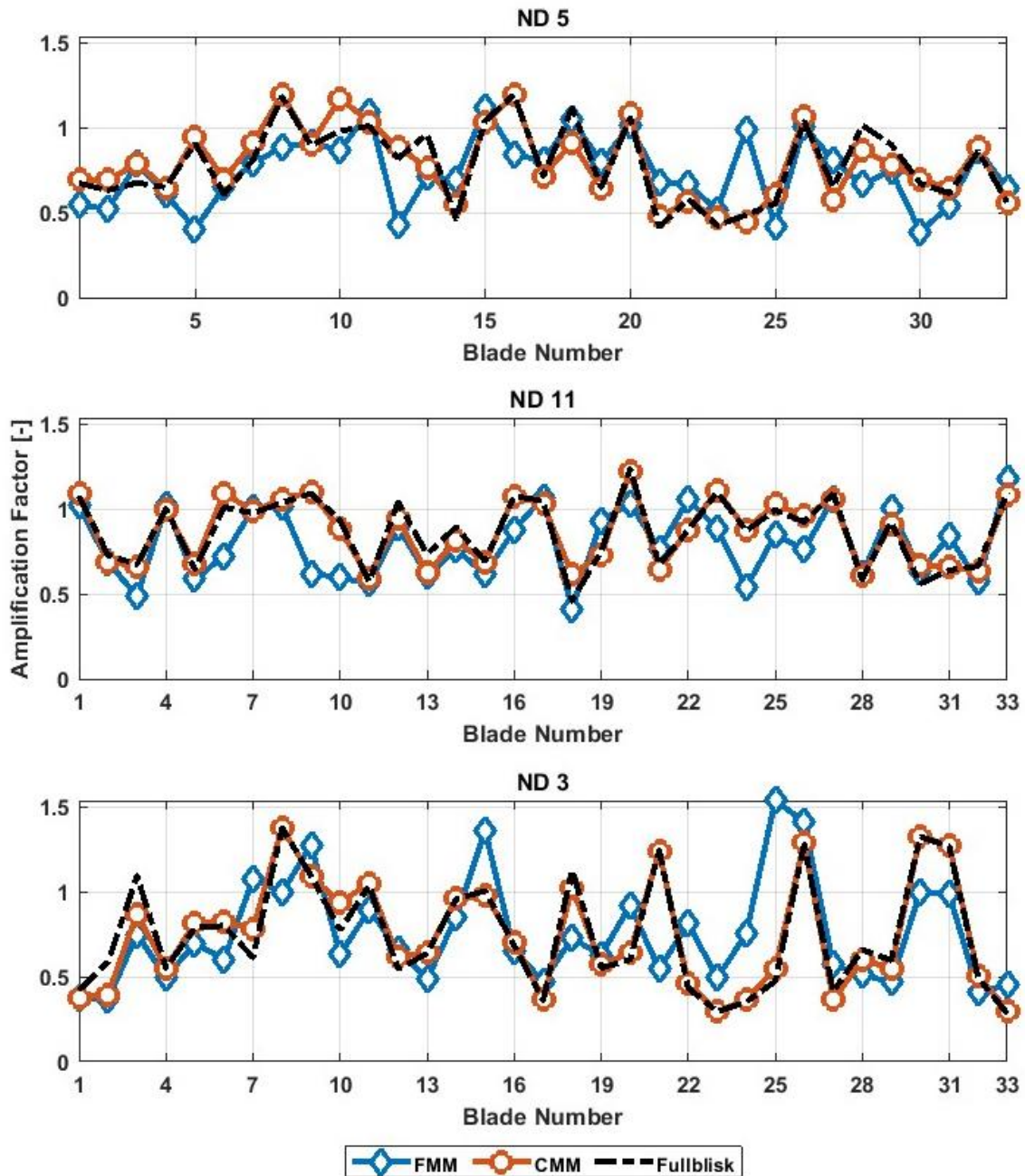
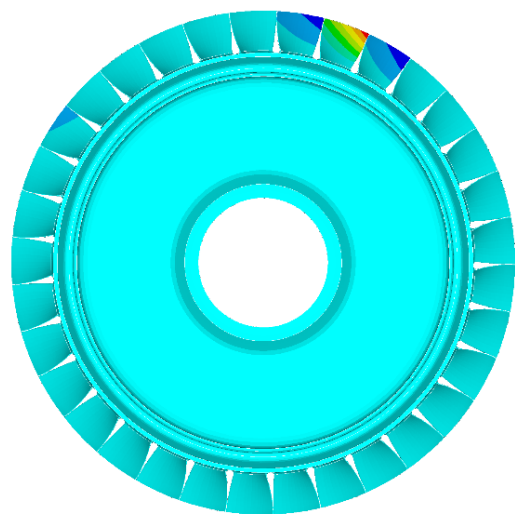
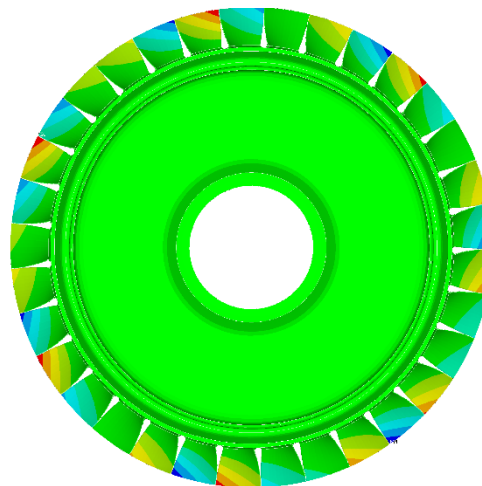


Figure 4.4 Amplification factors of first bending mode for ND 3, ND 5, and ND 11 (5% SD).

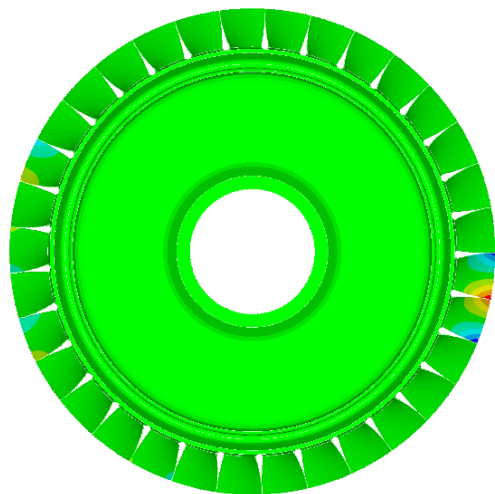


(a)

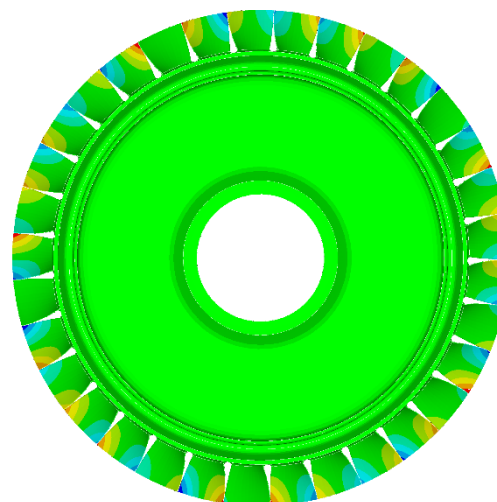


(b)

Figure 4.5 (a) Localized mode shape (Mode 31) (b) Tuned System Mode (Mode 31)



(a)



(b)

Figure 4.6 (a) Localized mode shape (Mode 72) (b) Tuned System Mode (Mode 72)

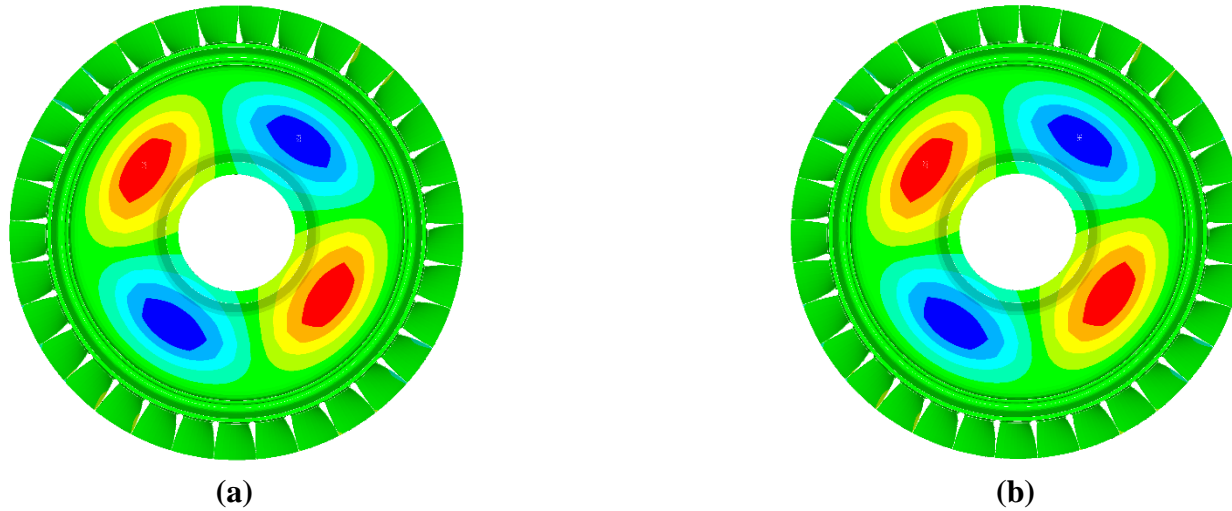


Figure 4.7 (a) Mistuned mode shape (Mode 39) (b) Tuned System Mode (Mode 39)

A comparison of the mistuned mode shape and tuned system mode shape is made in Figure 4.5, Figure 4.6, and Figure 4.7. An intense mode localization is observed for this case with a 5% standard deviation, while the mistuning barely affects a mode with significant disk participation. Note that the mode shapes are only included for the high mistuning case to show significant mode localization. Similar mode localization occurs for all cases but not to this extent. These results show the effect of mistuning on the blade-dominated bending and torsion modes.

The relative frequency differences in the mistuned frequencies with respect to tuned frequencies for each mistuned case are illustrated in Figure 4.8. Significant differences are seen in the blade modes, while minor changes are observed in the disk-dominant modes. The frequencies of the system barely changed for low mistuning cases, whose average mistuning was around 0.0001. The change in the blade frequency is directly proportional to deviation and average deviation.

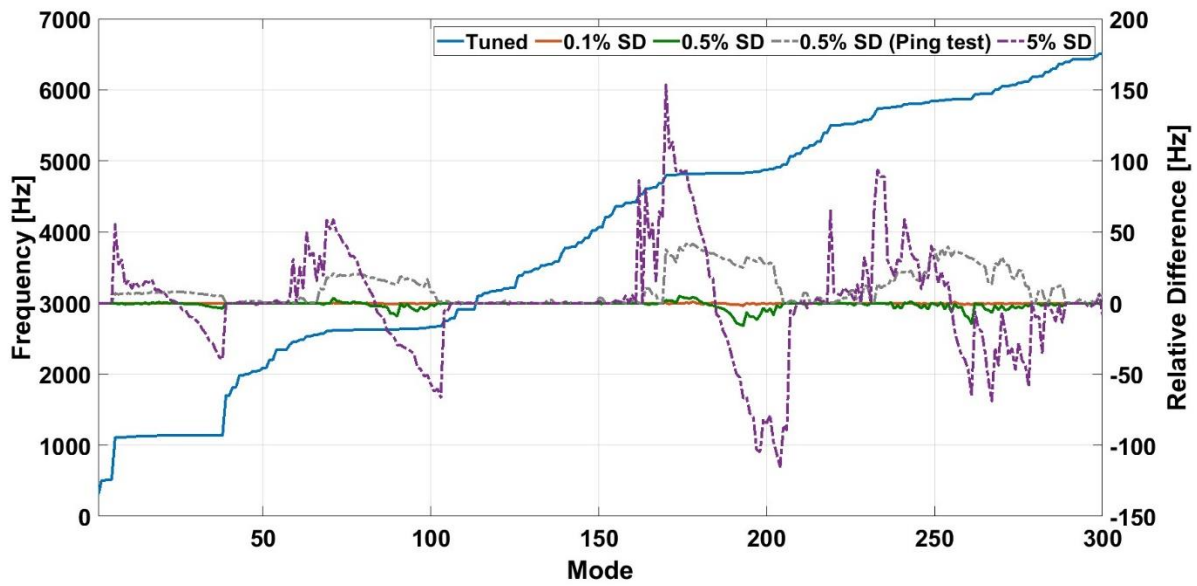


Figure 4.8 Mistuned frequencies comparison for various SD.

The deviations used in the 5% SD case are rearranged in ascending order to see the effects of the mistuning pattern. The blade amplification factors for both cases are shown in Figure 4.9. The maximum amplification factor was reduced by 13.5 percent for the second case, with a maximum amplification factor of 1.086.

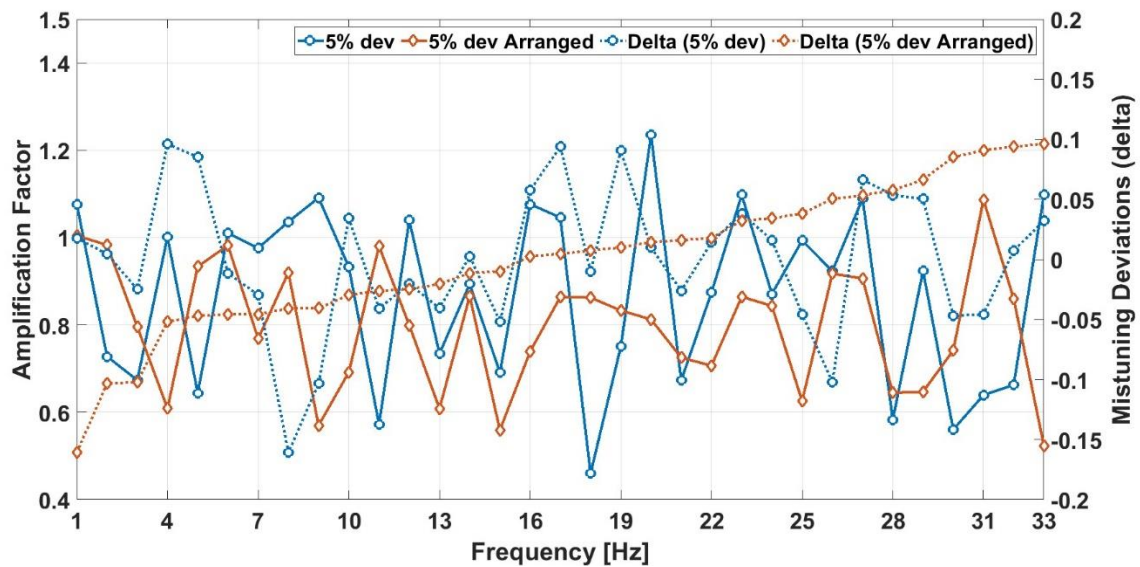


Figure 4.9 Blade amplification factor (5% SD)

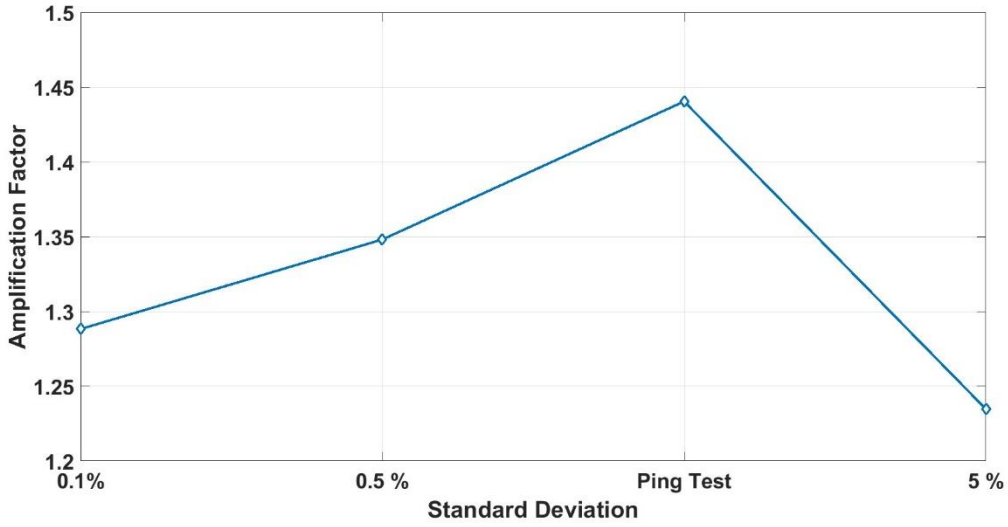


Figure 4.10 Maximum amplification factor of the mistuned system.

The maximum amplification factor corresponding to cases taken in this study is shown in Figure 4.10. The amplification factor reduces after a level of SD, as observed in past studies. This approach can be combined with the Monte Carlo Analysis to find the worst case to estimate the fatigue life of the system. Intentionally mistuning the system can reduce the sensitivity of the system to random mistuning, which can be explored further in future studies.

The maximum amplification error for each blade is computed, and the maximum of this dataset is computed to compare the error for different cases using Equation (4.2). The maximum amplification error for the complete sweep is calculated using Equation (4.2). Nodal diameter 11 of the bending mode was chosen to compare these errors, as the FMM model has the best estimate for this case.

$$A_{error,blade} = \max (\max (A_{fullblisk,blade}) - \max (A_{ROM,blade})) \quad (4.1)$$

$$A_{error,sweep} = \max \left(\bigcup_{blade=1}^{33} A_{fullblisk,blade} \right) - \max \left(\bigcup_{blade=1}^{33} A_{ROM,blade} \right) \quad (4.2)$$

The errors computed for maximum amplification for the reduced-order models are illustrated in Figure 4.11 and Figure 4.12. The maximum blade amplification error remains constant for most cases, within 0.15 for the CMM model. In contrast, the error increases as the deviation and average

deviation increase for the FMM model. Although the error is high for the blade amplification, FMM and CMM estimate the maximum amplification value well for the low mistuning cases.

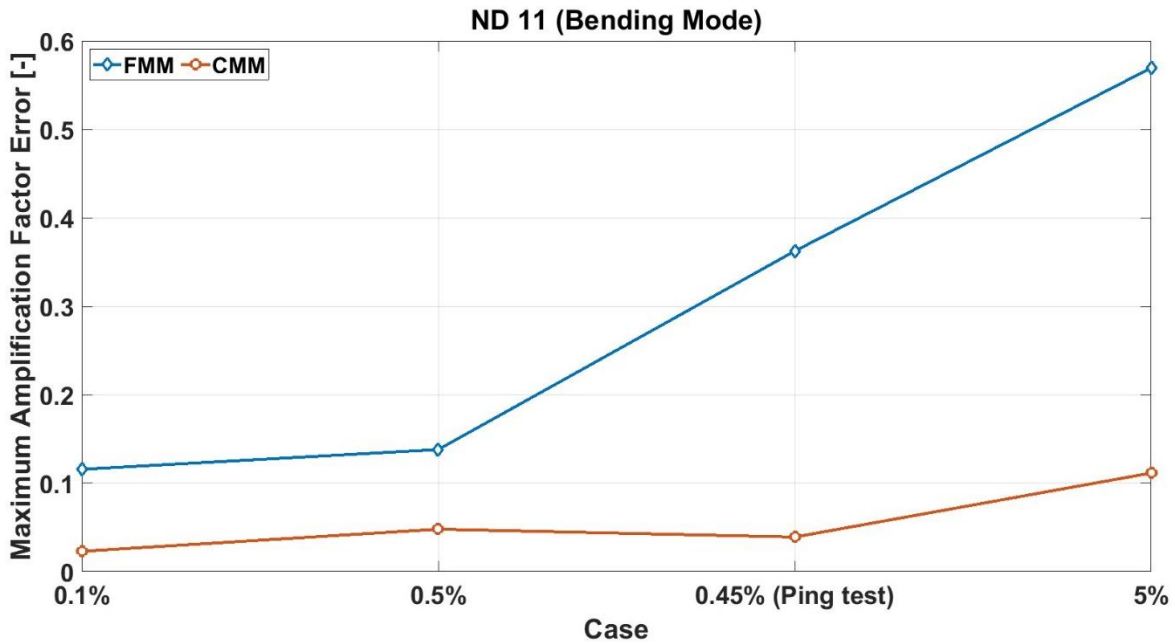


Figure 4.11 Maximum blade amplification factor error for FMM and CMM models at ND 11

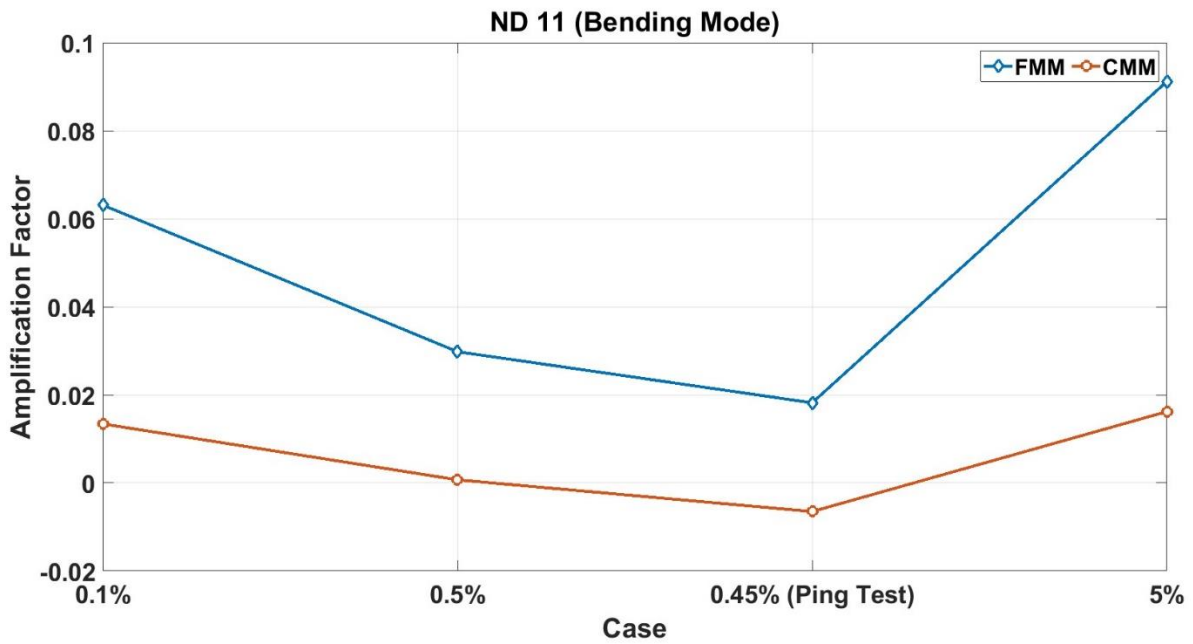


Figure 4.12 Maximum amplification factor error of the sweep for FMM and CMM models at ND 11

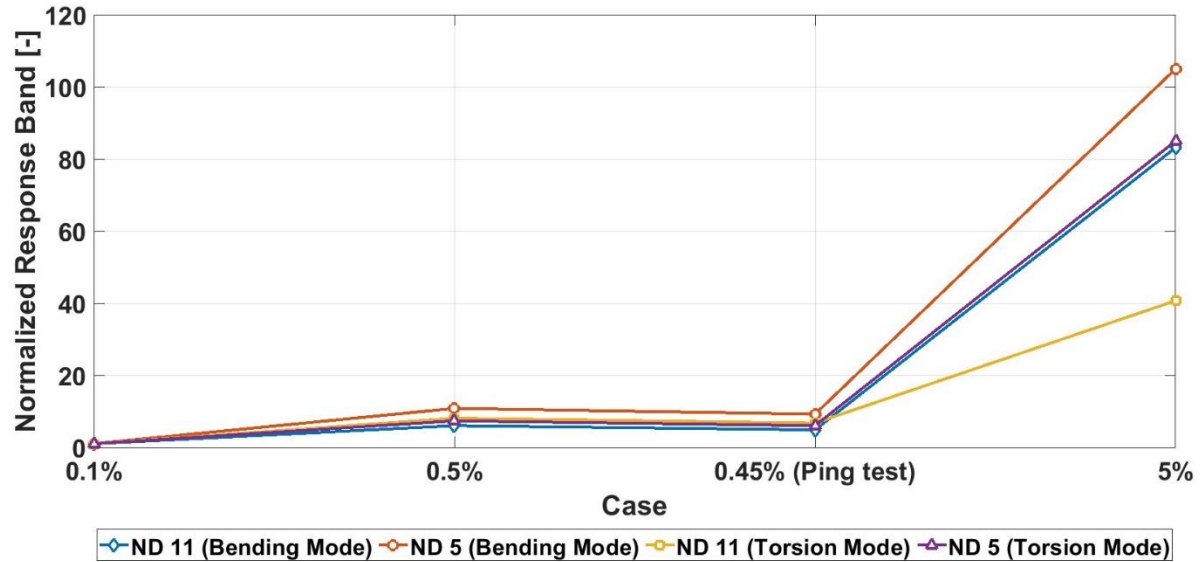


Figure 4.13 Normalized response band

In this investigation, the response band is defined as the frequency band in which the amplification factor is more than 0.2. The frequency band is normalized using the tuned frequency band for each case and shown in Figure 4.13. The frequency band is proportional to the standard deviation of the blade deviations and modal interactions. The frequency band is larger for the ND 5 case for both mode families. The frequency response band is smaller for the ping test case indicating that it is not strongly dependent on the average amplitude of the deviation.

The amplification factors corresponding to a case of random mistuning, including mistuning patterns, which are known to have the worst response from previous research, are shown in Figure 4.14. An amplification factor of 3.12 occurs for the ND 5 case, which is predicted accurately by the CMM model. FMM estimates the response within a 10 percent error for the ND 11 case but fails to give a reasonable estimate for other cases. FMM underpredicts the maximum amplification factor by 50 percent for the ND 5 case. These cases show that CMM is robust for most cases and can accurately predict the response within a reasonable percent error.

$$A_{whitehead} = \frac{1 + \sqrt{N}}{2} = \frac{1 + \sqrt{33}}{2} = 3.3723 \quad (4.3)$$

The maximum amplification factors computed for all cases in this investigation were within the Whitehead limit, the maximum factor by which the amplitude of vibration can increase due to mistuning [36]. The Whitehead limit for this study is computed using Equation (4.3). For all the cases investigated, CMM is a robust reduced-order model that can capture the response's complex features, while the FMM model works well for cases with low modal interactions.

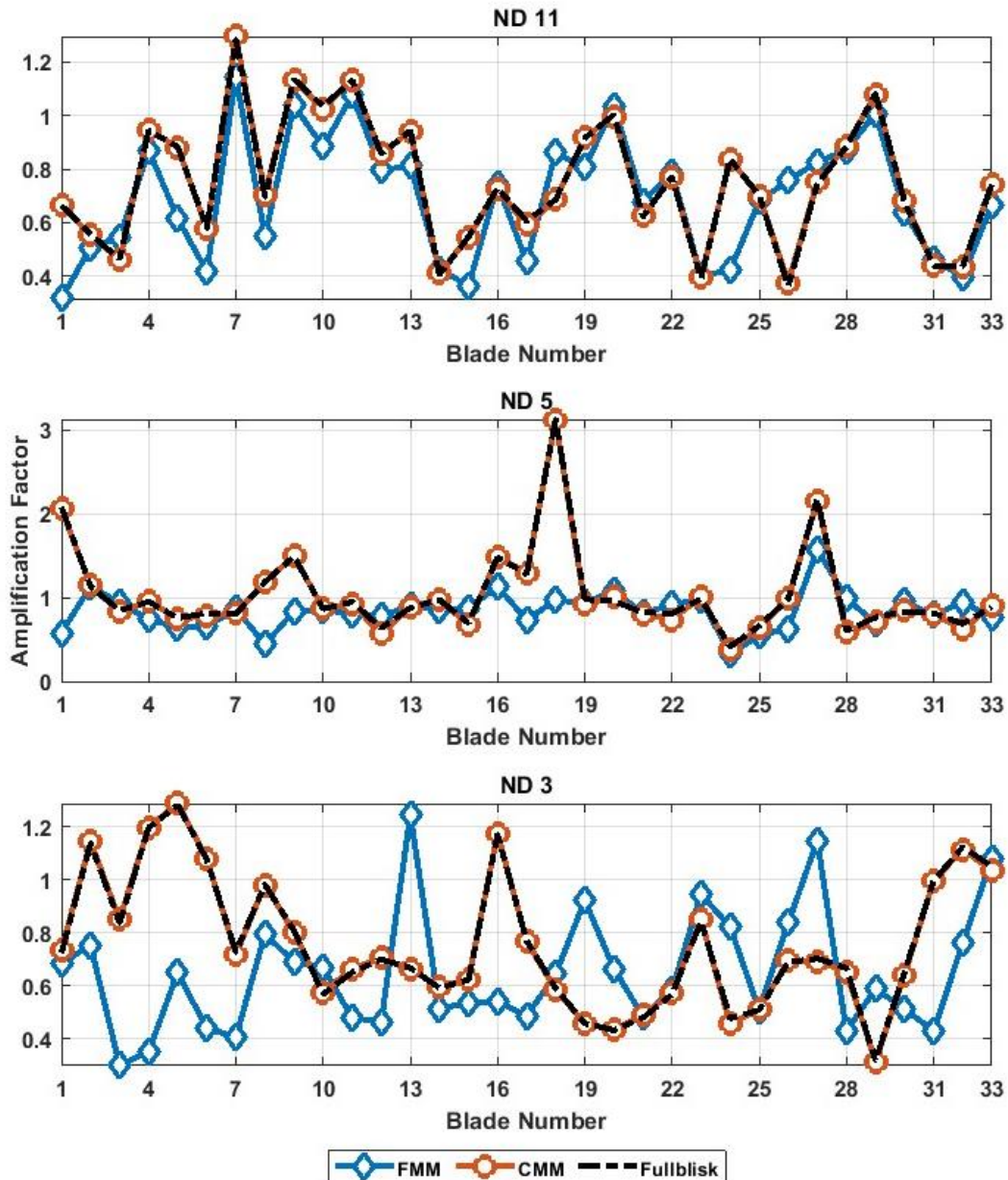


Figure 4.14 Amplification factors for ND 3, ND 5, and ND 11 crossings between 2000 to 3000 Hz (Random Mistuning).

5. SUMMARY AND CONCLUSIONS

This investigation aims to understand the limits of the current reduced-order models and regions of the usability of these models. The current conclusions of the reduced-order models are based on comparing the simulation results with the benchmark full blisk model of Rotor 2 in the Purdue 3-Stage compressor. The model can be modified later to include the aerodynamic coupling, when the unsteady CFD results are available, to validate the model with the experimental data.

5.1 Overview

The forced response is not only a function of standard deviation but also a function of mistuning amplitude and pattern. The amplification factor is maximized when two blade-dominant modes interact due to excessive energy exchange and mode localization. A significant frequency shift is observed in the blade-dominated modes when only the blades are mistuned. While most disk-dominated modes and responses are unaffected by blade mistuning, the effects are slightly notable in cases of very high deviations. The frequency band is a strong function of the standard deviation of the blade deviations and modal interactions and is not strongly dependent on the average amplitude.

The tuned system modes alone are insufficient to predict the forced response without retaining the dominant blade mode for both the reduced-order models. Retaining at least 400 modes is recommended for CMM and the full blisk model to capture the complex responses and mode interactions. CMM converges rapidly with an increasing number of retained tuned system modes. In cases where the modal participation is low from other families, the mode selection can be optimized to further reduce the computational cost of the analysis. Overall isolating the mode family gave better results for cases with low mistuning when a lower number of modes are retained to save the computational cost. CMM estimated the forced response and frequencies within a 2 percent error for all the cases in this study, making it very reliable in the veering regions. CMM can independently mistune each frequency simultaneously, unlike other models, which would be used to validate the model with the ping test results at various crossings.

In the FMM formulation, the tuned modes only need to be calculated once, which has significant computational savings for mistuning studies. FMM is a powerful tool to investigate

responses in the preliminary design stages, as the only input required is the tuned system frequencies and mistuned cantilever blade modes. Incorporating Monte Carlo Simulation to predict the worst-case fatigue life with the FMM model is effortless owing to its simple structure. This model is well suited for high frequency and nodal diameter modes, with strain energy concentrated in the blades. Mode selection is crucial for FMM formulation and affects the response significantly. FMM accurately predicts response for blade-dominated mode families and can capture the complex shape of the response well for cases with low mistuning and negligible modal participation from other families.

FMM best estimates the response for cases where mistuned blade modes are close to the tuned modes. When the two blade dominant modes do not interact significantly, the current FMM formulation gives a better estimate with separate sweeps of both the dominant modes. The results show a considerable lack of accuracy from the FMM reduced order model with the increase in mistuning level compared to the CMM model. Due to its isolated blade mode family assumptions, the FMM method cannot accurately predict the response in these cases. The current FMM formulation can estimate the amplification factor at ND 11 within a reasonable error, especially for the first bending mode. This investigation provides the necessary statistics to understand the reduced-order models and allows a more informed decision to use these models for different cases in the future.

5.2 Recommendations for future work

The reduced-order models should be validated with the experimental results to understand the accuracy of these models with aerodynamic coupling. The NSMS and strain gauge data acquired for GUIde 6 must be used to validate these models. Previous research has shown that the forced response is a strong function of interblade coupling, which could be investigated for different loading conditions and EO excitations after validation. The response at each EO must be estimated with the respective rotational speed at each crossing to include accurate stiffening effects at that speed.

Past research showed the reliability of FMM in cases where modes are not strongly excited, even in the regions with disk participation, which can be explored further. The cases investigated in this study did not have crossing regions which are potentially complex regions for the reduced

order models. It would be worth studying regions with higher complexity, including multistage effects.

The reduced order models are extremely sensitive to the retained modes and selection of modes. Optimization of the selection of tuned system modes can be explored for both the reduced order models to reduce the computational cost further. In cases where the tuned system modes and blade modes are far apart, FMM can be further explored, including the frequency shift method.

It would be interesting to study the forced response and reduced order modeling for high-speed machines where Coriolis and spin softening effects are significant and change the frequencies by more than 5 percent. Investigating the cases with non-proportional mistuning, as occurs with wear or damage, would be valuable. Studying these models for shrouded blades, exhibiting better vibration suppression ability, would also be noteworthy. The forced response is generally computed with harmonic analysis, which ignores the nonlinear effects. The transient effects can be further studied with a transient analysis.

APPENDIX: HARMONIC ANALYSIS METHODS

Full harmonic method

This method does not involve any matrix reduction or mass approximations and uses the full system of matrices. Therefore, these matrices are not constrained to symmetric and can be unsymmetric. This method utilizes full matrices to compute all the displacements and stresses in a single pass, making it computationally expensive, especially with the sparse solver. When the system is bulky and well-conditioned, this method is efficient. The full harmonic analysis supports frequency-dependent elastic and damping properties but ignores any nonlinear elements defined in the model.

Frequency sweep method

This method uses full system matrices, but the Variational Technology method interpolates the system matrices and loads to the frequency range requested by computing it at the range's midpoint. This method provides a higher performance solution as it approximates the results across the range instead of using the full matrices to calculate results at the last range point. This method allows all types of loads like forces, pressure, temperature, and displacements and computes the displacements and stresses in a single pass. This method only supports sparse solvers in Ansys Mechanical, which can be computationally expensive for large problems and is less efficient for a small frequency range. This method allows us to change the material properties, geometry, and constants without changing the mesh connectivity before resolving a frequency sweep harmonic analysis.

Mode-superposition harmonic analysis

The number of modes included in the calculation can be chosen per the frequency sweep range. This method can incorporate modal damping and pre-stress effects from static analysis. The element loads are included in the harmonic analysis using the LVSCALE command, which is applied in the preceding modal analysis. As the mode shapes are used to compute the response, the solutions tend to be concentrated around the system's natural frequency, giving us a smoother and more accurate response curve. This method supports mode-dependent damping. The initial modal analysis calculates a modal force vector to compute the dynamic response.

$$[M]\{\ddot{u}\} + [C]\{\dot{u}\} + [K]\{u\} = \{F\} \quad (5.1)$$

$$\{F\} = F_{time\ varying\ nodal\ load} + F_{modal\ load} \quad (5.2)$$

The equations are normalized with respect to mass which changes the equation of motion to modal coordinates using Equation (5.5). The modal coordinates corresponding to i^{th} mode shape (ϕ_i) is represented using y_i .

$$\{\phi_i\}^T [M] \{\phi_i\} = 1 \quad (5.3)$$

$$[M] \{\phi_i\}^2 = 1 \quad (5.4)$$

$$\{\phi_i\} = \frac{1}{\sqrt{M_i}} \quad (5.5)$$

This substitution simplifies the damping and stiffness matrix as equations (5.6) and (5.7).

$$\{\phi_i\}^T [C] \{\phi_i\} = 2\xi_i \omega_i \quad (5.6)$$

$$\{\phi_i\}^T [K] \{\phi_i\} = \omega_i^2 \quad (5.7)$$

$$\ddot{y}_i + 2\xi_i \omega_i \dot{y}_i + \omega_i^2 y_i = f_i \quad (5.8)$$

The forced response with an excitation frequency of ω_e amplitude is computed using Equation (5.9).

$$y_i = \frac{f_i}{(\omega_i^2 - \omega_e^2) + i(2\xi_i \omega_i \omega_e)} \quad (5.9)$$

The displacement vectors are then calculated using each mode's modal contribution, computed using mode shape using Equation (4.2).

$$\{CM_i\} = \{\phi_i\} y_i \quad (5.10)$$

$$\{u\} = \sum_{i=1}^n \{CM_i\} = \sum_{i=1}^n \{\phi_i\} y_i \quad (5.11)$$

REFERENCES

- [1] P. Beuseroy and R. Lengellé, "Nonintrusive turbomachine blade vibration measurement system," *Mechanical Systems and Signal Processing*, vol. 21(4), pp. 1717-1738, 2007.
- [2] A. R. Collar, "The expanding domain of aeroelasticity," *The Aeronautical Journal*, vol. 50, no. 428, pp. 613-636, 1946.
- [3] C. Hoen, "An Engineering Interpretation of the Complex Eigensolution of Linear Dynamic Systems," in *IMAC XXIII*, 2005.
- [4] Z. Hui-Ying and M. Xiu-Hua, "Study on Vibration Characteristics of High-Speed Rotating Constrained Blades Based on Spin Softening," *Applied Mechanics and Materials*, vol. 863, pp. 241-245, 2017.
- [5] S. Houxin and L. Chaofeng, "Effects of centrifugal stiffening and spin softening on nonlinear modal characteristics of cyclic blades with impact–friction coupling," *Springer Publications*, 2022.
- [6] K. Xuanen, X. Zili, Z. Bo and Z. Jize, "Effect of Coriolis force on forced response magnification of intentionally mistuned bladed disk," *Journal of Sound and Vibration*, vol. 399, 2017.
- [7] M. Baumgartner, F. Kameier and J. Hourmouziadis, "Non-Engine Order Blade Vibration in a High-Pressure Compressor," in *Twelfth International Symposium on Airbreathing Engines*, Melbourne.
- [8] Y. Leng, "Preliminary Design Tools in Turbomachinery: Non-uniformly Spaced Blade Rows, Multistage Interaction, Unsteady Radial Waves, and Propeller Horizontal-Axis Turbine Optimization (Ph.D. Dissertation)," Purdue University, West Lafayette, Indiana, 2016.
- [9] F. Nyssen, "Numerical Modeling and Experimental Identification of Mistuned Multi-Stage Bladed Assemblies (Ph.D. Dissertation)," University of Liege, Belgium.
- [10] C. C. Paige, "Accuracy and effectiveness of the Lanczos algorithm for the symmetric eigenproblem," *Linear algebra and its applications*, vol. 34, pp. 235-282.

- [11] Y. J. Kim, "Block Lanczos Algorithm," Naval Postgraduate School, Monterey, 1989.
- [12] R. Razvan, "Experimental Investigation of Inlet Distortion in a Multistage Axial Compressor," Purdue University, West Lafayette, Indiana, 2017.
- [13] L. Jing, "Multi-Row Aerodynamic Interactions and Mistuned Forced Response of an Embedded Compressor Rotor (Ph.D. Dissertation)," Duke University, Durham, North Carolina.
- [14] D. J. Ewins, "Vibration Characteristics of Bladed Disc Assemblies," *Journal of Mechanical Engineering Science*, vol. 15, pp. 165-186, 1973.
- [15] W. J. Chen and C. Pierre, "Vibration Localization and Wave Conversion Phenomenon in a Multi-Coupled, Nearly Periodic Disordered Truss Beam," in *AIAA Dynamics Specialists Conference*, Dallas, Texas, 1992.
- [16] C. Pierre, "Localization of Aeroelastic Modes in Mistimed High-Energy Turbines," *JOURNAL OF PROPULSION AND POWER*, vol. 10, no. 3, 1994.
- [17] Y. Kaneko, "Study on Transient Vibration of Mistuned Bladed Disk Passing Through Resonance," in *ASME Turbo Expo*, San Antonio, Texas, 2013.
- [18] K. V. K. R. E. Kaza, "Flutter and Response of a Mistuned Cascade in Incompressible Flow," *AIAA Journal*, vol. 20, no. 8, pp. 1120-1127, 1981.
- [19] C. Pierre, J. Judge, S. Ceccio and e. al, "Experimental Investigation of the Effects of Random and Intentional Mistuning on the Vibration of bladed Disks (Ph.D. Dissertation)," University of Michigan, Ann Arbor, Michigan, 2002.
- [20] M. P. Mignolet, H. Wei and J. Ioan, "On the Forced Response of Harmonically and Partially Mistuned Bladed Disks. Part I: Harmonic Mistuning," *International Journal of Rotating Machinery*, vol. 6, 1998.
- [21] L. Yang, M. Ma, S. Wu, X. Chen, R. Yan and Z. Mao, "An improved analytical dynamic model for rotating blade crack: With application to crack detection indicator analysis," *Journal of Low Frequency Noise, Vibration and Active Control*, vol. 40, no. 4, 2021.
- [22] M. U. Bashir, A. U. Rehman, A. Waleed, U. S. Virk and M. R. Javed, "Modeling and analysis of a mistuned fan blisk," *Journal of Engineering Research*, vol. 10, no. 3, pp. 246-257, 2021.
- [23] "Ansys Structural Analysis Guide," Ansys Inc., 2019.

- [24] J. Yuan, F. Scarpa, G. Allegri, B. Titurus, S. Patsias and R. Rajasekaran, "Efficient computational techniques for mistuning analysis of bladed discs: A review," *Mechanical Systems and Signal Processing*, 2016.
- [25] G. M. L. Gladwell, "Branch Mode Analysis of Vibrating Systems," *Journal of Sound and Vibration*, vol. 1, no. 1, pp. 41-59, 1964.
- [26] D. Krattiger, L. Wu, M. Zacharczuk, M. B. c, R. J. K. d, M. S. Allen, P. Tiso and M. R. Brake, "Interface reduction for Hurty/Craig-Bampton substructured models: Review and improvements," *Mechanical Systems and Signal Processing*, vol. 114, pp. 579-603, 2019.
- [27] M. G. Salas, "Development of Accurate Reduced Order Models in a Simulation Tool for Turbomachinery Aeromechanical Phenomena (Ph.D. Dissertation)," KTH Royal Institute of Technology, Stockholm, Sweden, 2018.
- [28] S. Lim, R. Bladh, M. P. Castanier and C. Pierre, "A Compact, Generalized Component Mode Mistuning Representation for Modeling Bladed Disk Vibrations," in *44th AIAA/ASME/ASCE/AMS Structures, Structural Dynamics, and Material Conference*, Virginia, USA, 2003.
- [29] M. P. C. a. C. P. R. Bladh, "Reduced Order Modeling and Vibration Analysis of Mistuned Bladed Disk Assemblies With Shrouds," *Journal of Engineering for Gas Turbines and Power*, vol. 121, no. 3, p. 515–522, 1999.
- [30] D. M. Feiner and J. H. Griffin, "A Fundamental Model of Mistuning for a Single Family of Modes," *Journal of Turbomachinery*, vol. 124, 2002.
- [31] Y. Leng, "In-house FMM Formulation based on Feiner et al. [30]".
- [32] D. R. Matthews, "Unsteady Aerodynamics And Blade-Row Interactions In The Embedded Stage Of An Axial Compressor (MS Thesis)," Purdue University, 2017.
- [33] P. A. N. Aye-Addo, "An Experimental Study Of The Effects Of Vane Count And Non-Uniform Vane Spacing On Rotor Resonant Response (MS Thesis)," Purdue University, 2016.
- [34] I. B. Celik, U. Ghea, P. J. Roache, C. J. Freitas, H. Coleman and P. E. Raad, "Procedure for Estimation and Reporting of Uncertainty Due to Discretization in CFD applications," *Journal of Fluids Engineering*, vol. 130.

- [35] R. J. Allemang, "The Modal Assurance Criterion –Twenty Years of Use and Abuse," *Sound and Vibration*, vol. 37, pp. 14-23, 2003.
- [36] M. Pastora, M. Binda and T. Harparik, "Modal Assurance Criterion," *Procedia Engineering*, vol. 48, pp. 543-548, 2012.
- [37] D. S. Whitehead, "The Maximum Factor by Which Forced Vibration of Blades Can Increase Due to Mistuning," *Journal of Engineering for Gas Turbines and Power*, vol. 120, pp. 115-119, 1998.